INFORMATION TO USERS

This manuscript has been reproduced from the microfilm master. UMI films the text directly from the original or copy submitted. Thus, some thesis and dissertation copies are in typewriter face, while others may be from any type of computer printer.

The quality of this reproduction is dependent upon the quality of the copy submitted. Broken or indistinct print, colored or poor quality illustrations and photographs, print bleedthrough, substandard margins, and improper alignment can adversely affect reproduction.

In the unlikely event that the author did not send UMI a complete manuscript and there are missing pages, these will be noted. Also, if unauthorized copyright material had to be removed, a note will indicate the deletion.

Oversize materials (e.g., maps, drawings, charts) are reproduced by sectioning the original, beginning at the upper left-hand corner and continuing from left to right in equal sections with small overlaps.

Photographs included in the original manuscript have been reproduced xerographically in this copy. Higher quality 6" x 9" black and white photographic prints are available for any photographs or illustrations appearing in this copy for an additional charge. Contact UMI directly to order.

Bell & Howell Information and Learning
300 North Zeeb Road, Ann Arbor, MI 48106-1346 USA
800-521-0600

UMI®

Reproduced with permission of the copyright owner. Further reproduction prohibited without permission.

Reproduced with permission of the copyright owner. Further reproduction prohibited without permission.

ELASTIC ANALYSIS OF INTERFACES IN SOLIDS

by

Leonid Evguenievich Shilkrot

A dissertation submitted in partial fulfillment
of the requirements for the degree of
Doctor of Philosophy
(Materials Science and Engineering)
in The University of Michigan
1999

Doctoral Committee:

Professor David J. Srolovitz (Chairman)
Professor James R. Barber
Assistant Professor Rachel S. Goldman
Assistant Professor Joanna Mirecki-Millunchick
Associate Professor Steven M. Yalisove

Reproduced with permission of the copyright owner. Further reproduction prohibited without permission.

UMI Number: 9959859

UMI®

UMI Microform9959859
Copyright 2000 by Bell & Howell Information and Learning Company.
All rights reserved. This microform edition is protected against
unauthorized copying under Title 17, United States Code.

Bell & Howell Information and Learning Company
300 North Zeeb Road
P.O. Box 1346
Ann Arbor, MI 48106-1346

Reproduced with permission of the copyright owner. Further reproduction prohibited without permission.

To my parents

Reproduced with permission of the copyright owner. Further reproduction prohibited without permission.

ACKNOWLEDGMENTS

I would like to express my deepest gratitude to my advisor, Prof. David J. Srolovitz for giving me the opportunity to work with him over these five years in Michigan. His brilliant scientific mind, boundless patience, help and encouragement made, in large part, this thesis possible.

I am grateful to Prof. James R. Barber whose course and consequent discussions of my research problems opened to me the field of elasticity. I would also like to thank Profs. Rachel S. Goldman and Joanna Mirecki-Millunchick through interactions with whom I learned to appreciate the work of experimentalists. They all kindly agreed to serve as members of my doctoral committee.

Last, but not at all the least, I want to thank all my friends: A. Rosenflanz, D. Shashkov, D. Gorelikov, M. Chumak, N. Zacharopoulos, B. Harnke, M. Johnson, members of the Lab, past and present, and many others for being around during my years in the graduate school.

Finally, the funding provided by the US Department of Energy is gratefully acknowledged.

Reproduced with permission of the copyright owner. Further reproduction prohibited without permission.

TABLE OF CONTENTS

DEDICATION ii

ACKNOWLEDGMENTS iii

TABLE OF CONTENTS iv

LIST OF FIGURES vi

LIST OF TABLES ix

LIST OF APPENDICES x

CHAPTER

I INTRODUCTION 1

1.1 Background 2
1.2 Effects of interfaces 6
1.3 Interfacial kinetics 10
1.4 Dissertation overview 15
References to Chapter I 18

II ELASTIC ANALYSIS OF FINITE STIFFNESS BIMATERIAL INTERFACES: Application to dislocation -interface interactions 20

2.1 Introduction 20
2.2 Elastic analysis 22
2.3 Applications 27
2.4 Conclusions 38
References to Chapter II 40

III MORPHOLOGY EVOLUTION DURING MULTILAYER FILM GROWTH 50

3.1 Introduction 50
3.2 Problem formulation 52
3.3 Elastic analysis 56
3.4 Solution of the evolution equation 60
3.5 Stability diagrams 65

Reproduced with permission of the copyright owner. Further reproduction prohibited without permission.

3.6 General case 69
3.7 Conclusions 75
References to Chapter III 78

IV ELASTIC MODELS OF SURFACE DEFECTS 93

4.1 Introduction 93
4.2 Elastic model of a surface step 95
4.3 Elastic model of adatom interactions on a solid surface 112
4.4 Adatom-step interactions 124
4.5 Conclusions 133
References to Chapter IV 136

V CONCLUSIONS AND SUGGESTIONS FOR FUTURE RESEARCH 152

References to Chapter V 156

APPENDICES 157

Reproduced with permission of the copyright owner. Further reproduction prohibited without permission.

LIST OF FIGURES

Figure

2.1. An illustration of the configuration employed in the analysis of the interaction between the source of stress (indicated by a dislocation) and a bimaterial interface. 41

2.2. The normalized climb force $\mathbf{f}_y^*$ on a single dislocation versus the normalized dislocation/interface separation c/b..... 42

2.3. The dependence of the normalized equilibrium separation $c^*\kappa_1/\mu_1$ on the Dundurs parameter Γ.. 43

2.4. Normalized climb force $\mathbf{f}_y^* c/b$ versus normalized separation $c\kappa_1/\mu_1$ for different values of the Dundurs parameter Γ..... 44

2.5. An illustration of the configuration employed in the analysis of the interaction between an array of misfit dislocations and a bimaterial interface..... 45

2.6. The normalized climb force F^* acting on dislocations in the array vs. the normalized dislocation/interface separation $\Lambda = 2\pi c/d$ for the case of a "welded" interface. 46

2.7 The normalized climb force F^* acting on dislocations in the array versus the normalized dislocation/interface separation Λ in the "slipping" interface limit.. 47

2.8 The normalized climb force F^* acting on dislocations in the array versus the normalized dislocation/interface separation Λ for a finite interfacial stiffness.. 48

2.9 The dependence of the equilibrium stand-off distance Λ_0 on the Dundurs parameter Γ for different values of the interface stiffness.. 49

3.1 A thin film with an undulating surface subjected to a stress σ..... 80

Reproduced with permission of the copyright owner. Further reproduction prohibited without permission.

3.2 A schematic illustration of the multilayer film geometry, indicating the amplitude of the interface undulations Δ and the layer thicknesses *H*... 81

3.3 Multilayer film morphology produced by a) an in-phase instability and b) an out-of-phase instability..... 83

3.4 Stability diagram for a growing multilayer film, indicating the types of morphologies expected classified according to the eigenvalue λ_{max} 84

3.5 Contour plot of the logarithm of the absolute value of λ_{max}... 85

3.6 Contour plot of ξ^*_{max} for the domains of unstable multilayer growth... 86

3.7 Stability diagram for a growing multilayer film with a constraint on the wave vector ξ^*_{max} to values where an initial perturbation on the first layer would grow.. 87

3.8 Stability diagrams for situations where the materials A and B differ from each other by more than simply the sign of the misfit stress... 91

3.9 Stability diagram for the strain-balance superlattice (i.e., superlattices for which $H_A\Sigma_A + H_B\Sigma_B = 0$) 92

3A.1 The geometry used to compute the stress on the surface caused by an interface buried at depth *h*. The interface is modeled by a line load which can vary along *x*, **f**(*x*)..... 166

4.1 Surface tractions produced by discontinuities of the surface stress on a faceted surface 139

4.2 The geometry of the simulation cell.. 140

4.3 Interaction energy of the steps on vicinal ($\bar{1}\bar{m}0$) surfaces vs. the square of the inverse step separation for gold and nickel 142

4.4 Displacement field for a periodic array of <100> steps on a {001} surface obtained from the atomistic simulations... 144

4.5 Displacement field for a periodic array of <100> steps on a {001} surface obtained from the anisotropic elastic theory (Eq. 10) using the best fit surface line force dipole vector **D**.. 145

4.6 Geometry of the simulation cell used to determine the adatom - adatom interaction strength.. 146

Reproduced with permission of the copyright owner. Further reproduction prohibited without permission.

4.7 Polar plot of $\mathbf{h}_{zz}(\alpha)$ for the {001} plane of EAM Ni..... 147

4.8 Polar plot of the adatom interaction energy, as per Eq. (35)..... 148

4.9 The adatom-adatom interaction energy for adatoms on the (001) surface of EAM Ni vs. the inverse nearest neighbor adatom separation S_1^{-1} for different adatom lattice period ratios: S_2:S_1..... 149

4.10 Geometry of the simulation cells used to determine step - adatom interaction strength..... 150

4.11 The step-adatom interaction energy for the case of a (001) surface with [100] steps in EAM Ni..... 151

Reproduced with permission of the copyright owner. Further reproduction prohibited without permission.

LIST OF TABLES

Table

4.1 The coefficients of $(d_0)^{-m}$ in the expansion of the step-step interaction energy E_{int} vs. the inverse interstep spacing d_0, as per Eq. (7)..... 102

4.2 The two independent components of the surface line force dipole $\mathbf{D}_x$ and $\mathbf{D}_y$ (eV/Å) and the coefficient A_2 (eV Å) of the $(d_0)^{-2}$ in the expansion of the step-step interaction energy E_{int} vs. the inverse interstep spacing d_0, as per Eq. (7) of Chapter IV with $A_1 = A_3 = 0$..... 110

4.3 The surface stress τ and surface energy γ of the {001} surface of Au and Ni determined from the present atomistic simulations..... 111

4.4 The magnitude of the lattice summation Σ (Eq. (34)) for different adatom lattice period ratios S_2:S_1..... 121

4.5 The parameters describing adatom-adatom interactions on a (100) surface of EAM Ni, obtained by fitting the data in Fig. 4.9 to the functional form in Eq. (37)..... 123

4.6 The magnitude of the point force dipole strength A as per Eq. (38)..... 124

4.7 The parameters describing the interactions between a [100] step on a (100) surface and an adatom..... 132

Reproduced with permission of the copyright owner. Further reproduction prohibited without permission.

LIST OF APPENDICES

Appendix

2A Surface Green's function 158

2B Exponential integral identities.... 160

2C Evaluation of the Fourier series. 161

3A Surface stress from a buried line load. 164

3B Solution of the recurrence relations 167

4A Anisotropic surface elastic Green tensor 172

Reproduced with permission of the copyright owner. Further reproduction prohibited without permission.

CHAPTER I

INTRODUCTION

Interfaces are an important feature of material microstructures and, as such, are of great interest from both applied and scientific points of view. The presence of interfaces and grain boundaries affects most technologically useful properties of materials. The modern electronic industry owes its existence to the p-n junction, which is an interface between two differently doped regions of a semiconductor. Thin film technologies rely heavily on processes that occur on the free surface and at interfaces to control the structure and quality of the growing film. Interfaces also play a key role in composite materials, where they provide the link between reinforcements and the matrix that control mechanical response. The central goal of the study of interfaces is to provide a picture of how interfaces affect the properties of materials. Following the traditional materials science approach, this is done through establishment of structure - property relationships. Establishment of a full understanding of the role of interfaces in materials is well beyond the scope of this thesis. Instead, we focus on the much more modest theme of the elasticity of interfaces. This also is too broad an area, so we will instead examine several specific cases of the effects and descriptions of elastic issues involving in interfaces in solids. In particular, we investigate: 1) the effects of elastic boundary conditions at an interface and apply the results to the interactions between misfit dislocations and interfaces; 2) the study of the morphological stability of a misfitting multilayer thin film during epitaxial growth which combines both macroscopic thermodynamics and kinetics at the interface; 3) the study of elastic interactions of defects on solid surfaces which deals with the microscopic structure of a free surface (crystal – vacuum interface). These

Reproduced with permission of the copyright owner. Further reproduction prohibited without permission.

three applications span continuum and atomistic descriptions of interfaces, as well as relevant interfacial thermodynamic and kinetics issues.

1.1 Background

An interface is a boundary that separates two bodies that exhibit some differences in materials properties (the dimensionality of an interface is always one less than that of the two bodies).The difference between the two bodies can be in their chemical nature of the materials (e.g., Fe and FeO) or in their structure (at fixed chemistry), such as two grains with different crystallographic orientation (i.e., meeting at a grain boundary). Depending on the properties of interest, the interface can be viewed in a continuum context as the boundary where some material property changes discontinuously or in an atomic context as a finite width region with well defined properties of its own. On a macroscopic level we can discuss thermodynamic and kinetic features, while on a microscopic level we can analyze the structure of the interface. In many cases, but certainly not all, macroscopic properties are determined by the atomic structure of the interface.

In a continuum description, an interface is a place where a physical parameter or its spatial derivative is discontinuous. A simple example is a case where the elastic constants change abruptly as the interface is traversed. A more interesting mechanical example is a case where the elastic fields change abruptly when the interface is crossed. This abrupt change can result from differences in elastic constants (as in the previous example) or from misfit. In either case, the governing differential equations are modified as the interface is traversed. These changes can be parametric, such as results from a change in elastic constants or from the introduction of new terms, such as from misfit. Additionally, the elastic fields can be modified by the boundary conditions that must be applied at the interface. For example, in some cases, certain components of the stress may

Reproduced with permission of the copyright owner. Further reproduction prohibited without permission.

be zero or continuous at the interface. The issue of boundary conditions associated with different types of interfaces will be discussed in detail in Chapter II.

Microscopic descriptions of interfaces depend on the level of detail which is of interest and/or accessible. For example, at one level an interface appears flat, while closer examination shows that it is in fact rough. A more detailed look shows that the interface is composed of a regular array of structural elements. On an even finer scale, we may find that the chemical composition within a few Ångstroms of the interface is quite different than that of the bounding materials.

The taxonomy of interfaces involves three criteria. By the degree of matching between atomic planes, interfaces can be classified as coherent (full matching such as GP zones), semi-coherent (partially relaxed by misfit dislocations) and incoherent (such as the interface between an inert gas film on a metallic surface [1]). Interfacial energy is commonly the smallest for coherent interfaces, increases when the interface is partially relaxed, and largest for incoherent interfaces [2]. On the other hand, the energy of the entire system containing an interface may be lowest when the interface is incoherent – consider the case of two macroscopic bodies with different crystal structures and vastly different lattice parameters meeting along an interface.

Interfaces which join identical materials with differently oriented crystal lattices (grain boundaries) are called homophase interfaces. The interfaces between two materials with dissimilar Bravais lattices or chemical composition is referred to as a heterophase interface. A heterophase interface is not always a sharp dividing surface between two materials, but may be extending into the bulk of the two materials (i.e., without sharp dividing surfaces). This can occur in a system with a miscibility gap in the phase diagram, where the two phases interpenetrate each other at the onset of the phase transformation below the transition temperature [3]. The interface may also be wide in the case where the two bounding materials are of the same phase. For example, grain

Reproduced with permission of the copyright owner. Further reproduction prohibited without permission.

boundaries in ceramics often exhibit a microscopic glassy layer, which may be thought of as extended interfaces [4].

The properties of an interface are determined by the local chemical environment of atoms at or near the interface. Since the arrangement of atoms in the interfacial region are different from that in the bulk of the material, the electron density and atomic bonding at the interface are different than those of the bulk. Furthermore, since most properties have their origin within the electronic structure, this change in bonding at the interface will modify many physical properties, including strength, energy, etc. For the purposes of a macroscopic description, the consequences of the variation in atomic bonding at the interface can be accounted for by way of phenomenological models, as will be seen in Chapters II and IV. The description of bonding at interfaces is beyond the scope of this thesis.

It is easier to discuss the crystallography of interfaces for the case where the two bounding materials have the same structure (i.e., the homophase, rather than the heterophase case). One approach to understanding interfacial structure is to consider how the two lattices fit together without any relaxation (i.e., a hard sphere or rigid lattice assumption). It is widely believed that if the structures fit together well (i.e., share many common sites), the interface will be of low energy and exhibit "special" properties. This approach is formalized in the coincidence site lattice (CSL) description, in which a new lattice is created from the sites where the two interpenetrating lattices share common positions [5]. These sites represent areas of good atomic matching while the intervening sites exhibit poor matching. The degree of matching may be summarized in terms of the inverse density of coincident sites (known as the Σ value) [6].

The domain of poor matching between coincident sites is described by introducing structural defects (interfacial dislocations). The earliest example of such an approach is the description of low angle symmetric tilt boundaries in terms of a regular array of edge dislocations with Burgers vectors perpendicular to the boundary plane [7].

Reproduced with permission of the copyright owner. Further reproduction prohibited without permission.

Dislocation arrays are useful for describing both low angle tilt (symmetric or asymmetric) and twist boundaries. This simple model of dislocation arrays becomes inapplicable for high-angle grain boundaries where the spacing between dislocations becomes of order or smaller than the lattice parameter and heterophase structures with different crystal lattices where the CSL does not exist. However, the method of introducing interfacial dislocations to describe interpenetrating lattices was generalized by Bilby [8] and Frank [9]. The O-lattice approach describes a more general matching between the lattices [10]. Although lattice matching may not be possible in many cases, positions (occupied by atoms or not) may exist in the two crystal lattices that match. The resultant array of sites are create the O-lattice. In this framework, the O-lattice can be used to identify interfacial dislocations. Bilby and Frank derived an equation to determine the Burgers vector of interfacial dislocations which describes the interfacial dislocation density [8, 9] and is related to the more general concept of dislocation density tensors in bulk materials.

Although a grain boundary may be described by one or more sets of interfacial dislocations, it is important to stress that these interfacial defects do not introduce long-range elastic fields in the bounding grains. As shown in Ref. [11], while the stress and strain fields of a single dislocation are long range and decay very slowly (the displacement field diverges logarithmically with distance), the elastic field of a dislocation wall in a symmetric tilt grain boundary decays exponentially. Any set of interfacial dislocations obeying the Frank formula [9] also satisfies this condition.

A related and technologically important example of dislocations at an interface arises in heteroepitaxially grown thin films, where an array of misfit dislocations is formed when the film is sufficiently thick [12]. A traditional description of a misfit dislocation is a geometrical one, stemming from the matching of lattices between the film and the substrate the film is grown on. Another way of looking at the origin of misfit dislocations is the following. A calculation of the stress field produced by an array of parallel edge dislocations buried in an elastic half-space with the Burgers vectors parallel

Reproduced with permission of the copyright owner. Further reproduction prohibited without permission.

to the free surface (i.e., a film on the substrate with the misfit dislocation array at the interface) has two components. One is exponentially decaying with distance from the dislocation array and is unimportant for this discussion. The other is a uniform tensile (or compressive) stress in the direction along the Burgers vector which is only present between the dislocations and the free surface (i.e., the uniform stress in the film only and not in the half-space). It is possible to show that the geometrical description of misfit dislocation (i.e., the spacing between the dislocations in the array and the magnitude of the Burgers vector) assures that the stress produced by the dislocation array completely cancels the misfit stresses in the film. A misfit dislocation array is a natural way to create a long range stress in the film to cancel the misfit stress. The exponentially decaying part of the stress field along with the dislocation cores prevents misfit dislocations from appearing when the film thickness is small (i.e., the energy associated with the local stress field and the dislocation cores is too large to be compensated by relieving the long range misfit stress in very thin films). This explains the phenomenon of critical thickness for misfit dislocation formation [13].

1.2 Effects of interfaces

As mentioned above, interfaces can modify the boundary condition on continuum fields. Such boundary conditions can lead to discontinuities, either in the field or in its first derivatives (with respect to the coordinates tangential and normal to the interface). The most trivial example of the effects of such boundary conditions can be seen in the refraction of light - the boundary conditions for Maxwell's equations for the vectors **E** and **B**, which govern the penetration of electromagnetic fields across the interface. In this thesis, it is more pertinent to focus on the elastic boundary conditions that must be satisfied at interfaces. For a material under an external load or containing internal sources of stress, an interface presents a discontinuity in the field of elastic stresses and

Reproduced with permission of the copyright owner. Further reproduction prohibited without permission.

displacements. In the most general case, there are six equations which must be satisfied at the interface in three dimensions. (One for each component of the displacement vector and one for each component of the traction vector). The three equations on the tractions are a trivial consequence of the requirement that the material at the interface is static: the total force at the interface (which is a sum of the tractions on both sides of the interface) must be zero. The three other equations cannot be deduced from first principles, but are determined based on the nature of the interfacial structure. The conventional boundary conditions, used in most elastic calculations, are called "welded interface" conditions, in which the displacement vector is assumed to be continuous across the interface. The issue of the appropriate boundary conditions is addressed in detail in Chapter II.

The elastic boundary conditions associated with interfaces can be handled quite simply in some cases. An interface separating two region with dissimilar elastic constants alters the elastic field of dislocations. In the simplest case of a screw in an elastic half-space, where the interface is a free surface of the material, the dislocation-interface interaction can be analyzed by introducing a dislocation image of the opposite sign by analogy with images of electrostatic charges created by a metal surface. This construction leads to a force attracting the dislocation to the free surface and decaying proportionally to the inverse distance between the dislocation and an interface. On the other hand, an image construction does not satisfy the elastic boundary conditions for the case of an edge dislocation near a surface. Nonetheless, it is still relatively straightforward to show that the elastic boundary conditions leads to an attractive force between an edge dislocation and a free surface. Rather complete analyses of this and related situations involving bimaterial interfaces may be found in the works of Head [14] and Dundurs [15]. We return to this topic of the effect of elastic boundary conditions on dislocations interacting with bimaterial interfaces in Chapter II.

Koehler [16] proposed using the effect of images to design an exceptionally strong solid. He suggested using a periodic epitaxial structure of extremely thin

Reproduced with permission of the copyright owner. Further reproduction prohibited without permission.

alternating layers of two materials with a large difference in the elastic constants. His argument was that a dislocation located in the layer of the less stiff material would be repelled from both interfaces of that layer due to the images appearing in all other layers. Since the layers are thin, a dislocation in one of the layers would be very close to its images in the nearby layers. As a result, the maximal resolved shear stress necessary to drive a dislocation through this laminate structure is of order of 1/100 of the smaller of the two shear moduli. This result has yet to be confirmed quantitatively by experimental or through more rigorous theory.

Another type of interface effect is related to the role played by interfaces in plasticity. A grain boundary can act as a barrier to slip thereby providing one of the most commonly exploited method for hardening polycrystalline materials [17]. A geometric requirement for a dislocation to be a able to propagate across an interface is that dislocation slip planes in both grains intersect along the line lying in the grain boundary plane [11]. Moreover, the condition of conservation of Burgers vectors in both grains must be satisfied. These two conditions only hold in special cases and are rarely satisfied. One way in which real materials overcome this difficulty is for the dislocation to split into partial dislocations, some of which propagate into the second grain leaving a residual partial dislocation in the grain boundary [18]. Other ways of crossing an interface are more indirect. An interface acting as an impermeable barrier for dislocations leads to a dislocation pile-up [11]. As the applied load increases, the stress at the tip of the pile up becomes sufficient to operate a dislocation source in the grain boundary leading to the formation of dislocations that propagate into the second grain (the source can also be in the second grain itself) [18]. The analysis of the stress field at the tip of a pile-up is often used to explain the increase in the yield stress of a material as the grain size decreases (i.e., the grain boundary area per unit volume increases). This effect is described by the Hall-Petch relation [19, 20] $\sigma_Y = \sigma_Y^0 + kd^{-1/2}$ where σ_Y denotes the yield stress of the

Reproduced with permission of the copyright owner. Further reproduction prohibited without permission.

material, d is the grain size, and k is the proportionality coefficient. Experimental studies show that the exponent of d in this relation varies from -1/3 to -1.

Interfaces are prone to sliding, thereby providing a mechanism for polycrystalline plasticity. This phenomenon typically occurs only at elevated temperatures ($T > 0.4\ T_m$) and may involve a variety of microscopic mechanisms. A phenomenological description of sliding of a flat interface is provided by replacing the interface with a narrow, Newtonian viscous region. The rate of shear in this model is proportional to the applied shear stress (a Maxwell solid) [21]. The analysis of sliding of non-planar interfaces tends to be more complicated, because asperities of the interlocked crystals block the shearing, and sliding needs to be accommodated. This accommodation is thought to occur by means of elastic, plastic or diffusional accommodation. The elastic method of accommodation is of interest as an example of elastic boundary conditions at an interface.

Elastic accommodation takes place in the case of a small degree of shear. In the analysis in Raj and Ashby [22], it is assumed that as the grains are shifted relative to each other, tractions develop along the interface due to the elastic contact between asperities at both sides of the boundary. These tractions only have a component normal to the interface, since the viscous interface cannot support shear. This is a manifestation of a "slipping interface" boundary conditions which is discussed in Chapter II. The analysis in Raj and Ashby [22] predicts a strain rate which is exponentially decaying with time at constant shear stress. Other equally important mechanisms of interfacial sliding (diffusional and plastic one) are beyond the scope of this thesis.

Interfaces provide fast diffusion channels through the material for both self diffusion and diffusion of impurities. An interface typically has a lower density than the surrounding material and, therefore, a higher than bulk concentration of equilibrium vacancies. These two factors account for both the lower activation energy of diffusion and higher atomic jump rate. The effect of high interfacial diffusivity is especially pronounced at low temperatures, when diffusion through the grains is slow (i.e., bulk

Reproduced with permission of the copyright owner. Further reproduction prohibited without permission.

diffusion has a significantly higher activation energy). As a result, the diffusant permeates into the material through interfaces (e.g.,, along the grain boundary network) and then diffuses away from the interfaces into the bulk of the grains. This effect has been studied experimentally by observing the concentration profile of the diffusant away from the grain boundaries [23].

The list of examples of interfacial effects presented above is not intended to be exhaustive, but rather shows the importance of interfaces for mechanical properties of materials. Another class of phenomena in materials related to interfaces is of a kinetic nature. As an interface separates two dissimilar pieces of material, any morphological changes in a material naturally involve interfaces. These changes may be stress driven, originating for example, from lattice misfit between the two materials meeting at the interface, curvature driven, such as grain growth, or stem from a discontinuity of the chemical potential across the interface, such as in phase transformations. The kinetic effects are discussed below.

1.3 Interfacial kinetics

The motion of an interface can be described phenomenologically using two related approaches. The first approach is based on the consideration of the driving force acting upon an element of the interface. This approach assumes that an interface responds linearly to the force, and the proportionality coefficient is referred to as the interface mobility. Such a description is typical for studies of grain boundary migration [24].

The other approach is more atomistic by nature. Instead of operating in terms of the force acting on an element of the interface, the difference in the chemical potential of atoms at both sides of the interface is considered. In equilibrium, these two approaches naturally result in the same solution for the position of the interface, i.e. the force acting on the interface is zero along the interface when the chemical potentials of atoms on both

Reproduced with permission of the copyright owner. Further reproduction prohibited without permission.

sides of the interface are equal (or vice versa). However, the second approach is more powerful when the system is not in equilibrium, as it is more easily generalized to include different microscopic mechanisms of atomic transport toward and along the interface. Since both of these approaches have their origin in thermodynamics, we are able to explain the result obtained with one in terms of the other.

Consider an interface S_0 separating two regions A and B. The interface at this position will serve as a reference point for the interfacial position and zero of energy. The total energy of the system with the interface displaced from S_0 can be characterized by the displacement vector $\delta\boldsymbol{\xi}(\mathbf{x})$, where $\mathbf{x}$ is the coordinate vector along the interface S_0. We assume that the vector $\delta\boldsymbol{\xi}$ is directed from side A to side B. The total energy of the system is a function of the displacement vector $\delta\boldsymbol{\xi}$.

$$E_{int} = E_{int}(\delta\boldsymbol{\xi}(\mathbf{x})) \tag{1}$$

The force acting on the interface (per unit length of the interface), $\boldsymbol{\tau}$ is defined as a variable conjugate to $\boldsymbol{\xi}$:

$$\boldsymbol{\tau}(\mathbf{x}) = -\frac{\delta E_{int}}{\delta\boldsymbol{\xi}(\mathbf{x})} \ . \tag{2}$$

Although referred to as "a force", $\boldsymbol{\tau}$ is essentially a tensor (τ_{ik} is the component of the force along the basis vector $\mathbf{e}_i$, produced by the displacement along the basis vector $\mathbf{e}_k$). This expression can be written in integral form as

$$-\delta E_{int} = \int_S \delta\boldsymbol{\xi}\boldsymbol{\tau} d\mathbf{S}. \tag{3}$$

In the absence of a chemical reaction (phase transformation), the total energy in the last expression consists of two distinct contributions: interfacial, for the lack of a better word, and elastic energies. Similarly, a force acting on the interface has two contributions. The interfacial contribution E_{int} is proportional to the area of the interface:

Reproduced with permission of the copyright owner. Further reproduction prohibited without permission.

$$E_{int} = \int_S \gamma dS \ , \tag{4}$$

and γ is the specific interfacial energy, similar to surface tension for a free surface. The variational derivative of the interfacial energy with respect to the displacement vector $\boldsymbol{\xi}$ is proportional to mean curvature κ of the interface [25]:

$$-\delta E_{int} = \int_S 2\gamma\kappa\delta\boldsymbol{\xi} d\mathbf{S}. \tag{5}$$

The elastic energy term E_{el} is written in terms of Eshelby's energy-momentum tensor $\mathbf{P}$:

$$-\delta E_{el} = \int_S \delta\boldsymbol{\xi}(\mathbf{P}_B - \mathbf{P}_A) d\mathbf{S} \tag{6}$$

where the subscripts A and B refer to sides A and B of the interface respectively. The energy-momentum tensor is defined as [26]:

$$\mathbf{P}_{ij} = W\delta_{ij} - \sigma_{ik}\frac{\partial \mathbf{u}_k}{\partial x_j} \tag{7}$$

where W is the local elastic energy density, σ_{ij} is the elastic stress tensor and $\mathbf{u}_i$ is the elastic displacement field. The reason that the elastic contribution to the force contains a term in addition to the elastic energy density is that the expression for the total elastic energy of the system E_{el} must include the potential energy of the loading system [26].

If the chemical nature of the materials on both sides of the interface are different(i.e., the chemical potentials μ_A^0 and μ_B^0 in the unstressed state are different)then the variation of the total energy of the system includes a "chemical" term which is simply

$$-\delta E_{chem} = \int_S (\mu_B^0 - \mu_A^0)\delta\boldsymbol{\xi} d\mathbf{S} \ . \tag{8}$$

Reproduced with permission of the copyright owner. Further reproduction prohibited without permission.

The most general expression for the tensor $\boldsymbol{\tau}$ is a sum of all three terms (Eqs. 5, 6, and 8). For convenience, we explicitly write this equation in coordinate form as:

$$\begin{aligned} -\delta E_{tot} &= \int_S \delta\xi_i \left(2\gamma\kappa\delta_{ij} + [\mu^0]\delta_{ij} + [\mathbf{P}_{ij}]\right) dS_j \\ &= \int_S \delta\xi_i \left(2\gamma\kappa\delta_{ij} + [\mu^0]\delta_{ij} + [W]\delta_{ij} - \sigma_{jk}\left[\frac{\partial \mathbf{u}_k}{\partial x_i}\right]\right) dS_j \end{aligned} , \tag{9}$$

where the notation [...] denotes the jump in the value across the interface.

Equation (9) is derived without any assumptions about the interface. If we assume, however, that the interface is "welded" as mentioned in Section 1.1 (continuity of displacements across the interface), than it is possible to show that Eq. (9) in fact defines the force normal to the interface (per unit length of an interface):

$$F = 2\gamma\kappa + [\mu^0] + [W] - \mathbf{T}\left[\frac{\partial \mathbf{u}}{\partial n}\right] . \tag{10}$$

where $\mathbf{T}$ is the surface traction vector at the interface and $\left[\frac{\partial \mathbf{u}}{\partial n}\right]$ is the discontinuity in the normal derivative of displacements. This normal force, along with the mobility of an interface, define the law of morphological evolution.

The chemical potential is defined in thermodynamics as a derivative of the Gibbs free energy with respect to the number of particles. It is easy to show that the jump in the chemical potential across the interface is simply the expression for the force normalized to the molar volume V_m:

$$[\mu] = V_m\left(2\gamma\kappa + [\mu^0] + [W] - \mathbf{T}\left[\frac{\partial \mathbf{u}}{\partial n}\right]\right) . \tag{11}$$

As expected, Eqs. (10) and (11) are equivalent when the system is in equilibrium.

A free surface is an important limiting case of an interface in solids. Surface properties are central in the processes of deposition, adsorption, crack nucleation, etc.

Reproduced with permission of the copyright owner. Further reproduction prohibited without permission.

The description of transport on the free surface of a stressed solid requires knowledge of the chemical potential of atoms at the surface. Similar to the case of an interface in a solid (Eq. 9), the total energy of a solid with a free surface under stress consists of three distinct contributions. We now focus on only the elastic term; the other two terms (the surface tension term and the chemical term) are similar to the case of an interface within a solid, described above.

The total elastic energy of a solid subjected to external loads involves the potential energy of the loading system [26] and the elastic energy stored in the body. In the case of hydrostatic loading, the volume of the solid is the only variable required to describe the mechanical state of the elastic body. In this case, the (elastic part of the) chemical potential of the solid is simply

$$\mu = \mu^0 + WV_m + P\overline{V}_m \tag{12}$$

where μ^0 is again the chemical potential of the solid in the unstressed state, W is the elastic energy density, V_m is the molar volume, P is the hydrostatic pressure and $\overline{V}_m$ denotes the molar volume of the stressed material.

If the load applied to the solid is not uniform, then the expression for the elastic part of the chemical potential becomes more complex. The complication is mainly due to the fact that a system with a nonhydrostatic loading is inherently nonequilibrium [27]. A number of authors [27-32] have computed the variation in the total elastic energy of a solid caused by adding an infinitesimal amount of material to the surface. This energy variation is directly related to the chemical potential at the surface. In short, the elastic part of the chemical potential is [32]:

$$\mu_{el} = \mu_0 + \left(\mathbf{P}_{ij} - \sigma_{ij}\right) n_i n_j V_m \tag{13}$$

Reproduced with permission of the copyright owner. Further reproduction prohibited without permission.

where the vector **n** is the normal to the surface, **P** is the Eshelby energy-momentum tensor (Eq. 7) and σ is the stress tensor. In case of a hydrostatic load, this expression reduces to Eq. (12).

In the problem addressed in Chapter III we consider transport along the traction-free surface. In this case, the chemical potential is determined by the local elastic energy density W.

A nonuniform chemical potential along the free surface creates a flux of matter **J** along the surface. This flux may result in shape changes provided the surface kinetics is sufficiently fast on the scale of the observation time. Mullins [33] delineates two main mechanisms of surface evolution. One of them is referred to as 'evaporation-condensation' where atoms evaporate from the surface at points of high chemical potential and get transferred through the vapor to surface locations with low chemical potential. In this case, the flux from (to) the surface is directly proportional to the difference in chemical potential between the surface and the vapor.

The second surface transport mechanism is surface diffusion. In this case, the flux **J** is proportional to the gradient of the chemical potential along the surface with the proportionality coefficient determined by the Nernst-Einstein relation [34]. The divergence of the flux **J**, again evaluated in the coordinates along the surface, results in the equation for the evolution of the surface profile. This equation will be used in Chapter III.

1.4 Dissertation overview

We investigate three problems showing various aspects of elastic effects at interfaces. In particular, the questions we address are: 1) the effects of elastic boundary conditions at an interface with an application of the results to the interactions between misfit dislocations and interfaces; 2) the morphological stability of a misfitting multilayer

Reproduced with permission of the copyright owner. Further reproduction prohibited without permission.

thin film during epitaxial growth, which combines both macroscopic thermodynamics and kinetics at the interface; and 3) the elastic interactions of defects on solid surfaces, which deals with a free-surface mediated interactions.

The goal of Chapter II is to develop an approach to describe appropriate elastic boundary conditions at interfaces. We investigate the role of elastic boundary conditions in the interaction between a source of stress within a bicrystal and the interface that separates the two (dissimilar) elastic half-spaces. A particular source of stress that we consider in detail is an edge dislocation with a Burgers vector parallel to the interface. To make the problem tractable analytically, we assume that the interface has a linear response to shear, i.e., the local tangential tractions are proportional to the jump (discontinuity) in tangential displacement across the interface. We derive a simple matrix expression which can be used to compute the stress field in the bicrystal originating from the dislocation-interface interaction. We derive the expression for the force acting on a single dislocation as well as on a periodic array of these dislocations with and without the presence of elastic misfit between the two materials meeting at the interface. From these results, we determine the conditions under which a dislocation (or an array of dislocations) will be attracted to or repelled from the interface or whether it (they) will stand-off from the interface at a finite distance.

Chapter III is dedicated to the study of the stability of a multilayer film during its heteroepitaxial growth. The evolution of the growing film is controlled by diffusion along the growth surface during the deposition. The nature and extent of the surface diffusion is controlled by the interplay between surface tension, the elastic strain energy arising from misfit, and the morphology of both the growing surface and buried interfaces. We present a linear stability analysis of the problem and identify possible microstructures of the multilayer films and the rates at which they evolve.

Chapter IV elucidates elastic aspects of interactions between defects (surface steps, adsorbed atoms) on solid surfaces (other types of interactions are important, such

Reproduced with permission of the copyright owner. Further reproduction prohibited without permission.

as entropic, electronic, etc.). In this chapter, to accomplish this task, we employ both elastic analyses and atomistic computer simulations. The simulations data are analyzed in terms of a 'dipole' model in which the defect is replaced by a surface force couple. We employ anisotropic linear elasticity to verify the validity of the dipole model in the description of elastic interactions between surface defects. We also determine the limit on the distance between the defects below which the linear model becomes invalid.

Chapter V concludes the dissertation, summarizing the main findings and suggesting some directions for future research.

Reproduced with permission of the copyright owner. Further reproduction prohibited without permission.

References to Chapter I

[1] A. Zangwill, *Physics at surfaces*, (Cambridge University Press: Cambridge, 1990).

[2] J. M. Howe, *Interfaces in materials*, (Wiley: New York, 1997).

[3] J. W. Cahn and J. E. Hillard, *J. Chem. Phys.*, **28**, 258 (1958).

[4] W. D. Kingery, *Introduction to ceramics*, 2nd ed., (Wiley: New York, 1976).

[5] A. P. Sutton and R. W. Balluffi, *Interfaces in crystalline materials*, (Clarendon Press: Oxford, 1995).

[6] S. Ranganathan, *Acta Cryst.*, **21** , 197 (1966).

[7] W. T. Read and W. Shockley, *Phys. Rev.*, **78**, 275 (1950).

[8] B. A. Bilby, *Report on the conference on defects in crystalline solids*, (The Physical Society: London , 1955).

[9] F. C. Frank, *Simposium on plastic deformation of crystalline solids*, (Office of Naval Research: Pittsburgh, Pennsylvania, 1950).

[10] W. Bollmann, *Crystal defects and crystalline interfaces*, (Springer-Verlag: Berlin, 1970).

[11] J. P. Hirth and J. Lothe, *Theory of dislocations*, 2nd ed., (Wiley: New York, 1982).

[12] F. C. Frank and J. H. v. d. Merwe, *Proc. Roy. Soc.*, **A198**, 205 (1949).

[13] J. W. Matthews and A. E. Blakeslee, *J. Cryst. Growth*, **27**, 118 (1974).

[14] A. K. Head, *Proc. R. Soc.*, **B66**, 793 (1953).

[15] J. Dundurs, in *Mathematical theory of dislocations*, ed. by T. Mura, (ASME: New York, 1969).

[16] J. S. Koehler, *Phys. Rev.*, **B2**, 547 (1970).

[17] F. A. McClintock and A. S. Argon, eds., *Mechanical behavior of materials*, (Addison-Wesley: Reading, Massachusetts, 1966).

[18] X. Baillin *et al*, *Phil. Mag.*, **A61**, 329 (1990).

[19] E. O. Hall, *Proc. Phys. Soc.*, **B64**, 747 (1951).

Reproduced with permission of the copyright owner. Further reproduction prohibited without permission.

[20] N. J. Petch, *J. Iron Steel Inst.*, **174**, 25 (1953).

[21] A. S. Nowick and B. S. Berry, *Anelastic relaxation in crystalline solids*, (Academic Press: New York, 1972).

[22] R. Raj and M. F. Ashby, *Met. Trans.*, **2**, 1113 (1971).

[23] I. Kaur and W. Gust, *Fundamentals of grain boundary diffusion*, (Ziegler Press: Stuttgart, 1989).

[24] G. Gottstein, D. A. Molodov and L.S. Shvindlerman, *Interface Sci.*, **6**, 7 (1998).

[25] C. Herring, in *The physics of powder metallurgy*, ed. by W. E. Kingston, (McGraw-Hill: New York,1951).

[26] J. D. Eshelby, in *Inelastic behavior of solids*, ed. by M.F. Kanninen *et al.*, (McGraw-Hill: New York,1970).

[27] J. C. M. Li, R. A. Orani, and L .S. Darken, *Z. Chem Neue Folge*, **49**, 271 (1966).

[28] W. B. Kamb, *J. Geophys. Res.*, **66**, 259 (1961).

[29] A. G. McLellan, *The chemical thermodynamics of deformable materials*, (Cambridge University Press: Cambridge, 1980).

[30] F. V. Nolfi, *J. Appl. Phys.*, **44**, 5245 (1973).

[31] M. S. Paterson, *Rev. Geophys. Space Phys.*, **11**, 355 (1973).

[32] B. J. Bartholomeusz, *Phil. Mag.*, **A71**, 489 (1995).

[33] W. W. Mullins, *J. Appl. Phys.*, **28**, 333 (1957).

[34] W. Jost, *Diffusion in solids, liquids, gases*, (Academic Press: New York, 1952).

Reproduced with permission of the copyright owner. Further reproduction prohibited without permission.

CHAPTER II

ELASTIC ANALYSIS OF FINITE STIFFNESS BIMATERIAL INTERFACES: APPLICATION TO DISLOCATION-INTERFACE INTERACTIONS

2.1 Introduction

Interfacial properties play an important role in a wide variety of materials phenomena, including grain boundary sliding, grain growth, intergranular fracture, faceting, fiber slipping in composites, etc. The mechanical properties of an interface are determined, in large part, by the nature of the chemical bonding at the interface, which may be significantly different from that within either of the materials meeting at the interface. This picture is further complicated by the presence of defects and/or compositional inhomogeneity at the interface.

The influence of interfaces on the mechanical properties of multiphase and polycrystalline materials is ubiquitous. Interfaces serve as barriers to dislocation motion and, as such, modify strength, as short circuit diffusion paths thereby modifying creep rates, as easy paths for crack propagation affecting toughness, etc. Interfaces also affect the elastic deformation of materials. From the point of view of continuum elasticity, an interface manifests itself through interfacial boundary conditions imposed upon the equations of elastic equilibrium. Typically, we assume that both the displacements and tractions are continuous across the interface. Such an interface is often referred to as "welded".

At elevated temperatures, interfacial diffusivities are often very high. An effective viscosity may be defined as inversely proportional to the diffusivity. Hence, when the

Reproduced with permission of the copyright owner. Further reproduction prohibited without permission.

interfacial diffusivity is very high, the interface may be viewed as liquid-like. As for liquids, this liquid-like interface cannot support a shear. To capture this physical effect, the elastic boundary conditions are commonly modified such that normal tractions and displacements are continuous across the interface and the shear traction is zero [1]. This is referred to as a "slipping" interface. Head [1] and Dundurs [2] studied various problems of interaction between an inclusion and a dislocation with such a "slipping" interface. Mura and Furuhashi [3] examined the effect of this type of boundary condition on an elliptical inclusion in shear. More recently, Kouris and Tsuchida [4] studied the interactions between two fibers in a composite material with such a boundary condition.

While both the "welded" and "slipping" interface boundary conditions are rigorously defined and have found wide applications, the appropriate boundary condition for most real interfaces lies somewhere in between these two extremes. One difficulty in determining an appropriate interfacial boundary condition is our incomplete knowledge of bonding at all but a few special interfaces. While first principles, electronic structure calculations of interfacial bonding have been performed, relatively few have examined the effect of shear [5]. One approach to correcting this deficiency is to develop a phenomenological model that approximates the bonding at interfaces [5]. Needleman [6] proposed an empirical (atomic bonding motivated) constitutive relation between the jump in the displacements vector across an interface and the tractions that this jump produces. In practice, this shear traction increases linearly with increasing displacement jump, goes through a maximum and then decays to zero. This method can be adopted for numerical calculations by using the finite element method to solve the mechanics problem in the two materials and describing the interfacial tractions in terms of the resultant jump in displacements. This approach was applied to crack propagation along an interface [7] and interfacial stability [8].

A simpler approach was proposed by Lene and Leguillon [9] to describe interfaces in composite materials. In their approach, the shear tractions exerted on the

Reproduced with permission of the copyright owner. Further reproduction prohibited without permission.

interface are assumed to vary linearly with the displacement jump across the interface. This may be thought of as replacing the interface with a thin layer of material and then letting the layer thickness go to zero at constant value of the product of the interfacial thickness and the shear modulus of the layer [10]. The advantage of this approach is that the linearity of the traction-displacement jump relation lends itself to analytical elasticity calculations. By adjusting the interfacial stiffness or spring constant, the mechanical response of the interface may be arbitrarily chosen. Lene and Leguillon [9, 10] employed this approach in determining the average elastic constants of a composite material. Using a homogenization approach, they found that the overall composite stiffness decreased rapidly with decreasing interfacial shear stiffness. Kouris and Mura [11] used this type of boundary condition and potential function approach to determine the elastic fields of an inclusion at a free surface.

This chapter presents a simple, analytical method for accounting for variations in interfacial properties on the elastic behavior of a two phase material. Such variations in interfacial properties may be related to segregation, changes in temperature or variations between material systems. Our approach is based upon the linear shear traction-displacement jump condition proposed by Lene and Leguillon [9] within a Green function framework. We illustrate the utility of this approach by considering the influence of interfacial properties on the elastic interactions between dislocations and interfaces. We consider both the case of a single dislocation and an array of misfit dislocations in heteroepitaxial systems.

2.2 Elastic analysis

In this section, we analyze the elastic fields associated with a source of stress in one of two semi-infinite materials which meet at an interface where the tractions are directly proportional to the jump in displacement. This is a very general approach since it

Reproduced with permission of the copyright owner. Further reproduction prohibited without permission.

accounts for materials of arbitrary elastic constants, a general source of stress (e.g., dislocation, misfitting homogeneous inclusion, etc.) and arbitrary interfacial stiffness. The latter is related to the bonding at the interface, local concentration, temperature, etc.

Consider two elastic half-spaces with shear moduli μ_1 and μ_2 and Poisson ratios, ν_1 and ν_2. It is convenient to write the Poisson ratios in terms of the parameter $k_\alpha = 3\text{-}4\nu_\alpha$ and introduce the Dundurs parameters for the two material: $\Gamma = \frac{\mu_2}{\mu_1}$, $A = \frac{1-\Gamma}{1+\Gamma k_1}$ and $B = \frac{k_2 - \Gamma k_1}{k_2 + \Gamma}$. These materials are joined along a plane, as indicated in Fig. 2.1.

We divide the stress field in materials **1** into two distinct parts: the stress field in material **1** due to the source of stress in the absence of an interface (i.e., in the infinite body) and the corrective fields added to insure that the boundary conditions at the interface are satisfied. In material **2**, no source of stress is present - hence, only the corrective fields are present in material **2**. Since the interface is planar, we limit the analysis to two spatial dimensions and all equations are linear (both the boundary conditions and the elastic equilibrium equations), the resulting elasticity problem may be solved by Fourier transforming both the stresses and displacements along the direction parallel to the interface (i.e., the x-axis in Fig. 2.1).

We begin the analysis by considering materials **1** and **2** separately, as if we made a cut along the interface. The tractions $\mathbf{T}_1$ on the surface of material **1** consist of two parts: we denote those produced by the source of stresses in an infinite medium (with constants μ_1 and ν_1) as **F** and those produced by the corrective solution (which assures that the boundary conditions at the interface are satisfied) as **P**:

$$\mathbf{T}_1 = \mathbf{P} + \mathbf{F} \quad . \tag{1}$$

Continuity of stresses across the interface requires that the tractions $\mathbf{T}_2$ on the surface of material **2** are equal and opposite to $\mathbf{T}_1$:

Reproduced with permission of the copyright owner. Further reproduction prohibited without permission.

$$\mathbf{T}_2 = -(\mathbf{P} + \mathbf{F}) \ . \tag{2}$$

We adopt the notation that the first component of all vectors is tangential to the interface (i.e., in the x-direction) and the second refers to the normal direction (i.e., the y-direction).

The elastic fields in materials **1** and **2** are obtained by solving the elastic equilibrium equations in the two half-spaces separately, subject to the traction distributions indicated in Eqs. (1) and (2), respectively. Following the procedure outlined by Sneddon [12], we solve these equations by Fourier transforming the problem in the direction parallel to the interface. The direct and inverse Fourier transforms of a quantity S are defined as

$$S(\xi) = \int_{-\infty}^{\infty} dx S(x) \exp(-i\xi x) \quad \text{and} \quad S(x) = \int_{-\infty}^{\infty} \frac{d\xi}{2\pi} S(\xi) \exp(i\xi x) \ ,$$

respectively.

The displacements on the surface of material **1** (denoted as $\mathbf{u}_1$) consist of the part due to the source of stress $\mathbf{u}_s$ in an infinite medium and that from the corrective solution. The latter may be written in terms of the surface Green function $\mathbf{G}_1(\xi)$ for material **1**. Hence,

$$\mathbf{u}_1 = \mathbf{G}_1(\xi)\mathbf{P} + \mathbf{u}_s \ . \tag{3}$$

$\mathbf{u}_1$, $\mathbf{u}_s$ and $\mathbf{P}$ are all functions of ξ. The surface Green function (i.e., the half-space Green function evaluated on $y = 0$) may be written explicitly as (see Appendix 2A)

$$\mathbf{G}_1(\xi) = \begin{pmatrix} \dfrac{k_1 + 1}{4\mu_1|\xi|} & -\dfrac{k_1 - 1}{4i\mu_1\xi} \\ \dfrac{k_1 - 1}{4i\mu_1\xi} & \dfrac{k_1 + 1}{4\mu_1|\xi|} \end{pmatrix} \tag{4}$$

Reproduced with permission of the copyright owner. Further reproduction prohibited without permission.

In the absence of a source of stresses in material **2** the displacements on the surface of material **2** are:

$$\mathbf{u}_2 = \mathbf{G}_2(\xi)\mathbf{T}_2 = -\mathbf{G}_2(\xi)(\mathbf{P}+\mathbf{F}) \tag{5}$$

where $\mathbf{G}_2$ is the (half-space) surface elastic Green function for material **2** (along $y = 0$), discussed in Appendix 2A,

$$\mathbf{G}_2(\xi) = \begin{pmatrix} \frac{k_2+1}{4\mu_2|\xi|} & \frac{k_2-1}{4i\mu_2\xi} \\ -\frac{k_2-1}{4i\mu_2\xi} & \frac{k_2+1}{4\mu_2|\xi|} \end{pmatrix} \tag{6}$$

Since both **F** and $\mathbf{u}_s$ represent the source of stress in material **1**, we can simplify the equations by writing $\mathbf{u}_s$ in terms of **F**. To do this, we replace the infinite space containing the source with two half-spaces (of material **1**). The displacement field $\mathbf{u}_s$ is found by contracting the tractions on the surface due to the source of stress (**F**) with the Green function of half-space **2** (which we imagine to be made of material **1**). Therefore, we write

$$\mathbf{u}_s = -\mathbf{G'}_2(\xi)\mathbf{F} \tag{7}$$

where the minus sign is associated with the fact that the normal to the surface of half-space **2** is opposite that for half-space **1**. $\mathbf{G'}_2$ is the Green function for half-space **2**, but consisting of material **1** and is simply $\mathbf{G}_2$ (Eq. 6), with all of the subscripts 2 replaced with 1:

$$\mathbf{G'}_2(\xi) = \begin{pmatrix} \frac{k_1+1}{4\mu_1|\xi|} & \frac{k_1-1}{4i\mu_1\xi} \\ -\frac{k_1-1}{4i\mu_1\xi} & \frac{k_1+1}{4\mu_1|\xi|} \end{pmatrix} \tag{8}$$

Reproduced with permission of the copyright owner. Further reproduction prohibited without permission.

Equations (1)-(8) describe the displacements and tractions on the surfaces of the two half-spaces, but not how these half-spaces are related. We do this by invoking the linear relation between the interfacial tractions and the jump in displacements at the interface [9], as described in Section 2.1, above. This is the "constitutive relation" for the interface:

$$\mathbf{T}_1 = \mathbf{K}(\mathbf{u}_2 - \mathbf{u}_1) \tag{9}$$

where the matrix $\mathbf{K}$ is a diagonal matrix of interfacial stiffnesses or springs constants:

$$\mathbf{K} = \begin{pmatrix} \kappa_t & 0 \\ 0 & \kappa_n \end{pmatrix} \tag{10}$$

κ_t represents the resistance of the interface to tangential motion (i.e., sliding) and κ_n represents the resistance of the interface to normal motion (i.e., opening). In general, the interfacial stiffness matrix may be non-diagonal, such that the application of a normal traction produces lateral displacements. While this is possible when the interface symmetry is low, such an effect would be absent in an isotropic continuum and therefore it is not considered here.

Combining Eqs. (1)-(10) we obtain a closed form, analytical expression for the corrective solution $\mathbf{P}$ in terms of $\mathbf{F}$, the interfacial stiffness matrix $\mathbf{K}$ and the Green functions:

$$\mathbf{P} = \left[\mathbf{G}_1 + \left(\mathbf{G}_2 + \mathbf{K}^{-1}\right)\right]^{-1}\left[\mathbf{G'}_2 - \left(\mathbf{G}_2 + \mathbf{K}^{-1}\right)\right]\mathbf{F} \quad . \tag{11}$$

Equation (11) is valid for an arbitrary interfacial stiffness matrix $\mathbf{K}$ (even a non-diagonal one). The usual "welded" interface boundary condition corresponds to $\kappa_n = \infty$, $\kappa_t = \infty$. In this case, $\mathbf{K}^{-1}$ vanishes entirely. If $\kappa_t = 0$ and $\kappa_n = \infty$, the interface can slip, but not open. This corresponds to the second element on the diagonal of the interface compliance matrix $\mathbf{K}^{-1}$ is zero.

Reproduced with permission of the copyright owner. Further reproduction prohibited without permission.

From the expression for the corrective solution, Eq. (11), we can find the half-space tractions (Eqs. 1 and 2). Contracting these with the full half-space Green functions yields the displacements and stresses (through Hooke's law) everywhere. Therefore, Eq. (11) provides a rigorous, analytical tool for examining the interaction of sources of stress (e.g., defects, misfitting homogeneous inclusions, etc.) with bimaterial interfaces. This differs from previous defect/interface interaction analyses in that it accounts for the properties of the interface itself (i.e., the interface is not simply where two materials meet). In the following section, we apply this new tool to the special case of dislocation/interface interactions with and without misfit between the two media.

2.3 Applications

A. Single dislocation near a bimaterial interface

As an example of the application of the interaction between a source of stress and a generalized interface, we examine the case of an edge dislocation with Burgers vector **b** parallel to the interface, as shown in Fig. 2.1. The distance between the dislocation line and the interface is denoted as c. Crudely, one can think of the dislocation creating an image in material **2** which, in turn, elastically interacts with the dislocation in material **1**. This interaction will create a climb force on the original dislocation, denoted $\mathbf{f}_y$, which will tend to move it closer to or away from the interface. This climb force can be obtained analytically using the formalism developed in the previous section.

The tractions produced by the dislocation $\mathbf{F}_d$ are obtained by Fourier transforming the stress field of an edge dislocation with **b** parallel to the interface [13]

Reproduced with permission of the copyright owner. Further reproduction prohibited without permission.

$$\mathbf{F}_d = \begin{pmatrix} \frac{2\mu_1 b}{k_1+1}\text{sign}(\xi)i(1-c|\xi|)\exp(-c|\xi|) \\ -\frac{2\mu_1 b}{k_1+1}c|\xi|\exp(-c|\xi|) \end{pmatrix} . \tag{12}$$

Inserting the traction due to the dislocation, Eq. (12), into Eq. (11) yields an expression for the corrective traction **P**. Given, the traction **P** at the surface of half space **1**, we obtain the stress field anywhere in that half space (see Eq. 2A.4). The climb force $\mathbf{f}_y$, on the original dislocation may be found directly in terms of these stresses through the Peach-Koehler equation [13]:

$$\mathbf{f}_y = -b\sigma_{xx}\big|_{x=0,y=c} . \tag{13}$$

The Fourier transform of the σ_{xx} component of the stress tensor can be obtained by multiplying the vector **P** by the vector $\mathbf{W}_{xx}(\xi,y)$ (as discussed in Appendix 2A), where

$$\mathbf{W}_{xx}(y) = \begin{pmatrix} sign(\xi)i(2-|\xi|y) \\ (|\xi|y-1) \end{pmatrix}\exp(-|\xi|y) \tag{14}$$

(see Appendix 2A). In order to determine the Peach-Koehler force on the dislocation, we must inverse Fourier transform $\sigma_{xx}(\xi,y)$ at $x = 0$ and $y = c$.

Before determining the climb force on the dislocation for arbitrary interface stiffness, we consider the two limiting, no opening ($\kappa_n = \infty$), cases: $\kappa_t = \infty$ and $\kappa_t = 0$. $\kappa_t = \infty$ corresponds to "welded" interface boundary condition. The climb force on the dislocation is given in terms of the inverse Fourier transform of $\sigma_{xx}(\xi,y)$ (which is symmetric with respect to the variable of integration ξ)

$$\begin{aligned} \mathbf{f}_y &= -\frac{b^2\mu_1}{\pi(k_1+1)}\int_0^{\infty} d\xi \exp(-2\xi c)(3A+B-8A(\xi c)+4A(\xi c)^2) \\ &= -\frac{b^2\mu_1}{2\pi(k_1+1)c}(A+B) \end{aligned} \tag{15}$$

Reproduced with permission of the copyright owner. Further reproduction prohibited without permission.

This is identical to the climb force on a dislocation near a bimaterial, "welded" interface found by Head [1] and Dundurs and Sendeckyj [14]. Assuming equal Poisson ratios of the two materials, the dislocation is repelled from the interface if the material containing the dislocation is the more compliant of the two and, otherwise, attracted. The case in which the Poisson ratios of the two materials differ is discussed in detail in Ref. [14].

The "slipping" interface boundary condition implies $\kappa_r = 0$ and $\kappa_s = \infty$. In this case, the climb force is

$$\begin{aligned} \mathbf{f}_y &= -\frac{b^2\mu_1}{\pi(k_1+1)}\int_0^{\infty} d\xi \exp(-2\xi c)\left(4-4(\xi c)+4\frac{((\xi c)^2-(\xi c))}{A+B-2}(AB-1)\right) \\ &= -\frac{b^2\mu_1}{\pi(k_1+1)c} \end{aligned} \tag{16}$$

This solution was also found by Dundurs [2]. When the interface is "slipping", the dislocation with a Burgers vector parallel to the interface is always attracted to the interface, independent of the elastic properties of either material. The magnitude of the force is completely independent of the elastic constants of the material across the interface from the dislocation.

We now turn to the more general case of a dislocation near an interface with a finite, non-zero stiffness. In this case, the expression for $\sigma_{xx}(0,c)$ (from the inverse Fourier transform of $\sigma_{xx}(\xi,c)$) in the climb force is more complicated than in either of the two special cases

Reproduced with permission of the copyright owner. Further reproduction prohibited without permission.

$$\mathbf{f}_y = -\frac{b^2\mu_1}{\pi(k_1+1)}\int_0^{\infty} d\xi \exp(-2\xi c)\left[4-4(\xi c)\left(A-\frac{(A-1)^2}{A+B-2}+1\right)+4(\xi c)^2\left(A-\frac{(A-1)^2}{A+B-2}\right)\right]$$

$$-\frac{b^2\mu_1}{\pi(k_1+1)}\left[\int_0^{\infty} d\xi \exp(-2\xi c)(3A+B-4)\frac{\kappa_t}{\kappa_t+\xi\dfrac{\mu_1\Gamma A(A+B-2)}{(A-1)(1-\Gamma)}}\right.$$

$$-\int_0^{\infty} d\xi \exp(-2\xi c)\left[A+\frac{(A-1)^2}{A+B-2}-1\right]\frac{4\kappa_t(\xi c)}{\kappa_t+\xi\dfrac{\mu_1\Gamma A(A+B-2)}{(A-1)(1-\Gamma)}} \qquad (17)$$

$$\left.+\int_0^{\infty} d\xi \exp(-2\xi c)\frac{(A-1)^2}{A+B-2}\frac{4\kappa_t(\xi c)^2}{\kappa_t+\xi\dfrac{\mu_1\Gamma A(A+B-2)}{(A-1)(1-\Gamma)}}\right]$$

The integrals in Eq. (17) can be written explicitly in terms of exponential integrals (see Appendix 2B):

$$\mathbf{f}_y = -\frac{b^2\mu_1}{\pi(k_1+1)c}\left[\frac{A+B}{2}-\frac{A+B-2}{2}e^{\alpha}\,\mathrm{Ei}(2,\alpha)\right.$$

$$\left.+\frac{(A-1)^2}{A+B-2}\left(2e^{\alpha}\,\mathrm{Ei}(3,\alpha)-3e^{\alpha}\,\mathrm{Ei}(4,\alpha)\right)+(A-1)\left(2e^{\alpha}\,\mathrm{Ei}(3,\alpha)-e^{\alpha}\,\mathrm{Ei}(2,\alpha)\right)\right], \qquad (18)$$

where $\alpha = \dfrac{2c\kappa_t(A-1)(1-\Gamma)}{\mu_1\Gamma A(A+B-2)} = \dfrac{2c\kappa_t(\mu_1^2k_2+\mu_2^2k_1+\mu_1\mu_2+\mu_1\mu_2k_1k_2)}{\mu_1\mu_2(\mu_1+\mu_2+\mu_1k_2+\mu_2k_1)}$ and the exponential integral $\mathrm{Ei}(n,\alpha) \equiv \int_1^{\infty} dt\dfrac{e^{-\alpha t}}{t^n}$. It is interesting to note that only the first terms in Eqs. (17) and (18) remain in the $\kappa_t = 0$ limit (i.e., the first terms corresponds to the "slipping" interface result).

In order to simplify the discussion of the effect of the interfacial stiffness, we first consider the case of a grain boundary (i.e., materials **1** and **2** have the same elastic constants, i.e., $\Gamma = 1$). In this limit, Eq. (18) is considerably simplified:

$$\mathbf{f}_y = -\frac{b^2\mu_1}{\pi(k_1+1)c}\left[2e^{\alpha}\,\mathrm{Ei}(2,\alpha)-3e^{\alpha}\,\mathrm{Ei}(3,\alpha)+\frac{3}{2}e^{\alpha}\,\mathrm{Ei}(4,\alpha)\right], \qquad (19)$$

Reproduced with permission of the copyright owner. Further reproduction prohibited without permission.

where α goes to $\alpha' = \frac{c\kappa_t(k_1+1)}{\mu_1}$ in the $\mu_1 = \mu_2$, $\nu_1 = \nu_2$ limit. Analysis of Eq. (19) shows that the dislocation is attracted toward the grain boundary for all finite values of the interfacial stiffness κ_t. Only in the limit that κ_t goes to infinity, does the attractive force between the dislocation and grain boundary disappear. This case corresponds to a dislocation in an infinite medium (i.e., the grain boundary is no different than the rest of the material). The variation of the force on the dislocation with dislocation separation for the case of a grain boundary is shown below, where we discuss the more general dislocation/interface interaction problem.

To facilitate the analysis of the general case of the interaction between a dislocation and a bimaterial interface, we set the Poisson ratios of both materials equal to 1/3. The dependence of the normalized climb force $\mathbf{f}_y^*$ ($= \frac{\mathbf{f}_y \pi(k_1+1)}{\mu_1 b}$) on the separation between the dislocation and the interface, c, as per Eq. (18), is shown in Fig. 2.2 for $\kappa_t b/\mu_1 = 1$ and $\Gamma = 10$ and $\Gamma = 0.5$. For $\Gamma < 1$ a dislocation is attracted toward the interface for all dislocation-interface separations. On the other hand, for $\Gamma > 1$ the dislocation is repelled from the interface at large dislocation-interface separation and attracted at small separation. This implies the existence of an unstable equilibrium separation for $\Gamma > 1$. The unstable equilibrium separation c^* decreases with increasing Γ, as shown in Fig. 2.3. For all values of $c > c^*$ and $\Gamma > 1$, dislocations are repelled from the interface and for $c < c^*$. For all values of Γ, the climb force $\mathbf{f}_y$ asymptotically approaches zero as the dislocations move further away from the interface.

The dislocation climb force, represented by Eq. (18), exhibits an inverse dependence on the dislocation-interface separation $1/c$ times a more complicated, α-dependent term. In order to understand this c-dependence in more detail, we plot $\frac{\mathbf{f}_y^* c}{b}$ (normalized as indicated in the figure) versus $\kappa_t c/\mu_1$ in Fig. 2.4 for several different values of the modulus ratio Γ ($\Gamma = 1$ corresponds to the grain boundary case). For all Γ,

Reproduced with permission of the copyright owner. Further reproduction prohibited without permission.

the normalized force $\frac{\mathbf{f}_y^c}{b}$ goes to -1 as the interface stiffness goes to zero. In this limit, the interface is a "slipping" interface (see Eq. 16). As the interface stiffness and/or the dislocation-interface separation increases, $\mathbf{f}_y^c$ increases monotonically and asymptotically approaches a constant value at large κ_i^c. This asymptotic value may be found from the dislocation-interface interaction result in the "welded" interface limit, Eq. (15) (i.e., $-(A+B)/2$). In the special case of a grain boundary ($\Gamma = 1$), this asymptotic value is exactly zero (i.e., the dislocation is neither attracted to nor repelled from a grain boundary with $\kappa_i = \infty$).

The present results demonstrate that under conditions where the dislocation is normally repelled from the interface (i.e., in the "welded" case), it is still repelled from the interface at large dislocation-interface separation and attracted toward the interface at small dislocation-interface separations. Under conditions where the dislocation is normally attracted toward the interface (i.e., in the "slipping" case), changing the interfacial stiffness does not reverse this. The magnitude of the attraction or repulsion is a function of the interfacial stiffness, κ_i. In the next section we generalize the present results to the case of an array of dislocations near an interface separating two materials that are misfitting with respect to one another.

B. Dislocation array near a bimaterial interface

When the two materials meeting at a bimaterial interface are misfitting with respect to one another, the resulting misfit stresses can be relieved by the presence of a dislocation array of suitable Burgers vector and spacing [15]. Therefore, we now consider an array of equally spaced dislocations in material **1** near the interface. If the elastic constants of the two materials are different, the dislocations may be displaced from the interface (e.g., [16, 17]). For the sake of concreteness, we assume that material **1** is less stiff than material **2** and the lattice parameter of material **1** is smaller than that of material

Reproduced with permission of the copyright owner. Further reproduction prohibited without permission.

2 (see the geometry in Fig. 2.5). In this case, two forces act on the dislocations: the first one is a climb force which repels the dislocation from the stiffer material. The second one is caused by the misfit and is known as the coherency force. Since material 1 is in compression, the force on the dislocations with the Burgers vectors oriented as in Fig. 2.5 is negative, indicating that the misfit attracts the dislocation to the interface. As a result of the interplay between these two forces, an elastic constant and misfit strain dependent equilibrium stand-off distance may exist. Gutkin *et al* [18] and Mader and Knauss [19] determined this stand-off distance in the "welded" interface limit. We investigate this stand-off distance for the "slipping" and "welded" interface and for all interface stiffnesses in between. We first calculate the magnitude of the climb force acting on an array of misfit dislocations in the absence of misfit and then determine the influence of the misfit. This yields a general expression for the misfit dislocation stand-off distance for arbitrary material properties and interface stiffness.

Consider an array of edge dislocations with Burgers vector **b** oriented parallel to and a distance c from the interface in material 1 and separated from each other by a distance d (Fig. 2.5). The climb force $\mathbf{f}_y$ can be obtained, as in the single dislocation case, by considering the interaction with the corrective solution (Eq. 13). Summing the resultant corrective solution over all of the dislocations in the array yields the climb force on each dislocation:

$$\mathbf{f}_y = -b\sum_{n=-\infty}^{\infty}\sigma_{xx}(nd,c) \quad , \tag{20}$$

where $\sigma_{xx}(x,y)$ is the stress field produced by the corrective solution used for a single dislocation. To compute this infinite sum, we make use of Poisson's formula:

$$\sum_{n=-\infty}^{\infty}\sigma_{xx}(nd,c) = \frac{1}{d}\sum_{k=-\infty}^{\infty}\int_{-\infty}^{\infty}dx\sigma_{xx}(x,c)e^{-2\pi ikx/d} \quad . \tag{21}$$

Reproduced with permission of the copyright owner. Further reproduction prohibited without permission.

The terms on the right-hand-side of Eq. (21) are Fourier coefficients of σ_{xx}.

As for the single dislocation near an interface, we consider two limiting cases ($\kappa_f = \infty$ and $\kappa_f = 0$) before examining the general case. In the "welded" interface limit ($\kappa_f = \infty$), we may rewrite Eq. (21) explicitly as

$$\mathbf{f}_y = -\frac{b^2\mu_1}{(k_1+1)}\sum_{n=-\infty}^{\infty}\frac{\exp(-4\frac{|n|\pi c}{d})}{d}\left(3A+B-8A(\frac{2|n|\pi c}{d})+4A(\frac{2|n|\pi c}{d})^2\right) . \qquad (22)$$

Since the function within the summation is even, this equation can be rewritten as:

$$\mathbf{f}_y = -\frac{b^2\mu_1}{(k_1+1)}\left[\frac{3A+B}{d}+2\sum_{n=1}^{\infty}\frac{\exp(-4\frac{n\pi c}{d})}{d}\left(3A+B-8A(\frac{2n\pi c}{d})+4A(\frac{2n\pi c}{d})^2\right)\right] , \qquad (23)$$

where the first term corresponds to the $n = 0$ Fourier coefficient. The summation of this series yields (see Appendix 2C):

$$\mathbf{f}_y = -\frac{b^2\mu_1}{(k_1+1)d}\left[3A+B+\frac{(3A+B)e^{-\Lambda}}{\sinh\Lambda}-\frac{4A\Lambda}{\sinh^2\Lambda}+\frac{2A\Lambda^2\cosh\Lambda}{\sinh^3\Lambda}\right] , \qquad (24)$$

where $\Lambda = \frac{2\pi c}{d}$. This expression was previously obtained by Gutkin *et al.* [18] and by Mader and Knauss [19]. As the stand-off distance c of the array approaches infinity, the climb force acting on a dislocation asymptotically approaches a constant value $\mathbf{f}_y = -\frac{b^2\mu_1}{(k_1+1)d}(3A+B)$. For the simple case when the Poisson's ratios of both materials are the same, this force is positive (i.e., dislocations are repelled from the interface) when the Dundurs parameter Γ is greater than 1.

Following the same approach that led to Eq. (24), we obtain the climb force for the "slipping" interface ($\kappa_f = 0$) case:

Reproduced with permission of the copyright owner. Further reproduction prohibited without permission.

$$\mathbf{f}_y = -\frac{b^2\mu_1}{(k_1+1)d}\left[4+4\frac{e^{-\Lambda}}{\sinh\Lambda}-\frac{\Lambda}{\sinh^2\Lambda}(2+2\frac{AB-1}{A+B-2})+\frac{2(AB-1)}{A+B-2}\frac{\Lambda^2\cosh\Lambda}{\sinh^3\Lambda}\right] \quad (25)$$

As the stand-off distance c of the array approaches infinity, the climb force acting on the dislocations asymptotically approaches a constant value which is negative (i.e., dislocations are attracted to the interface) regardless of the elastic constants of the materials.

We now turn to the general case, where the interface has a finite stiffness. The climb force $\mathbf{f}_y$ can be expressed in terms of a Fourier series $\mathbf{f}_y = \sum_{n=-\infty}^{\infty}\mathbf{f}_n$ (evaluated at $x = 0$) with Fourier coefficients $\mathbf{f}_n$:

$$\mathbf{f}_n = -\frac{b^2\mu_1}{(k_1+1)}\frac{\exp(-2|n|\Lambda)}{d}\left[4-4(\Lambda|n|)\left(A-\frac{(A-1)^2}{A+B-2}+1\right)+4(\Lambda|n|)^2\left(A-\frac{(A-1)^2}{A+B-2}\right)\right.$$
$$\left.+(3A+B-4)\frac{1}{1+\frac{2|n|\Lambda}{\alpha}}-\left(A+\frac{(A-1)^2}{A+B-2}-1\right)\frac{4(|n|\Lambda)}{1+\frac{2|n|\Lambda}{\alpha}}+\frac{(A-1)^2}{A+B-2}\frac{4(|n|\Lambda)^2}{1+\frac{2|n|\Lambda}{\alpha}}\right] \quad (26)$$

As before, we make use of the symmetry of the Fourier coefficients to obtain the climb force as:

$$\mathbf{f}_y = -\frac{b^2\mu_1}{(k_1+1)d}\left(\left[(3A+B)+4\frac{e^{-\Lambda}}{\sinh\Lambda}-\frac{\Lambda}{\sinh^2\Lambda}2\left(A-\frac{(A-1)^2}{A+B-2}+1\right)\right.\right.$$
$$\left.+2\left(A-\frac{(A-1)^2}{A+B-2}\right)\frac{\Lambda^2\cosh\Lambda}{\sinh^3\Lambda}\right]+2\sum_{n=1}^{\infty}\exp(-2n\Lambda) \quad (27)$$
$$\left.\left[(3A+B-4)\frac{1}{1+\frac{2n\Lambda}{\alpha}}-\left(A+\frac{(A-1)^2}{A+B-2}-1\right)\frac{4(n\Lambda)}{1+\frac{2n\Lambda}{\alpha}}+\frac{(A-1)^2}{A+B-2}\frac{4(n\Lambda)^2}{1+\frac{2n\Lambda}{\alpha}}\right]\right).$$

This summation can be evaluated explicitly in terms of incomplete beta-functions, B, using the method outlined in Appendix 2C.

Reproduced with permission of the copyright owner. Further reproduction prohibited without permission.

$$
\begin{aligned}
f_y = &-\frac{b^2\mu_1}{(k_1+1)d}\left[3A+B+(3A+B)\frac{e^{-\Lambda}}{\sinh\Lambda}-\frac{4A\Lambda}{\sinh^2\Lambda}+\frac{2A\Lambda^2\cosh\Lambda}{\sinh^3\Lambda}\right] \\
&+\frac{b^2\mu_1}{(k_1+1)d}e^{\beta\Lambda}\left[(3A+B-4)2\mathrm{B}_{exp(-2\Lambda)}(\frac{\beta}{2}+1,-1)\right. \\
&-\left(A+\frac{(A-1)^2}{A+B-2}-1\right)8\Lambda\left(2\mathrm{B}_{exp(-2\Lambda)}(\frac{\beta}{2}+1,-2)-\mathrm{B}_{exp(-2\Lambda)}(\frac{\beta}{2}+1,-1)\right) \\
&\left.+\frac{(A-1)^2}{A+B-2}8\Lambda^2\left(\mathrm{B}_{exp(-2\Lambda)}(\frac{\beta}{2}+1,-1)-6\mathrm{B}_{exp(-2\Lambda)}(\frac{\beta}{2}+1,-2)+6\mathrm{B}_{exp(-2\Lambda)}(\frac{\beta}{2}+1,-3)\right)\right],
\end{aligned}
\tag{28}
$$

where $\beta = \alpha/\Lambda$ only depends on materials parameters, such as the misfit, elastic constants, interfacial stiffness. Equation (28) reduces directly to the "welded" interface solution (Eq. 24) by setting $\kappa_t = \infty$ or, equivalently, $\beta = \infty$. The "slipping" interface result (Eq. 25) cannot be directly recovered by substituting $\kappa_t = 0$ or, equivalently, $\beta = 0$ into Eq. (28). This may be traced back to the fact that the value of the $n = 0$ Fourier coefficient for $\kappa_t = 0$ in Eq. (26) is different depending on the order in which we allow n and κ_t to go to zero. The "slipping" interface solution may be obtained from Eqs. (26)-(28) by allowing κ_t (α) to go to zero before taking the $n = 0$ limit in Eq. (26).

We now address the issue of the force on the dislocation array associated with the misfit between materials **1** and **2**. The misfit between the two materials can always be described in terms of a continuous distribution of dislocations at the interface [20]. If we assume that the dislocation array in Fig. 2.5 completely relieves the misfit, then the Burgers vector density associated with this uniform distribution of dislocations at the interface must be *b/d* [20]. The stress fields associated with this dislocation distribution at the bi-material interface may be obtained by integrating the stress field of a single dislocation (with the burgers vector replaced by the misfit strain, which is equal to *b/d*) at a bimaterial interface [21] along the entire interface. This stress field results in a climb force on each dislocation in the dislocation array in Fig. 2.5 which may be determined from the Peach-Koehler relation. The magnitude of the force due to the misfit is:

Reproduced with permission of the copyright owner. Further reproduction prohibited without permission.

$$\mathbf{f}_m = \frac{b^2\mu_1}{(k_1+1)d}(3A+B-4) \quad . \tag{29}$$

The total force acting on a dislocation F is a sum of the forces in Eq. (28) and (29)

$$F = \mathbf{f}_y + \mathbf{f}_m \quad . \tag{30}$$

In order to simplify the remaining analysis, we work in terms of the normalized climb force $F^* = \frac{F(k_1+1)d}{b^2\mu_1}$ and we arbitrarily set the Poisson ratios of both materials to 1/3. Using these choices, the force acting on the array of dislocations depends on three dimensionless parameters: the Dundurs parameter Γ, the normalized separation between the interface and the dislocation array Λ and a parameter $\frac{\kappa_1 d}{\mu_1}$, which enters Eq. (28) through the parameter β.

Figure 2.6 shows the dependence of the normalized climb force F^* on the normalized distance between the dislocation array and the interface $\Lambda(= 2\pi c/d)$ for infinite κ_r ("welded" interface) for a range of values of the Dundurs parameter Γ. Two distinct types of behavior may be seen. For $\Gamma > 1$, the force acting on the dislocation array is repulsive for small values of Λ, asymptotically approaching infinity as Λ approaches zero, and attractive for large values. A stable equilibrium Λ exists, which corresponds to an equilibrium dislocation array stand-off distance from the interface [19]. For $\Gamma \leq 1$, the dislocations are attracted to the interface at all separations. Finally, when $\Gamma = 1$, the force on the dislocations is constant and attractive ($F = -4$, in normalized units).

The variation of the force on the dislocation array as a function of the separation from the interface, in the "slipping" interface limit, $\kappa_r \rightarrow 0$, is shown in Fig. 2.7. In this limit, the force F is attractive at all dislocation/interface separations and for all values of the Dundurs parameter Γ. This normalized force diverges as Λ goes to zero and is asymptotic to -4 as Λ approaches ∞. The dependence on the Dundurs parameter Γ is insignificant.

Reproduced with permission of the copyright owner. Further reproduction prohibited without permission.

Figure 2.8 shows the variation of the force on the dislocations with distance from the interface for a case in which the interface is intermediate between "slipping" and "welded": i.e., $\frac{\kappa_i d}{\mu_1} = 50$. This force is attractive for all values of Λ when $\Gamma \leq 1$ and asymptotically approaches -4 (in normalized units) for all values of Γ and $\frac{\kappa_i d}{\mu_1}$. As the Dundurs parameter Γ continues to increase, a maximum in the force vs. separation curve occurs. For $\Gamma > \Gamma_c$ this maximum corresponds to a repulsive force over a finite range of Λ (for $\frac{\kappa_i d}{\mu_1} = 50$, $\Gamma_c \approx 5.15$). Since F tends to $-\infty$ as $\Lambda \rightarrow 0$ and $F \rightarrow -4$ (normalized units) as $\Lambda \rightarrow \infty$, a maximum force greater than zero implies the presence of two equilibrium points (separations). The one at the smaller Λ, Λ_1, is always unstable and the one at the larger Λ, Λ_0, is stable. Therefore, for all $\Lambda < \Lambda_1$, the dislocation is attracted to the interface, while for all $\Lambda > \Lambda_1$ the dislocations are attracted to the equilibrium stand-off separation Λ_0. As the magnitude of $\frac{\kappa_i d}{\mu_1}$ increases further, Λ_1 decreases.

The dependence of the stable equilibrium point/misfit dislocation stand-off distance Λ_0 on the Dundurs parameter Γ and $\frac{\kappa_i d}{\mu_1}$ is shown in Fig. 2.9. In the "welded" interface case, an equilibrium stand-off distance exists for all values of the Dundurs parameter greater than 1. For a fixed value of Γ, the magnitude of the equilibrium stand-off distance decreases with decreasing interface stiffness. This is not surprising, since the repulsive component of the climb force decreases with decreasing interface stiffness κ_i. Since the equilibrium stand-off distance observed in several experiments (see e.g., [16, 17]) is greater than that predicted based on this and similar analyses [18, 19] in the "welded" interface limit and that presented here in the case of finite stiffness interfaces, the introduction of finite stiffness interfaces does not resolve the discrepancies between experiment and theory.

2.4 Conclusions

Reproduced with permission of the copyright owner. Further reproduction prohibited without permission.

In this chapter, we presented an easily applied method for determining the elastic fields in problems containing bimaterial interfaces of arbitrary stiffness. This analytical approach is useful for the common situation in which the classical "welded" and "slipping" interface elastic boundary conditions do not adequately describe the interface. As an application of this method, we determined the climb force acting on an individual edge dislocation and an array of such dislocations near a bimaterial interface. For the case of an individual dislocation, we found that an unstable dislocation-interface equilibrium separation exists, above which the dislocation is repelled and below which it is attracted to the interface, provided that the material containing the dislocation is more compliant than that across the interface and that the interface is neither perfectly "welded" nor "slipping".

When the two materials meeting at the interface are misfitting with respect to one another, the misfit is commonly relieved by the formation of a misfit dislocation array. When the interface is "slipping", the dislocations always reside at the interface. However, when the interface is "welded" and the material containing the dislocations is less stiff than that on the other side of the interface, the misfit dislocations may stand-off from the interface, as seen experimentally. In the case in which the dislocations are repelled from the interface in the welded interface limit, replacing the welded interface with one of finite stiffness, either decreases the equilibrium stand-off distance or results in no stand-off at all (i.e., the dislocation/interface separation is zero), depending on the relative elastic properties of the two materials, as represented by the Dundurs parameter. This stand-off distance decreases with the decrease of the interface stiffness. Even when a finite stand-off distance does exists in the finite stiffness interface case, there is a dislocation/interface separation smaller than which the dislocation array is attracted into the interface.

Reproduced with permission of the copyright owner. Further reproduction prohibited without permission.

References to Chapter II

[1] A. K. Head, *Proc. Roy. Soc. (London)*, **B66**, 793 (1953).

[2] J. Dundurs, in *Mathematical theory of dislocations*, ed. by T. Mura, (ASME: New York, 1969).

[3] T. Mura and R. Furuhashi, *J. Appl. Mech.*, **51**, 308 (1984).

[4] D. Kouris and E. Tsuchida, *Mechanics of Materials*, **12**, 131 (1991).

[5] G. Bozzolo, J. Ferrante and J. R. Smith, *Scripta Met.*, **25**, 1927 (1991).

[6] A. Needleman, *J. Appl. Mech.*, **54**, 525 (1987).

[7] A. Needleman, *J. Mech. Phys. Solids* **38**, 289 (1990).

[8] Z. Suo, M. Ortiz, and A. Needleman, *J. Mech. Phys. Solids*, **40**, 613 (1992).

[9] F. Lene and D. Leguillon, *Int. J. Solids Structures*, **18**, 443 (1982).

[10] F. Lene and D. Leguillon, *Journal de Méchanique*, **20**, 511 (1981).

[11] D. A. Kouris and T. Mura, *J. Mech. Phys. Solids*, **37**, 365 (1989).

[12] I. N. Sneddon, *Fourier transforms*, (McGraw-Hill: New York, 1951).

[13] J. P. Hirth and J. Lothe, *Theory of dislocations*, 2nd ed., (Wiley: New York 1982).

[14] J. Dundurs and G. P. Sendeckyj, *J. Appl. Phys.*, **36**, 3353 (1965).

[15] F. C. Frank and J. H. v. d. Merwe, *Proc. Roy. Soc. (London)*, **A198**, 205 (1949).

[16] W. Mader, *Z. Metallk.*, **80**, 139 (1989).

[17] D. X. Li *et al*, *Acta metall. Mater.*, **40 Suppl**, S327 (1992).

[18] M. Y. Gutkin *et al Phys. Stat. Sol. (a)*, **113**, 337 (1989).

[19] W. Mader and D. Knauss, *Acta metall. Mater.*, **40 Suppl.**, S207 (1992).

[20] J. P. Hirth, D.M. Barnett, and J. Lothe, *Phil. Mag.*, **A40**, 39 (1979).

[21] J. Dundurs and T. Mura, *J. Mech. Phys. Solids*, **12**, 177 (1964).

[22] R. E. Eykholt, personal communication.

Reproduced with permission of the copyright owner. Further reproduction prohibited without permission.

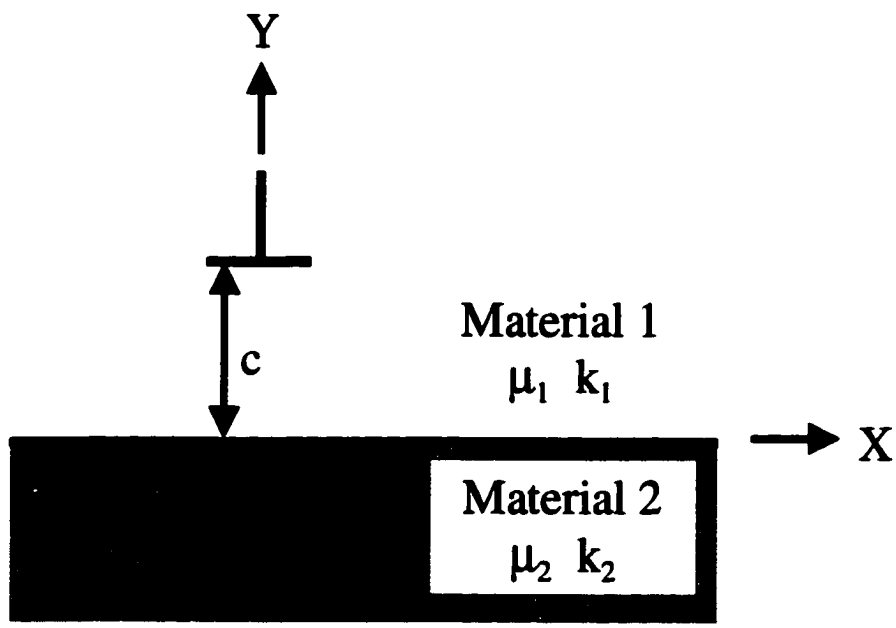


Figure 2.1. An illustration of the configuration employed in the analysis of the interaction between the source of stress (indicated by a dislocation) and a bimaterial interface.

Reproduced with permission of the copyright owner. Further reproduction prohibited without permission.

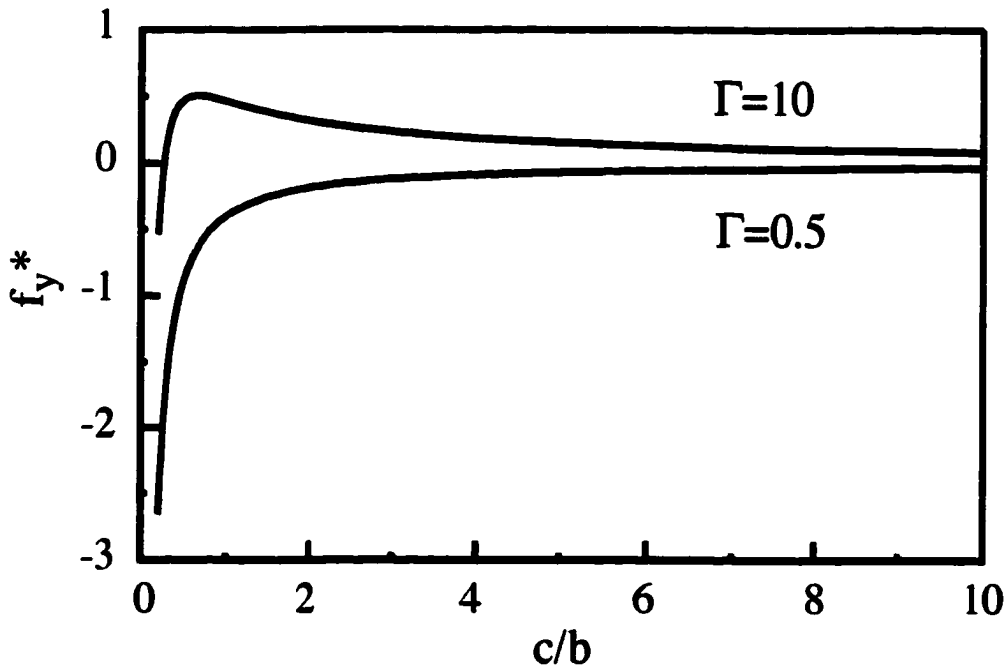


Figure 2.2. The normalized climb force $\mathbf{f}_y^*$ on a single dislocation versus the normalized dislocation/interface separation *c/b*.

Reproduced with permission of the copyright owner. Further reproduction prohibited without permission.

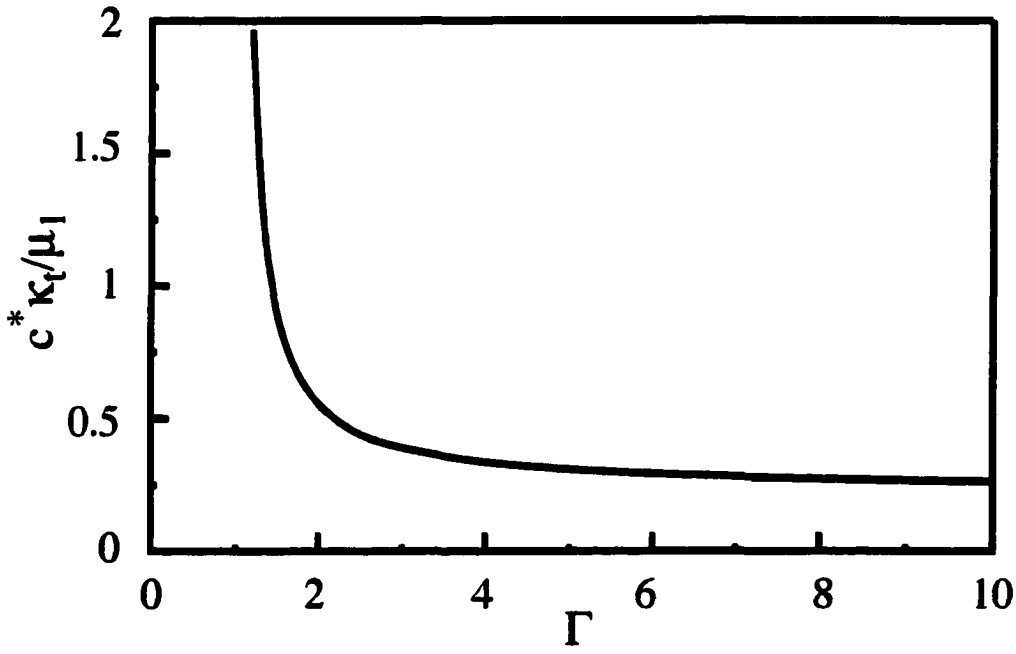


Figure 2.3. The dependence of the normalized equilibrium separation $c^*\kappa_t/\mu_1$ on the Dundurs parameter Γ.

Reproduced with permission of the copyright owner. Further reproduction prohibited without permission.

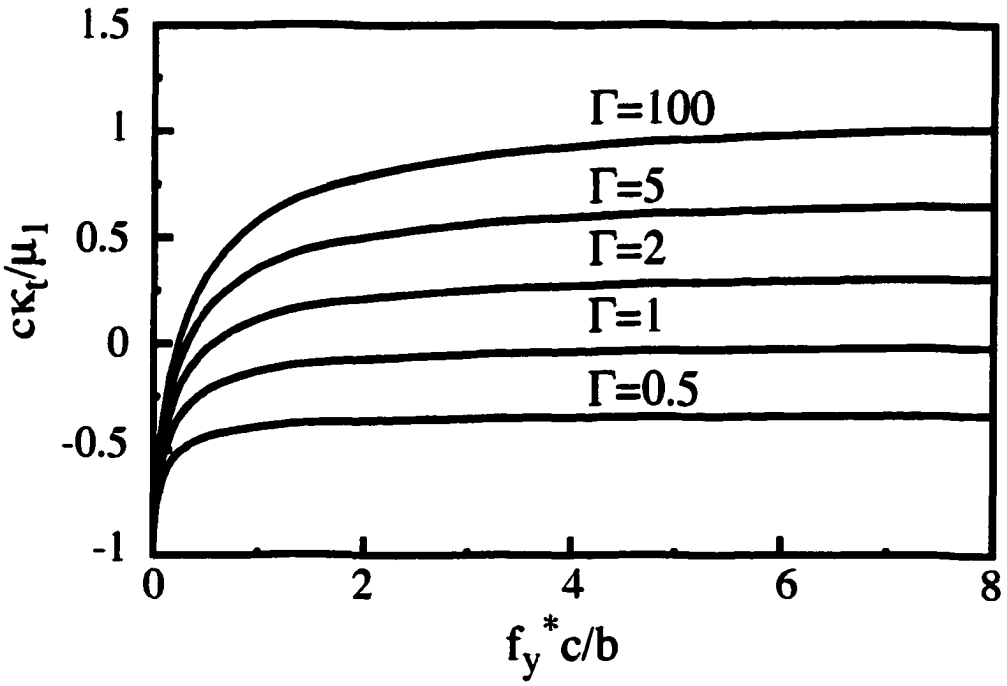


Figure 2.4. Normalized climb force $f_y^* c/b$ versus normalized separation $c\kappa_t/\mu_1$ for different values of the Dundurs parameter Γ.

Reproduced with permission of the copyright owner. Further reproduction prohibited without permission.

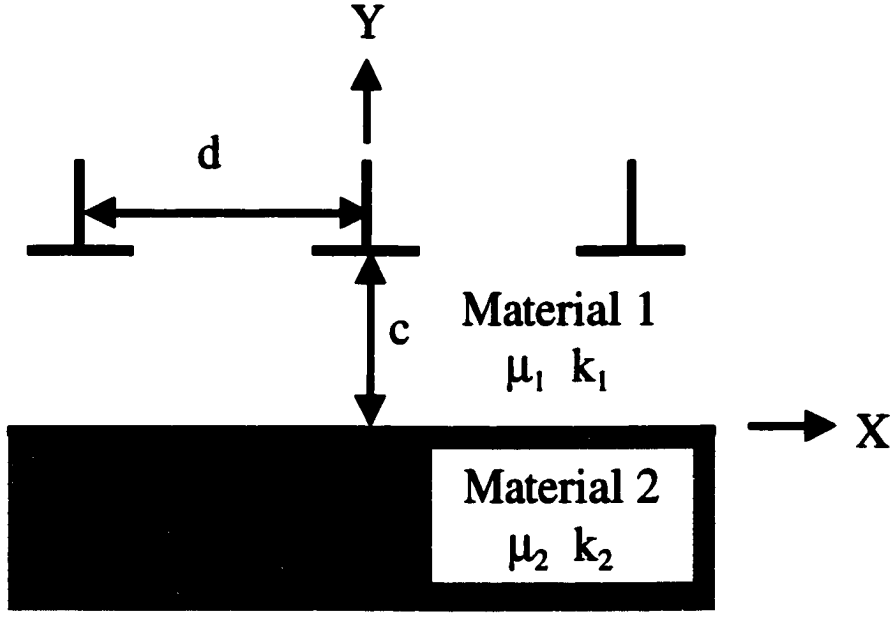


Figure 2.5. An illustration of the configuration employed in the analysis of the interaction between an array of misfit dislocations and a bimaterial interface.

Reproduced with permission of the copyright owner. Further reproduction prohibited without permission.

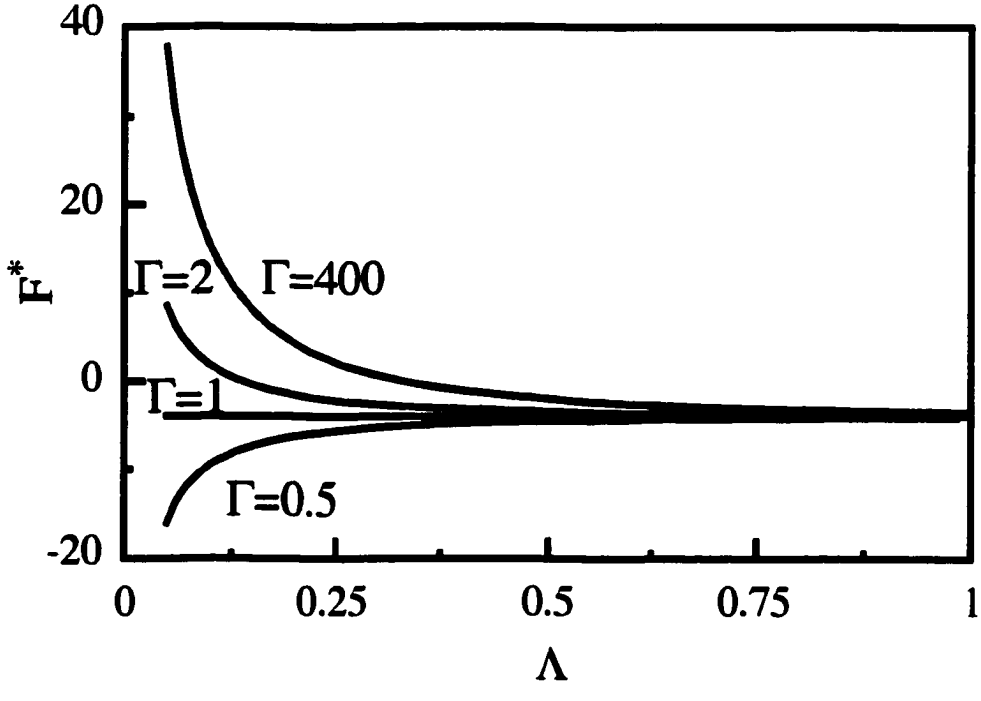


Figure 2.6. The normalized climb force F^* acting on dislocations in the array versus the normalized dislocation/interface separation $\Lambda = 2\pi c/d$ for the case of a "welded" interface ($\kappa_1 d/\mu_1 = \infty$). Different curves correspond to different values of the Dundurs parameter Γ.

Reproduced with permission of the copyright owner. Further reproduction prohibited without permission.

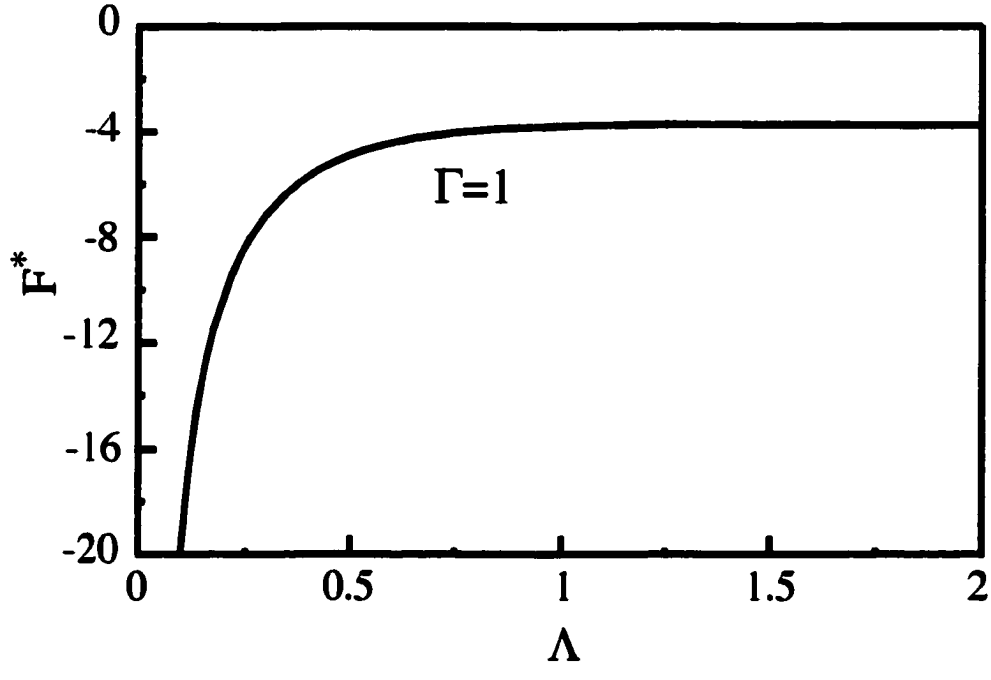


Figure 2.7. The normalized climb force F^* acting on dislocations in the array versus the normalized dislocation/interface separation Λ in the "slipping" interface limit ($\kappa_t d/\mu_1 \to 0$).

Reproduced with permission of the copyright owner. Further reproduction prohibited without permission.

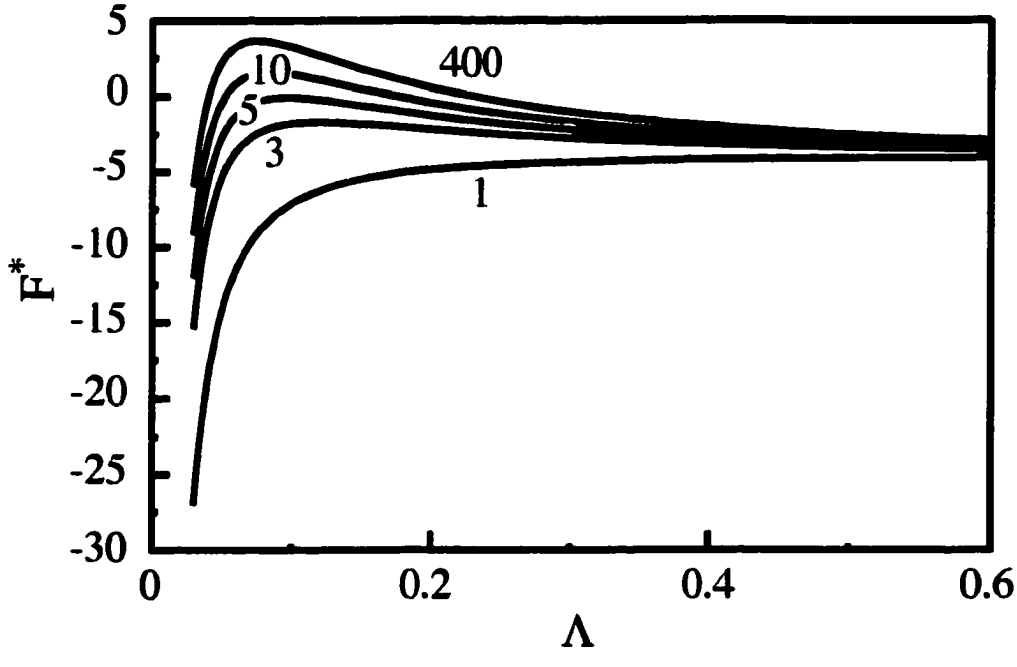


Figure 2.8. The normalized climb force F^* acting on dislocations in the array versus the normalized dislocation/interface separation Λ for a finite interfacial stiffness ($\kappa_i d/\mu_1 = 50$). The five curves correspond to the indicated values of the Dundurs parameter Γ.

Reproduced with permission of the copyright owner. Further reproduction prohibited without permission.

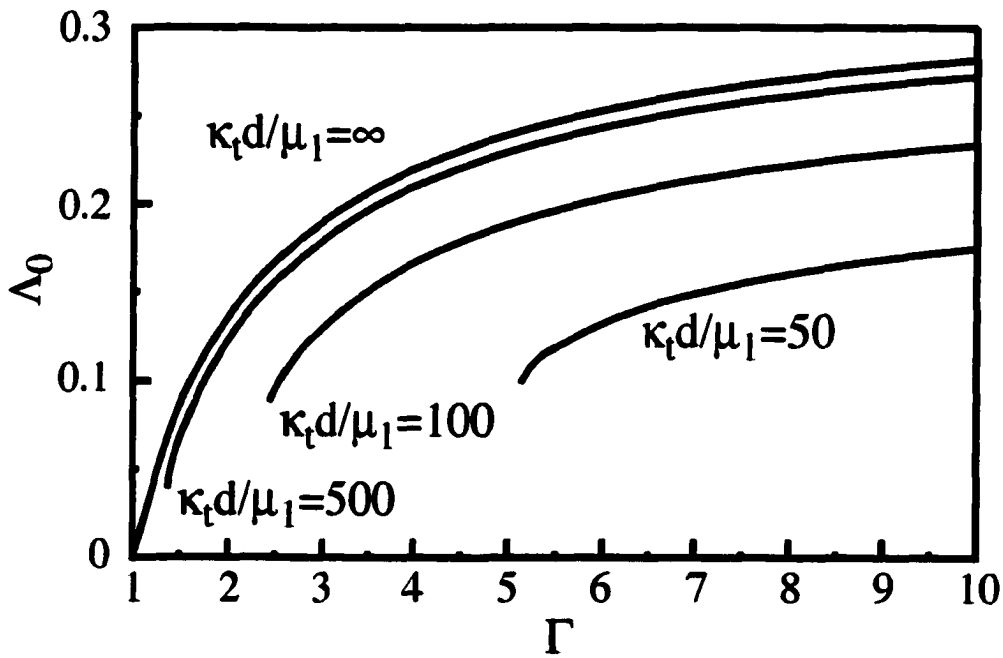


Figure 2.9. The dependence of the equilibrium stand-off distance Λ_0 on the Dundurs parameter Γ for different values of the interface stiffness ($\kappa_t d/\mu_1$).

Reproduced with permission of the copyright owner. Further reproduction prohibited without permission.

CHAPTER III

MORPHOLOGY EVOLUTION DURING MULTILAYER FILM GROWTH

3.1 Introduction

Multilayer semiconductor films are in widespread use in a number of modern optoelectronic applications. Magnetic multilayers possessing giant magnetoresistance are playing an increasing role in magnetic and magneto--optic storage technologies. Introduction of artificial periodicities, by repeating a pattern of layers of different materials, modifies the underlying electronic band structure and electron transport properties of the underlying materials, thereby providing an approach to fine tune materials properties.

Ideally, multilayer structures consist of periodic arrays of uniform, distinct coherent layers separated by sharp, atomically flat coherent interfaces. Recent progress has been made in incorporating misfitting materials into the superlattice. Strain-balanced superlattices made it possible to grow multilayer structures of thickness far exceeding the critical thickness of a single layer without forming misfit dislocations at interfaces [1, 2].

Multilayer films may not achieve this desired structure even if the thickness of individual layers in the superlattice is below the critical thickness for misfit dislocation formation for a single layer in the short–period superlattice. Deviations from atomic flatness may result from non-uniformities in the growth process or morphological instabilities. While the structure may be stable against plastic relaxation (misfit dislocation formation), elastic instabilities may occur during the growth process [3-5].

Reproduced with permission of the copyright owner. Further reproduction prohibited without permission.

Composition modulations/variations both parallel and perpendicular to the interfaces have been reported [6-11]. If carefully controlled, these modulations may be exploited to form self-organizing quantum nanostructures [12-15] which are promising candidates for semiconductor lasers due to their δ function–like density of electronic states. In this chapter, we examine the evolution of interface morphology during the growth of periodic, multilayer films. As shown below, a rich variety of interface morphologies may be obtained, depending on the properties of the materials making up the individual layers and on the growth conditions.

Modulations in microstructure and composition during epitaxial growth is, by no means, a novel subject. The formation of compositional modulations during the growth of alloy films has attracted the attention of several theorists (see e.g [16]). Large misfit stresses may modify the phase diagram of a miscible system, leading to spinodal decomposition [17]. The spinodal decomposition also makes the film unstable with respect to the growth of surface perturbations [18]. Guyer and Voorhees [19] considered morphological and compositional stability originating from compositional stress in an alloy during the deposition process. Step-flow mechanisms can contribute to alloy film instability during epitaxial growth and may also lead to a modulated structure [20]. Misfit stresses in a thin film can also lead to undulations of the growth [21]. The coupling between modulations of morphology and composition was recently considered by Glas [22].

While spinodal decomposition may explain composition modulation in alloy films, observation of composition modulations in multilayer films where each individual layer was a compound [10, 11] suggest that other mechanisms for the development of composition modulations also exist. In this chapter, we present a simple model for the formation of modulated multilayer structures which does not rely on alloy decomposition processes. Such modulations are through-thickness average modulations in composition and do not change the composition of the individual layers (as discussed below). We

Reproduced with permission of the copyright owner. Further reproduction prohibited without permission.

show that the competition between surface and elastic energy effects can lead to periodic interface modulations. Under certain conditions, these interface modulations can produce an overall lateral composition modulation in the growing multilayer film, as discussed below. Our analysis predicts the materials properties and growth conditions required to produce such modulations and both the wavelength and rate of growth of these modulations. We also predict the materials properties and growth conditions necessary to grow multilayer films which are stable against interface modulations. The existence of conditions for which stable films with flat interfaces is surprising since misfitting monolithic films are always unstable against surface modulations.

3.2 Problem formulation

The existence of interface undulations in multilayer films is closely related to the well-known elastic instability of free surfaces of stressed solids [3]. Consider a thin film grown heteroepitaxially on a substrate, such that a misfit stress exists. If the surface is not flat, the stresses within the film are non-uniform. The non-uniform elastic energy along the surface causes a variation in chemical potential along the surface that can be relaxed by mass flow along the surface (i.e., surface diffusion). In the case of a sinusoidal perturbation [5], these fluxes will result in the increase of the perturbation amplitude for any perturbation wavelength. The existence of non-negative surface energy impedes the growth of these perturbations. The interplay between these two factors, determines whether the perturbation amplitude will grow and, if so, the rate of growth. Short wavelength perturbations decay, whereas long wave modes grow exponentially with time.

If the surface of the film undulates, the atomic planes in the film are distorted by the non-uniform stress at the surface of the film. This situation is presented in Fig. 3.1. The average misfit stress in the film is denoted as σ and, for the sake of this argument,

Reproduced with permission of the copyright owner. Further reproduction prohibited without permission.

the lattice parameter of the film is originally smaller than that of the substrate (i.e. the misfit is negative and the film is in tension) and σ is positive. An elastic solution [5] shows that this film is more stretched in the troughs and more compressed at the crests of the free surface (Fig. 3.1). Consider now a situation in which a second film is deposited on the first with a lattice parameter which is greater than that of the first film. In this case, the atoms of the second film will have lower energy if they sit in the troughs compared with sitting on the crests. As more material is added to the second film, the amplitude of the surface perturbation gets smaller and will eventually reverse such that the second film will have troughs above the crests in the first layer and vice versa. As additional layers grow, this perturbation may propagate through the entire stack of layers, either increasing or decreasing in amplitude and with the perturbations on adjacent layers either in or out-of-phase.

We now formulate the problem in terms of continuum elasticity. Consider the multilayer film geometry presented in Fig. 3.2, which consists of alternating layers of two materials (material A and B) epitaxially deposited on a substrate (material C). The interfaces between adjoining layers are assumed to be coherent. If the layers are misfitting with respect to the substrate, they may develop a sinusoidal perturbation on the growing free surface, as discussed above. This surface perturbation will become a buried interface as more layers are deposited on top of it. This perturbed interface bounding misfitting materials will act as a source of stress and modify the stress field throughout the film and, especially, on the new growth surface. Each buried interface will affect the chemical potential on the surface and, therefore, will modify the surface diffusion and subsequently the surface profile.

We adopt the following notation for the remainder of this chapter. All quantities related to layer k will have a subscript k. Thus, the thickness of growing layer k is denoted as h_k and that of the fully grown layer as H_k. H_k is equal to H_A for odd-numbered layers and H_B for even-numbered ones. The misfit stress in layer k is denoted as Σ_k and is

Reproduced with permission of the copyright owner. Further reproduction prohibited without permission.

equal to σ_A for odd-numbered layers and σ_B for even-numbered ones. Similarly, the amplitude of the perturbation to the surface of layer k is denoted as Δ_k. The present analysis is performed in the two spatial dimensions containing the substrate and substrate normal.

The thickness of the growing film $\bar{h}$ at time t can be written as:

$$\bar{h}(t) = \sum_{j=1}^{k-1} H_j + h_k(t) \quad , \tag{1}$$

where layers up to k-1 are fully grown and have thickness H_j respectively, and layer k is currently growing (i.e., it has not yet grown to thickness H_k). The average layer thickness, h_k, is always measured from the average height of the previous layer, such that the film profile is described by

$$h(x,t) = \bar{h}(t) + \Delta_k(x,t) \quad , \tag{2}$$

where $\Delta_k(x,t)$ is the perturbation to the growing surface of layer k

In the simple model for film growth adopted in the present study, each layer is deposited with a uniform rate r_k (r_A or r_B for A and B layers, respectively). The material is allowed to diffuse only along the growing surface. Therefore, no morphology evolution occurs below the current growth surface, i.e. no bulk diffusion. Mathematically, we write the evolution equation for the growing surface as [23]:

$$\frac{\partial h}{\partial t} = r_k + \frac{D_k \Omega_k \theta_k}{k_B T} \frac{\partial^2 \mu_k^s}{\partial s^2} \quad , \tag{3}$$

where D_k is the surface diffusivity of the material of layer k, k_B is the Boltzmann constant, and Ω_k and θ_k are the atomic volume and surface density, respectively. The chemical potential of the atoms at the surface of the growing layer μ_k^s and its second derivative are evaluated along the surface. This expression explicitly assumes that the

Reproduced with permission of the copyright owner. Further reproduction prohibited without permission.

deposition rate on each point of the surface is constant and unaffected by variations in the surface chemical potential.

The linear stability of the multilayer morphology is analyzed by considering a sinusoidal perturbation to the profile of an otherwise flat interface. We Fourier transform the coordinate parallel to the substrate, i.e.

$$\Delta_k(\xi) = \int_{-\infty}^{\infty} dx \Delta_k(x) e^{-i\xi x} \quad , \tag{4}$$

where ξ is the wave vector. Since this is done throughout, we will write $\Delta_k(\xi)$ simply as Δ_k. The present analysis is performed only to first order in perturbation theory, where the small parameter is the product of the wave vector ξ and the amplitude of the shape perturbation of a layer Δ. Within this approximation, the derivative along the surface in Eq. (3) is replaced by the derivative with respect to the x-coordinate. Equation (3) may, therefore, be rewritten as:

$$\frac{\partial \Delta_k}{\partial t} = -\xi^2 \frac{D_k \Omega_k \theta_k}{k_B T} \mu_k^s(\xi) \ . \tag{5}$$

Following [23], we write the chemical potential at the surface (in the x-space) as:

$$\mu(x) = \mu_0 + \gamma_k \Omega_k \kappa(x) + \frac{\Omega_m}{2} \boldsymbol{\sigma}_k^s(x) \mathbf{S} \boldsymbol{\sigma}_k^s(x) \quad , \tag{6}$$

where μ_0 is the chemical potential of a flat surface bounding unstressed material and the other two terms in this expression are the surface energy and elastic contributions, respectively. $\kappa(x)$ is the curvature of the growing surface and γ_k is the surface energy of layer k. The stress tensor $\boldsymbol{\sigma}_k^s(x)$ is evaluated at the surface and $\mathbf{S}$ is the elastic compliances tensor of layer k. For the sake of simplicity, we also assume that the elastic constants of materials A and B are identical.

Reproduced with permission of the copyright owner. Further reproduction prohibited without permission.

To first order in perturbation theory, the surface energy term in Eq. (6) can be written as

$$\mu_\gamma(\xi) = \gamma_k \Omega_k \kappa(\xi) = \gamma_k \Omega_k \xi^2 \Delta_k \tag{7}$$

The leading order contribution to the elastic term in the chemical potential is associated with the coupling between the uniform misfit stress Σ and the non-uniform contribution to the surface stress tensor $\sigma_k^s(x)$. Since the surface is nearly flat, the only term that enters the elastic contribution to the chemical potential is the normal stress parallel to the surface $\sigma_{xx}^s(x)$:

$$\mu_{el}(x) = \Omega_k \frac{\Sigma_k \sigma_{xx}^s(x)}{M} \quad , \tag{8}$$

where M is the elastic modulus in the direction along the surface which, in the plane strain approximation is

$$M = \frac{E}{1-\nu^2} \quad , \tag{9}$$

where E and ν are the Young's modulus and Poisson ratio, respectively. In the following, we derive an equation for the stress at the growing surface and assemble all of the terms in the evolution equation (Eq. 5). Next, we non-dimensionalize this equation and analytically solve for the amplitude of the perturbation of the growing layer $\Delta_k(\xi)$ as a function of material parameters and growth conditions.

3.3. Elastic analysis

In this section, we determine the tangential component of the stress at the surface of the growing layer k in the multilayer structure. This stress is required to evaluate the elastic component of the chemical potential, as described above (see Eq. 8). We analyze

Reproduced with permission of the copyright owner. Further reproduction prohibited without permission.

this problem within the framework of two-dimensional, isotropic, plane strain elasticity, in which materials A and B have the same elastic constants.

A simple analysis shows that there are two contributions to the stress $\sigma^{s}_{xx}(x)$ in first order in perturbation theory.

$$\sigma^{s}_{xx}(x) = \sigma_{surf}(x) + \sigma_{int}(x) \quad . \tag{10}$$

The first term is associated with the surface itself and is present because the growing surface is not flat. This stress is the correction to the uniform misfit stress Σ_k (i.e., the *xx*-component) that arises from the requirement that the surface tractions must be zero, as described by Asaro [3], Grinfeld [4], Srolovitz [5] and others. The Fourier transform of $\sigma_{surf}(x)$ may be written as:

$$\sigma_{surf}(\xi) = -2|\xi|\Delta_k\Sigma_k \quad , \tag{11}$$

where $|\xi|$ is the absolute value of the wave vector ξ and Δ_k is in Fourier space.

The second contribution to the stress at the surface in Eq. (10) is associated with the presence of buried interfaces and is only present when those interfaces are not flat. Because materials A and B have identical elastic constants, each interface contributes separately to the term σ_{int}. We determine σ_{int} using the Eshelby procedure [24] for the stress created by a misfitting inclusion. Consider the non-flat interface between layers *n* and *n*+1, the shape of which is determined by the amplitude of the n^{th} perturbation $\Delta_k(x)$ or, in Fourier space, $\Delta_n(\xi)$. If we make an imaginary cut along this interface, the macroscopic misfit stresses Σ_n and Σ_{n+1}, create surface tractions along both sides of the cut. To balance these tractions, we apply equal and opposite corrective tractions along the surfaces of the cut and then "weld" the two pieces back together. The stress produced by these corrective tractions, evaluated at the free surface, is σ_{int} for the *n* / *n*+1 interface.

Reproduced with permission of the copyright owner. Further reproduction prohibited without permission.

The tractions along the interface cut are, to first order in the small parameter $\Delta_n\xi_n$, the sum of the products of the misfit stresses Σ_n and Σ_{n+1} and the outer normals to the interface. In Fourier space, this traction **T** is:

$$\mathbf{T}_x = -i\Delta_n\xi(\Sigma_n - \Sigma_{n+1}) \quad \text{and} \quad \mathbf{T}_y = 0 \tag{12}$$

i.e. only the tangential component of the tractions is present. We also make use of the fact that $\Delta_m\xi_m$ is small to replace the actual curved interface with a flat interface while keeping the corrective tractions along that interface ($\mathbf{T}_c$ = -**T**) associated with the original curved interface. This line traction is parallel to and some distance from the free (growing) surface in an elastic half-plane. The expression for the stress field produced by such a line traction is derived in Appendix 3A, based on the Green's function for an elastic half-plane:

$$\sigma_{int}^{n/n+1} = -\Delta_n|\xi|(\Sigma_n - \Sigma_{n+1})\left[2 - \frac{|\xi|h_{nk}}{1-\nu}\right]exp(-|\xi|h_{nk}) \quad . \tag{13}$$

In order to determine the stress on the surface from all interfaces, this expression must be summed over n. The distance h_{nk} in this equation is the distance from the interface under consideration to the growing surface:

$$h_{nk} = \sum_{j=n+1}^{k-1} H_j + h_k \quad . \tag{14}$$

Note that this stress is time-dependent, since the thickness of the growing layer h_k increases linearly for a fixed growth rate r_k:

$$h_k = r_k t \tag{15}$$

Equations (5), (6), (8) and (10) provide the necessary framework to write down the equation governing the amplitude of the perturbation to the growing layer k. Combining Eqs. (5), (7), (11), (13) and (15) yields:

Reproduced with permission of the copyright owner. Further reproduction prohibited without permission.

$$\frac{\partial \Delta_k}{\partial h_k} = \frac{D_k \Omega_k{}^2 \theta_k}{r_k k_B T} |\xi|^3 \left[-\gamma_k |\xi| \Delta_k + 2\frac{\Sigma_k{}^2}{M}\Delta_k - \frac{\Sigma_k}{M}\left(\sum_{j=1}^{k-1} \Delta_j (\Sigma_{j+1} - \Sigma_j) \left[2 - \frac{|\xi| h_{jk}}{1-\nu} \right] e^{|\xi| h_{jk}} \right) \right], \quad (16)$$

where we have replace the variable time with the thickness of the growing layer h_k, using Eq. (15). The amplitude of the perturbation to the surface of each layer is a function of the amplitude of the perturbations to the interfaces of all underlying layers.

If we remove the terms in Eq. (16) associated with the buried interfaces, we find that it is identical to that derived by Asaro and Tiller [3] and Srolovitz [5] in the context of the analysis of the stability of a free surface bounding a stressed body. They found that there exists a wave vector for which a sinusoidal shape perturbation grows the fastest. We denote this wave vector for material A as ξ_A and use it as a length scale throughout the remainder of this analysis.

$$\xi_A = \frac{3\Sigma_A{}^2}{2M\gamma_A} . \quad (17)$$

We introduce the ratio of the misfit stress in material B (even-numbered layers) to that in material A (odd-numbered layers) $\beta = \Sigma_B/\Sigma_A$ and the ratio of surface energies $\Gamma = \gamma_B/\gamma_A$. The difference between the misfit stresses in the adjacent layers n and $n + 1$ is:

$$\Sigma_{n+1} - \Sigma_n = (-1)^n \Sigma_A (1-\beta) . \quad (18)$$

We consider the evolution of odd-numbered layers separately from the even-numbered layers. Eq. (16) becomes

$$\frac{\partial \Delta_k}{\partial h_k^*} = \Phi_A \xi^{*3} \left[\left(2 - \frac{3}{2}\xi^* \right)\Delta_k - \sum_{j=1}^{k-1} (-1)^j \Delta_j (1-\beta) \left[2 - \frac{\xi^* h_{jk}^*}{1-\nu} \right] e^{-\xi^* h_{jk}^*} \right] \quad (19a)$$

Reproduced with permission of the copyright owner. Further reproduction prohibited without permission.

for odd-numbered layers and

$$\frac{\partial \Delta_k}{\partial h_k^*} = \Phi_B \xi^{*3} \left[\left(2\beta^2 - \frac{3}{2}\Gamma\xi^* \right) \Delta_k - \sum_{j=1}^{k-1} (-1)^j \Delta_j \beta(1-\beta) \left[2 - \frac{\xi^* h_{jk}^*}{1-\nu} \right] e^{-\xi^* h_{jk}^*} \right] . \qquad (19b)$$

for even-numbered layers. Here, the dimensionless wave vector ξ^* is measured in terms of ξ_A:, $\xi^* = |\xi|/\xi_A$, and Φ_A and Φ_B are:

$$\Phi_A = \frac{D_A \Omega_A^2 \theta_A \Sigma_A^2 \xi_A^2}{r_A k_B T M} \quad \text{and} \quad \Phi_B = \frac{D_B \Omega_B^2 \theta_B \Sigma_A^2 \xi_A^2}{r_B k_B T M} , \qquad (20)$$

respectively. The thicknesses of each layer are also made dimensionless, as follows:

$$H_k \xi_A \rightarrow H_k^* , \quad H_A \xi_A \rightarrow H_A^* , \quad H_B \xi_A \rightarrow H_B^* , \quad h_{jk} \xi_A \rightarrow h_{jk}^* \text{ and } h_k \xi_A \rightarrow h_k^* \qquad (21)$$

3.4. Solution of the evolution equation

In order to determine the temporal evolution of the amplitude of the perturbation on the surface of the growing film, we must integrate the evolution equation (Eq. 19.a,b) over the entire layer thickness (i.e., from $h_k = 0$ to $h_k = H_k$) starting from the initial condition $\Delta_k(0) = \Delta_{k-1}(H_{k-1})$.

Equations (19a), (19b) can be simplified by the introduction of new variables:

$$X_j = \Delta_j \exp\left(\xi^* \sum_{n=2}^{j} H_n^* \right) . \qquad (22)$$

The evolution equation now becomes

Reproduced with permission of the copyright owner. Further reproduction prohibited without permission.

$$\frac{\partial X_k}{\partial h_k^*} = \Phi_A \xi^{*3}\left[\left(2-\frac{3}{2}\xi^*\right)X_k - e^{\xi^* H_A^*}\sum_{j=1}^{k-1}(-1)^j X_j(1-\beta)\left[2-\frac{\xi^* h_{jk}^*}{1-\nu}\right]e^{-\xi^* h_k^*}\right] \tag{23a}$$

for odd-numbered layers and

$$\frac{\partial X_k}{\partial h_k^*} = \Phi_B \xi^{*3}\left[\left(2\beta^2-\frac{3}{2}\Gamma\xi^*\right)X_k - e^{\xi^* H_B^*}\sum_{j=1}^{k-1}X_j(-1)^j\beta(1-\beta)\left[2-\frac{\xi^* h_{jk}^*}{1-\nu}\right]e^{-\xi^* h_k^*}\right] \tag{23b}$$

for even-numbered layers with the initial condition modified accordingly.

Integration of Eq. (23.a,b) yields the following linear relations

$$X_k = X_{k-1}F_A - \sum_{n=1}^{k-1}(-1)^n X_n(1-\beta)\left[\Xi_A + \Psi_A\left(\sum_{j=n+1}^{k-1}H_j^*\right)\right] \tag{24a}$$

for odd-numbered layers and

$$X_k = X_{k-1}F_B - \sum_{n=1}^{k-1}(-1)^n X_n\beta(1-\beta)\left[\Xi_B + \Psi_B\left(\sum_{j=n+1}^{k-1}H_j^*\right)\right] \tag{24b}$$

for even-numbered layers, where we have introduced the following composite parameters:

$$\begin{aligned}
&F_A = \exp\left(\Phi_A\delta_A\xi^{*3}H_A^*\right), \quad F_B = \exp\left(\Phi_B\delta_B\xi^{*3}H_B^*\right),\\
&\Psi_A = -\frac{(F_A-1)\xi^*}{(1-\nu)\delta_A}, \quad \Psi_B = -\frac{(F_B-1)\xi^*}{(1-\nu)\delta_B}\\
&\Xi_A = \left(2-\frac{1}{(1-\nu)\Phi_A\xi^{*2}\delta_A}\right)\frac{F_A-1}{\delta_A} + \frac{\xi^*H_A^*}{\delta_A(1-\nu)},\\
&\Xi_B = \left(2-\frac{1}{(1-\nu)\Phi_B\xi^{*2}\delta_B}\right)\frac{F_B-1}{\delta_B} + \frac{\xi^*H_B^*}{\delta_B(1-\nu)}
\end{aligned} \tag{25}$$

Reproduced with permission of the copyright owner. Further reproduction prohibited without permission.

$$\delta_A = \frac{1}{\Phi_A \xi^{*2}} + \left(2 - \frac{3}{2}\xi^*\right), \qquad \delta_B = \frac{1}{\Phi_B \xi^{*2}} + \left(2\beta^2 - \frac{3}{2}\Gamma\xi^*\right).$$

In order to improve the clarity of the results, we limit consideration of the solutions to the special case (to be relaxed later) where materials A and B are identical in every respect, except that the magnitude of the misfit stress Σ with respect to the substrate is equal and opposite in the two materials (i.e., $\beta = -1$). To be specific both materials have the same values of D, θ, Ω and γ, and are grown with the same deposition rate r and to the same thickness H. Since the two materials have the same thickness and equal and opposite misfit, there will be no driving force to form misfit dislocations provided that each layer can be grown to a thickness H on the pristine substrate without dislocation formation. Equations (24a), (24b) can be now be rewritten without subscripts and with $\beta = -1$ and $\Gamma = 1$:

$$X_k = X_{k-1}F - 2\sum_{j=1}^{k-1}(-1)^{k-j-1}X_j\left[\Psi H^*(k-j-1) + \Xi\right] \tag{24'}$$

The variables can now be rewritten as $\xi_0 = 3\Sigma^2/(2M\gamma)$, $\xi^* = |\xi|/\xi_0$, $H\xi_0 \rightarrow H^*$

$$\Phi = \frac{D\Omega^2\theta\Sigma^2{\xi_0}^2}{rk_BTM} \tag{20'}$$

and

$$F = \exp\left(\Phi\xi^{*3}\delta H^*\right), \quad \Psi = -\frac{\xi^*(F-1)}{(1-\nu)\delta},$$

$$\Xi = \left(2 - \frac{1}{(1-\nu)\Phi\xi^{*2}\delta}\right)\frac{F-1}{\delta} + \frac{\xi^* H^*}{\delta(1-\nu)}, \quad \delta = \frac{1}{\Phi\xi^{*2}} + \left(2 - \frac{3}{2}\xi^*\right), \tag{25'}$$

and Eq. (22) becomes

Reproduced with permission of the copyright owner. Further reproduction prohibited without permission.

$$X_j = \Delta_j e^{\xi^* H^* (j-1)} \quad . \tag{22'}$$

While the integrated equation for the evolution of the surface of the topmost layer (c.f. Eq. 24') is a function of the amplitude of the perturbations to all buried interfaces, it can be reduced to a much simpler linear recurrence relation that only involves the amplitude of the perturbations on three previous, consecutive interfaces, as shown in detail in Appendix 3B. Since the recurrence relation is linear and only depends on the amplitudes of the perturbations to three consecutive interfaces, the solution ($k \geq 4$) can be written in the following form

$$\Delta_k^+ = \alpha_1 \lambda_1^{k-1} + \alpha_2 \lambda_2^{k-1} + \alpha_3 \lambda_3^{k-1} \tag{26}$$

where we normalize the amplitude of the interface perturbation for each layer Δ_k by that of the first layer Δ_1 (i.e., $\Delta_l^+ = \Delta_l / \Delta_1$). λ_1, λ_2 and λ_3 are the eigenvalues of the matrix $\mathbf{L}$ (Eq. 3B.5)

$$\mathbf{L} = \begin{pmatrix} e^{-\xi^* H^*}(F - 2 - 2\Xi) & 1 & 0 \\ e^{-2\xi^* H^*}\left(2F - 1 + 2\Psi H^* - 2\Xi\right) & 0 & 1 \\ e^{-3\xi^* H^*} F & 0 & 0 \end{pmatrix} \tag{27}$$

and the coefficients α_1, α_2 and α_3 are the coefficient of the expansion of the vector $\mathbf{Y}_1$ in the basis of the eigenvectors of the matrix $\mathbf{L}$ (see Appendix 3B). The two elements of the vector $\mathbf{Y}_1$, which are the amplitudes of the perturbation of the interface above layers 2 and 3, $\mathbf{Y}_1 = \langle \Delta_3^+, \ \Delta_2^+, \ 1 \rangle$ need to be computed directly using Eqs. (24'), (22').

Because the perturbation amplitude grows as the eigenvalues of $\mathbf{L}$ to a power equal to the number of layers minus one (see Eq. 26), in the limit of a large number of layers, the amplitude of the perturbation on layer k is dominated by the largest eigenvalue:

Reproduced with permission of the copyright owner. Further reproduction prohibited without permission.

$$\Delta_k^+ = \alpha\lambda_1^{k-1} \quad , \tag{28}$$

where λ_1 is the largest eigenvalue of **L** and α_1 is the corresponding expansion coefficient. In the case when the maximal eigenvalues form a complex conjugate pair, the previous equation should includes the complex conjugate term as well sign (Δ_k^+ is a real number)

$$\Delta_k^+ = \alpha_1\lambda_1^{k-1} + \bar{\alpha}_1\bar{\lambda}_1^{k-1} \quad . \tag{28a}$$

Here, the bar over the variable indicates complex conjugate.

This asymptotic regime is reached fairly quickly because the difference between the asymptotic equation (c.f. Eq. 28) and the full equation (Eq. 26) decays as a power of the ratio of the eigenvalues. Thus, in studying the stability of the multilayer film, we use Eqs. (28), (28a) instead of the full equation (Eq. 26) and the perturbation behavior is fully determined by the dependence of Λ on the parameters ξ^* (normalized wave vector), H^* (normalized thickness of an individual layer) and Φ (Eq. 20'). The physical interpretation of Φ is discussed below.

Given a set of parameters H^* and Φ, as well as the magnitude of the wave vector ξ^*, the morphology of the multilayer structure can be classified according to the value of λ_1. If the absolute value of λ_1 is smaller than one, the perturbation does not propagate through the multilayer film but, rather, decays after a few layers – i.e., the interfaces are flat and we refer to this structure as stable. In the opposite case, when the absolute value of λ_1 is greater than one, the amplitude of the perturbation to the interfaces grows with the layer number – we refer to this structure as unstable. We can examine the nature of this instability by considering λ_1 in more detail.

The morphology of the structure in the unstable regime is determined by the complex phase of λ_1. If λ_1 is real and positive, the perturbation amplitudes (Δ) grows from interface to interface and the perturbations on consecutive interfaces will be in-phase, as indicated schematically in Fig. 3.3a. If λ_1 is real and negative, the value of Δ grows from interface to interface and perturbations on consecutive interfaces are out-of

Reproduced with permission of the copyright owner. Further reproduction prohibited without permission.

phase – i.e., the amplitude of the perturbations changing sign at each interface (the layer is accordion-shaped) as shown in Fig. 3.3b. The resulting structure is modulated not only morphologically, but also compositionally, since a vertical cross section of a multilayer film in the plane perpendicular to the plane of Fig. 3.3b will show oscillations in the fraction of materials A and B. When λ_1 is complex, the perturbations at consecutive interfaces are out-of-phase as well, but the sign change is not regular and will be determined by the complex phase of λ_1.

We reiterate that the asymptotic equation (Eq. 28) is valid provided that the expansion coefficient α_1, corresponding to the maximal eigenvalue λ_1, is not zero, and its value is not negligible compared to the expansion coefficients (α_2 and α_3) corresponding to other two eigenvalues (λ_2 and λ_3). In the quantitative analysis of the results presented in the next section, we checked to insure that this condition is satisfied. We present our results in terms of the stability diagram which provides a link between the materials and growth parameters and the morphology of the interfaces.

3.5. Stability diagrams

In this section, we examine the dependence of Δ on the material and growth parameters captured in Φ and H^* for the special case where adjacent layers are the same except for the misfit with respect to the substrate (i.e., the misfits are equal but have opposite sign). For each point in the Φ - H^* plane, we determine the dependence of the maximal eigenvalue λ_1 on the normalized eigenvector ξ^*. The rate at which the perturbations grow depends on the imposed perturbation wavelength. The fastest growing perturbation corresponds to $\lambda_1 = \lambda_{max}$, which occurs at $\xi^* = \xi^*_{max}$. The nature of the evolution of the perturbation amplitude with layer number is determined by whether the magnitude of λ_{max} is greater or less than unity and whether it is real or complex, as discussed above. The resultant stability diagram is presented in Fig. 3.4. Four distinct

Reproduced with permission of the copyright owner. Further reproduction prohibited without permission.

fields are found on the stability diagram. The region corresponding to $|\lambda_{max}| < 1$, marked stable in Fig. 3.5, indicates that the amplitude of the perturbations to the interfaces decrease with increasing number of layers for all wavelengths. In the region of unstable growth ($|\lambda_{max}| > 1$), the mode of the instability is determined by the phase of λ_{max}, as discussed in the previous section. For thick layers (large H^*) and slow diffusion (low Φ), the instability corresponds to in-phase growth; resulting in snake-like layers, as shown in Fig. 3.3a. As Φ increases and/or the layers are thin, the interface perturbations grow out-of-phase; resulting in accordion-like layers, as shown schematically in Fig. 3.3b. Between the unstable/out-of-phase and stable fields, a region of complex λ_{max} exists. In this region of the diagram, consecutive interfaces are either in- or out-of-phase depending on the interface number. This pattern of in- and out-of-phase interfaces may be either periodic or aperiodic as determined by the complex phase of λ_{max}.

A contour plot of the logarithm of the absolute value of λ_{max} is shown in Fig. 3.5. The contour lines are drawn only in the region where the film growth is unstable, i.e. $|\lambda_{max}| > 1$. The magnitude of λ_{max} and, consequently, the rate of growth of the instability increases with increasing distance from the stable growth domain within the Φ - H^* plane. In order to put the rate of growth of the instability into perspective, we compare how much the amplitude of the instability changes during the growth of a single layer with that for growing either pure A or pure B on the substrate to the thickness of one layer. The latter can be found by integrating Eq. (16) omitting the contributions associated with the buried interfaces. The corresponding value which we define as λ_s is simply: $\lambda_s = \exp(\Phi H^*/2)$. Contours of constant $\ln(\lambda_s)$ form straight lines in the Φ - H^* stability map of Fig. 3.5. The contours of constant $\ln(\lambda_{max})$ asymptotically approach the straight single layer lines ($\ln(\lambda_s)$) at large film thickness H^*. This is to be expected since the stress on the surface due to a buried interface decreases exponentially with the distance between the surface and buried layer (see Eq. 13).

Reproduced with permission of the copyright owner. Further reproduction prohibited without permission.

The magnitude of the wave vector of the most unstable perturbation ξ^*_{max} (corresponding to the eigenvalue λ_{max}) determines the overall film morphology. For a pure material (i.e., single layer film), the wave vector of the most unstable instability wave is equal to ξ_0 (i.e., $\xi^* = 1$). The contour plot of ξ^*_{max} for the domains of unstable multilayer growth is shown in Fig. 3.6. The magnitude of ξ^*_{max} does not significantly vary from one except for very small film thicknesses H^*. This implies that in most situations, the wavelength of the interface modulations will be very similar to that for a pure, single layer film and will not evolve significantly as the multilayer film grows.

The overall stability diagram (Fig. 3.4) is a result of the interplay between the three terms in Eq. (16): the surface energy that always favors the smoothing of the surface, the elastic energy relaxation associated with a curved surface which always favors the growth of surface perturbations, and the contribution from the stress associated with buried interfaces which may either favor the growth or decay of perturbations. Consider the relatively simple case of the growth of a single layer of material B on the first A layer. When the second layer is very thin, the stress on the surface from the buried A/B interface favors faster B growth in the troughs and slower B growth near the peaks of the surface profile. This, combined with the surface energy term, opposes the elastic energy relaxation term and leads to a decrease in the amplitude of the perturbation of the surface of the second layer. If the buried layer stress effect dominates the surface energy and the atomic mobility is sufficiently high (or the growth rate is sufficiently slow), the second layer will grow from one with perturbations to a nearly flat surface and then, with continued growth, to one for which perturbations of the opposite sign grows. Once perturbations of the opposite sign begin to grow, the elastic energy relaxation term further accelerates their growth. This corresponds to unstable, out-of-phase growth.

If the second (B) layer continues to grow, it may reach the thickness at which the sign of the stress on the surface from the buried interface switches sign (see Eq. 13). In this case, the stress from the buried interface favors faster B growth near the peaks on the

Reproduced with permission of the copyright owner. Further reproduction prohibited without permission.

surface and slower growth near the troughs. This leads to an increase in the amplitude of the perturbation and the layer growth is unstable and in-phase – hence the presence of an unstable, in-phase region in the Φ - H^* stability map. The existence of a growing, in-phase surface perturbation will only occur if the atomic mobility (Φ) is sufficiently low that the sign of the surface perturbation does not switch prior to the film thickness achieving the value at which the sign of the stress from the buried interface changes sign. This dependence of the growth mode on the atomic mobility explains the switch from in-phase to out-of-phase growth at large H^* in the Φ - H^* stability map of Fig. 3.4.

The presence of a region in the stability diagram where the perturbations decay can be understood as a type of out-of-phase growth that did not have sufficient time to be expressed. As discussed above, when the second layer is thin, the stress from the buried layer reinforces the tendency from the surface energy to grow faster in the troughs and slower at the peaks in the surface profile. If given sufficient time, this effect would lead to out-of-phase growth. However, if the growth of the second layer is terminated and the growth of a third layer begun before the sign of the perturbation switches, the interface is left with a perturbation that is of the same sign, but *smaller amplitude* then that of the first interface. This decrease in amplitude of the perturbation upon growth of an additional layer is the source of the stable region in the multilayer film stability diagram (Fig. 3.4).

In addition to the in-phase and out-of-phase modes in the unstable regions of the Φ - H^* stability map, there is a an unstable domain where the perturbations increase in absolute value but with a sign that is neither always the same nor alternates from layer-to-layer (i.e., labeled "complex" in Fig. 3.4). This region is between the stable and out-of-phase unstable domains. The origin of this effect cannot be explained on the basis of the two layer picture used to describe the origin of the other regions of the diagram and is strictly a result of the combined effects of many buried interfaces.

Reproduced with permission of the copyright owner. Further reproduction prohibited without permission.

In presenting the stability map (Fig. 3.4), we tacitly assumed that the wave length of modulations corresponds to the most unstable wave vector (i.e., that with $\xi^* = \xi^*_{max}$) and that this perturbation wave vector is constant during the entire growth. However, analysis of the growth of a single layer film (either pure A or pure B) showed that perturbations to the surface profile only grow, when the wave vector of those perturbations are smaller than a critical value, $\xi < 4/3\ \xi_0$ [5]. Therefore, there may not be any perturbations available to grow if $\xi^*_{max} > 4/3$. If this is indeed the case, then the stable region of the Φ - H^* stability map will be larger. In order to account for this effect, we reconstruct the stability diagram allowing only wave vectors of magnitude $\xi^*_{max} \leq 4/3$. The resultant stability map is presented in Fig. 3.7. This wave vector cut-off greatly expands the stable region of the diagram such that the entire small Φ / small H^* quadrant is stable. In addition to expanding the stable region of the map, cutting off ξ^*_{max} greatly expands the unstable region corresponding to the complex eigenvalues.

An additional caveat associated with the present analysis should be kept in mind. Stability or instability in the maps of Figs. 4 and 7 is determined based on how the system will behave in the limit of a large number of layers. The number of layers that must be grown until this analysis is valid is determined by the magnitude of the eigenvalue λ_1 in Eq. (28). Fortunately, the instability develops very quickly over the entire unstable region of Figs. 3.4 and 3.7, with the exception of the region near the stable-complex unstable boundary of Fig. 3.7. Hence, the stability map presented above properly expresses the actual situation under nearly all conditions.

3.6. General case

The asymptotic expression for the amplitude of the instability in the general case is derived in Appendix 3B:

$$\Delta^+_k = \alpha_1 \Lambda_{11} \lambda_1^{(k-4)/2} \quad \text{and} \quad \Delta^+_{k-1} = \alpha_1 \Lambda_{12} \lambda_1^{(k-4)/2} \tag{29}$$

Reproduced with permission of the copyright owner. Further reproduction prohibited without permission.

for even k, where λ_1 is the maximal eigenvalue and the coefficient α_1 is assumed not negligible compared to other three expansion coefficients. The matrix $\mathbf{\Lambda}$ is composed of the eigenvectors of matrix L as defined in Appendix 3B (see following Eq. 3B.10). The amplitude of the perturbation to the surface on one layer is determined by multiplying the amplitude of the perturbation on the previous layer by $\Lambda_{11}/\Lambda_{12}$ or $\lambda_1\Lambda_{12}/\Lambda_{11}$ depending on whether the top layer is even or odd. All stability arguments used above to describe the nearly equivalent material case can also be applied to the general case. To be more specific, the eigenvalue λ in the general case corresponds to the square of the same eigenvalue in the nearly equivalent material case and the instability condition $|\lambda| > 1$ applies in the general case as well. The phase of the variation in perturbation amplitude cannot be easily analyzed in the general case because it is determined by both $\Lambda_{11}/\Lambda_{12}$ and $\lambda_1\Lambda_{12}/\Lambda_{11}$ depending on whether the top layer is even or odd. In the nearly equivalent material case, these two numbers are both equal to the maximal eigenvalue.

Although the dependence of the mode of the perturbation (in-phase, out-of-phase or complex) on material parameters cannot be easily presented, the question of whether the perturbation is stable or unstable can be easily answered from the analysis of the maximal eigenvalue λ_1. As in the nearly equivalent material case, the overall stability of the structure is determined by whether $|\lambda_1|$ is smaller or larger than unity. Deviation of the materials parameters (misfit stresses, diffusivities, etc) and the growth conditions from those corresponding to the nearly equivalent material case changes the shape of the region where the multilayer film grows stably (see Fig. 3.4).

The physical meaning of the eigenvalue λ_1 is how much the amplitude of the instability changes during the growth of a single layer. We can get a sense of how λ_1 for the general case depends on the material and growth parameters by considering how they would affect the amplitude of the perturbation on the surface of a growing *single* layer film of material A or B grown to the thickness of the A or B layers in the multilayer film:

Reproduced with permission of the copyright owner. Further reproduction prohibited without permission.

$$\lambda_A = \exp\left(\Phi_A H_A^* / 2\right) \quad \text{or} \quad \lambda_B = \exp\left(\frac{\Phi_B H_B^* \beta^8}{2\Gamma^4}\right) . \tag{30}$$

Although the parameters in the expression for λ_B depend explicitly on properties of material A due to the normalization employed, the entire expression only depends on the properties of material B.

In order to determine how the physical and growth parameters affect the stability of the growing multilayer film, we construct a series of stability diagrams in which we vary the individual physical or growth parameters. Figure 3.8a shows the stability diagram for the case where the two types of materials are equivalent in every respect except that the thickness of the B-layers is either two thirds or three halves that of the A-layers (and the misfit has opposite sign). The region of stability in this diagram is almost identical to that when the layers have the same thickness (i.e., the nearly equivalent material case – Fig. 3.4) except for a slight shift in the direction of greater (H_B = 2/3 H_A) or smaller (H_B = 3/2 H_A) layer thickness. This can be qualitatively understood by realizing that a thinner B-layer thickness results in a smaller overall bilayer thickness (i.e., $H_A + H_B$). In order to achieve the same bilayer thickness, H_A must be increased over that where $H_A = H_B$. This results in an overall shift of the stability in the direction of larger (H_B = 2/3 H_A) or smaller (H_B = 3/2 H_A) H_A. The vertical shift in Fig. 3.8a is approximately equal to the logarithm of the ratio of the bilayer thickness to that when the A and B layers are equal thickness. Changes in the H_A/H_B do not significantly shift the stable region in the Φ_A-direction. There is, however, a slight change in the shape of the stable region.

The effect of relative misfit stress on film stability is shown in Fig. 3.8b (other A and B material and growth parameters are identical). For the case where the misfit stress in the B layers is -1.1 times that in the A layers, the domain of stable growth is shifted horizontally (in the $-\ln\Phi_A$ direction) relative to the case where the misfit stress in B is equal and opposite that in A. When the misfit stress in the B layers is -0.5 times that in A, the domain of stable growth is shifted horizontally, but in the opposite direction (in the

Reproduced with permission of the copyright owner. Further reproduction prohibited without permission.

+lnΦ_A direction) in addition to an overall expansion and the formation of a new nose at large H_A. The shift along the lnΦ_A axis may be understood by reference to Eq. (30), where we see that the argument in the exponential is proportional to β^8 (recall that $\beta = \Sigma_B/\Sigma_A$). Increasing βcreates an overall increase in the effective value of Φ (i.e., $\Phi_A + \Phi_B\beta^8$). Therefore, the same effective value of Φ is achieved at smaller Φ_A and hence the entire domain of stable growth is shifted toward smaller Φ_A. By the same reasoning, decreasing Φ_B leads to a shift in the domain of stable growth to larger values of Φ_A.

The effect of surface energy on film stability is shown in Fig.3. 8c (other A and B materials and growth parameters are identical – except for misfit which is equal and opposite). Increasing the surface energy of material B leads to an overall expansion of the domain of stable growth while decreasing the surface energy of material B leads to a decrease in the stable domain size. This opposite to the situation found for the misfit stress, as expected on the basis of Eq. (30). In this case too, the large lnΦ peak found when materials A and B are identical (except for the sign of the misfit) breaks into two peaks when the surface energies of the two materials are unequal.

The effect of surface diffusivity on film stability is shown in Fig. 3.8d (other A and B materials and growth parameters are identical – except for misfit which is equal and opposite). Decreasing the surface diffusivity of material B leads to an overall expansion of the domain of stable growth and the splitting of the nose in the in the domain of stable growth. Increasing the diffusivity of material B leads to shrinking of the stability region in the diagram (Fig. 3.8d). Interestingly, even though there is an overall expansion of the domain of stable growth in the case where the surface diffusivity of material B is smaller than that of material A, the splitting of the nose results in a portion of the parameter space that was stable when the surface diffusivity of A and B were identical and is unstable when the diffusivity of B is much smaller than that of A. This added complexity makes it difficult to draw general conclusions about the effects that individual material parameters have on multilayer film stability. The change in size of the

Reproduced with permission of the copyright owner. Further reproduction prohibited without permission.

domain of stable growth can also be understood on the basis of Eq. (30), where the parameter Φ_B is directly proportional to the surface diffusivity. Φ_B is also inversely proportional to the growth rate, such that increasing the growth rate of material B should have the same effect on the stability diagram as decreasing the surface diffusivity.

While we have examined the effects of several material and growth parameters on the stability of multilayer films, some of the parameters may be varied more easily than others. Since surface diffusivity is typically Arrhenius, large variations are possible by changing the temperature with a given system. While all of the other material parameters will likely vary with temperature, these variations are typically small. The largest variations in material parameters will arise when changing the materials that compose the individual layers. Again, the largest variations will typically be found in the surface diffusivity, but changes of order hundreds of percent may be realized in misfit stresses and surface energies as well. On the other hand, the magnitude of variations achievable be changing film thickness is limited by the critical thickness for the formation of misfit dislocations, which is controlled by the magnitude of the misfit. The stability is particularly sensitive to the ratio of misfit stresses and surface energies, which enter Eq. (30) with relatively high powers. Therefore, even though these parameters may not vary as widely as the diffusivity (which enters the exponent in Eq. (30) to the first power), their impact is greater.

In many practical cases of multilayer film growth, the material properties cannot be varied independently. For example, it is often desirable to grow a film under strain balanced conditions; i.e., where the average stress within the multilayer film is zero. This implies that $H_A\Sigma_A + H_B\Sigma_B = 0$. We have examined the effect of varying the misfit stress subject to this constraint. Figure 3.9 shows the stability diagram for five cases with different ratios of misfit stresses $\beta = \Sigma_B/\Sigma_A$ in the range $-1.1 \leq \beta \leq -0.5$, where the ratio of layer thicknesses H_B/H_A is varied accordingly to keep the multilayer film stress-free (i.e., $H_B/H_A = -1/\beta$). As the absolute value of β increases (β is negative) the domain of stable

Reproduced with permission of the copyright owner. Further reproduction prohibited without permission.

multilayer growth in the stability diagram shrinks. This is consistent with our observations above (Fig. 3.8b) which showed the same trend with misfit at fixed layer thickness. Increasing the absolute value of β causes a concomitant decrease in H_B/H_A. However, comparing Fig. 3.9 to Fig. 3.8a (where we vary layer thickness at fixed misfit stresses) shows little correspondence. Therefore, we conclude that variations in layer thickness in order to keep the film stress balanced (zero average stress) is dominated by changes in stress rather than thickness itself. This is consistent with Eq. (30) where we find that stress enters the expression at a much higher power than does layer thickness.

Applying the linear stability analysis presented in this study to real experimental systems is a daunting task. A rough estimate of whether the system is in the linear regime during the growth process is determined by how much the eigenvalue λ_1 differs from unity. This can be deduced from the values of λ_A and λ_B (Eq. 30). Using the data from Ref. [8] on InAs/AlAs superlattices grown on an InP substrate and a number of approximations to make up for missing data (such as surface energy of 1 J/m^2) we computed the values of Φ_A and Φ_B using the known values of lattice constants and elastic moduli for the compounds involved as well as the activation energies of surface diffusion [25]. Using this real and estimated data, we find that these experiments correspond to the unstable region of the stability diagram. This is due, in large part, to the very fast surface diffusion of indium atoms. While the formation of interface modulations is consistent with our predictions of an instability, we suspect that, the linear stability analysis may be of limited utility in this case since the large value of $\ln\Phi_A$ ($\ln\Phi_A \approx 7$ and $lnH_A^* \approx -3.4$ for experiments reported in [8] and, as a consequence, the value of λ_A exceeds unity by a few (seven) orders of magnitude) renders the small amplitude perturbation assumption of the perturbation theory inapplicable after just a few layers. Determination of the true interface morphology after one or two layers requires use of numerical methods capable of handling strongly nonlinear behavior [26].

Reproduced with permission of the copyright owner. Further reproduction prohibited without permission.

A more tractable system would be GaAs/AlAs superlattices [27], where the surface diffusivity of Ga is much lower than that of In. However, this system is almost perfectly lattice matched which leads to low misfit stresses in the layers. This, combined with the low surface diffusivities of the cations [25] leads to a prediction that such a film grows stably, as observed in experiments [27].

Another possibility for testing the linear stability analysis is to turn to superlattices composed of semiconductor alloys rather than of pure A(III)B(V) compounds. Unfortunately, the presence of two or more alloying elements makes the definition of surface diffusion coefficient D_s complicated to determine and, to our knowledge, there are no reliable data for the surface diffusivities of all alloy components as a function of composition. There is a qualitative agreement between the theory presented in this chapter and experiments reported in Ref. [7]. In that study multilayer superlattices of $InAs_yP_{1-y}/Ga_{1-x}In_xP$ were grown. The morphology of the films observed in these experiments, observed using transmission electron microscopy, shows both morphological and compositional modulations of the structure which can be classified as out-of-phase unstable growth.

3.7 Conclusions

In this chapter, we presented a linear stability analysis for epitaxial growth of multilayer thin films. We studied how a shape perturbation on the first layer propagates through the whole multilayer stack. We delineate two factors affecting instability growth. The first factor is surface energy which impedes the growth of the instability. The second factor is to the elastic energy associated with the misfit between the layers and the substrate. This factor favors the growth of curved surfaces and leads to non-flat buried interfaces. In this analysis, we assumed that the transport mechanism that controls the growth of the perturbation is diffusion along the growth surface. We treated the problem

Reproduced with permission of the copyright owner. Further reproduction prohibited without permission.

to first order in perturbation theory, where the small parameter is the product of the amplitude of the shape perturbation and the wave vector of the instability.

In the present analysis, we focused primarily on the special case of a multilayer film, where the materials parameters and growth conditions of the two types of layers are identical, with the exception that the misfit stresses are equal and opposite. We reported our findings in the form of stability diagrams in the layer thickness – normalized surface diffusivity plane. We found that, unlike the case of a thin film consisting of a single layer, there are conditions under which the film is stable, i.e., perturbations to the growth surface decay. For the regions of unstable film growth (where the amplitude of the perturbation grow from layer-to-layer), we distinguish three different types of resulting film morphology, classified according to the complex phase of the characteristic number λ which is a function of materials parameters and growth conditions. Positive λ corresponds to the 'in-phase' perturbation growth mode where perturbations at all interfaces are in phase. Negative λ corresponds to the 'out-of-phase' growth mode where the perturbations at consecutive interfaces are phase-shifted by a half-wave with respect to one another. This leads to a form of "averaged lateral composition modulation" – i.e., the composition within each layer is constant although the through-thickness average composition varies in the plane of the film. A case corresponding to λ which possesses a nonzero imaginary part is characterized by an irregular sign shift between perturbations at consecutive layer interfaces, which is determined by the complex phase of λ. We also determined the wave vector of the propagating perturbation corresponding to the fastest growing instability wave and the rate of perturbation growth.

We also considered the general case, where the two materials and the film growth conditions can vary. We explicitly examined how the surface diffusivity of the two materials, growth rate, surface energy, and film thickness affect the stable domain in the stability diagram. In short, we found that increasing the thickness of one layer shifts the stable growth region in the stability diagram toward the values of smaller bi-layer

Reproduced with permission of the copyright owner. Further reproduction prohibited without permission.

thickness. Increasing the surface diffusivity or, alternatively, decreasing the deposition rate of one of the layers shrinks the stable growth region in the stability diagram. Increasing the magnitude of the misfit stress or decreasing the surface energy produces a similar overall effect; qualitative details of the influence of each of the materials parameter can be understood through consideration of how the parameter modifies λ. Comparing the theoretical predictions of the film morphology with experimentally observed multilayer film structure enabled us to determine the range of applicability of our linear theory.

Reproduced with permission of the copyright owner. Further reproduction prohibited without permission.

References to Chapter III

[1] J. W. Matthews and A. E. Blakeslee, *J. Cryst. Growth*, **29**, 273 (1975).

[2] J. W. Matthews and A. E. Blakeslee, *J. Cryst. Growth*, **32**, 265 (1976).

[3] R. J. Asaro and W. A. Tiller, *Metall. Trans.*, **3**, 1789 (1972).

[4] M. A. Grinfeld, *Sov. Phys. Dokl.*, **31**, 831 (1986).

[5] D.J . Srolovitz, *Acta Metall.*, **37**, 621 (1989).

[6] R. S. Goldman *et al*, *J. Vac. Sci. Technol.*, **B15**, 1027 (1997).

[7] A. Ponchet *et al*, *J. Appl. Phys.*, **75**, 7881 (1994).

[8] S. P. Ahrenkiel *et al*, *J. Appl. Phys.*, **84**, 6088 (1998).

[9] S. T. Chou *et al*, *J. Appl. Phys.*, **78**, 6270 (1995).

[10] K. Y. Cheng, K. C. Hsieh, and J. N. Baillargeon, *Appl. Phys. Lett.*, **60**, 2892 (1992).

[11] J. Mirecki-Millunchick *et al*, *Appl. Phys. Lett.*, **70**, 1402 (1997).

[12] J. Tersoff, C. Teichert, and M.G. Lagally, *Phys. Rev. Lett.*, **76**, 1675 (1996).

[13] D. Leonard *et al*, *Phys. Rev. Lett.*, **63**, 3203 (1993).

[14] D. J. Eagelsham and M. Cerullo, *Phys. Rev. Lett.*, **64**, 1943 (1990).

[15] N. N. Ledentsov *et al*, *Semiconductors*, **32**, 343 (1998).

[16] I. P. Ipatova *et al*, *Phys. Rev.*, **57**, 12968 (1998) and references therein.

[17] D. M. Wood and A. Zunger, *Phys. Rev.*, **B40**, 4062 (1989).

[18] F. Leonard and R.C. Desai, *Phys. Rev.*, **B57**, 4805 (1998).

[19] J. E. Guyer and P. W. Voorhees, *J. Cryst. Growth*, **187**, 150 (1998).

[20] J. Tersoff, *Phys. Rev.*, **B56**, R4394 (1997).

[21] B. J. Spencer, P. W. Voorhees, and S. H. Davis, *J. Appl. Phys.*, **73**, 4955 (1993).

[22] F. Glas, *Appl. Surf. Sci.*, **123/124**, 298 (1998).

[23] W. W. Mullins, *J. Appl. Phys.*, **28**, 333 (1957).

Reproduced with permission of the copyright owner. Further reproduction prohibited without permission.

[24] J. D. Eshelby, *Proc. Roy. Soc. Ser. A*, **241**, 376 (1957).

[25] T. Shitara *et al*, *Mat. Res. Soc. Symp. Proc.*, **312**, 267 (1993).

[26] B. J. Spencer and D.I. Meiron, *Acta metall. mater.*, **42**, 3629 (1994).

[27] Y. Hsu, W. I. Wang, and T. S. Kuan, *J. Vac. Sci. Technol.*, **B14**, 2286 (1996).

[28] C. Teodosiu, *Elastic models of crystal defects* (Springer-Verlag: Berlin, 1982).

Reproduced with permission of the copyright owner. Further reproduction prohibited without permission.

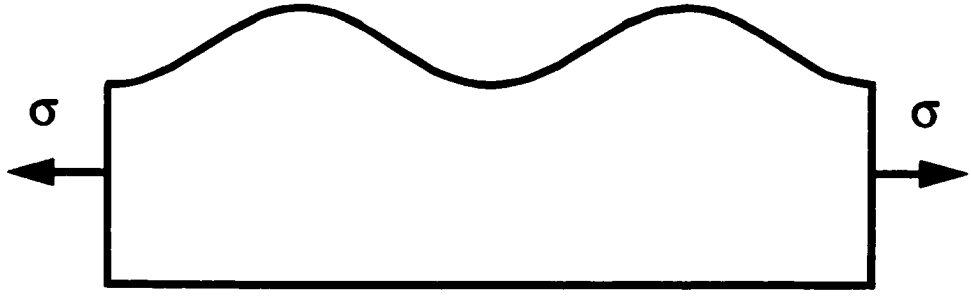


Figure 3.1. A thin film with an undulating surface subjected to a stress σ. For a film in tension, as in this figure, the atomic planes are farther apart from one another in the troughs (the film is more stretched than average) and closer to one another at the crests.

Reproduced with permission of the copyright owner. Further reproduction prohibited without permission.

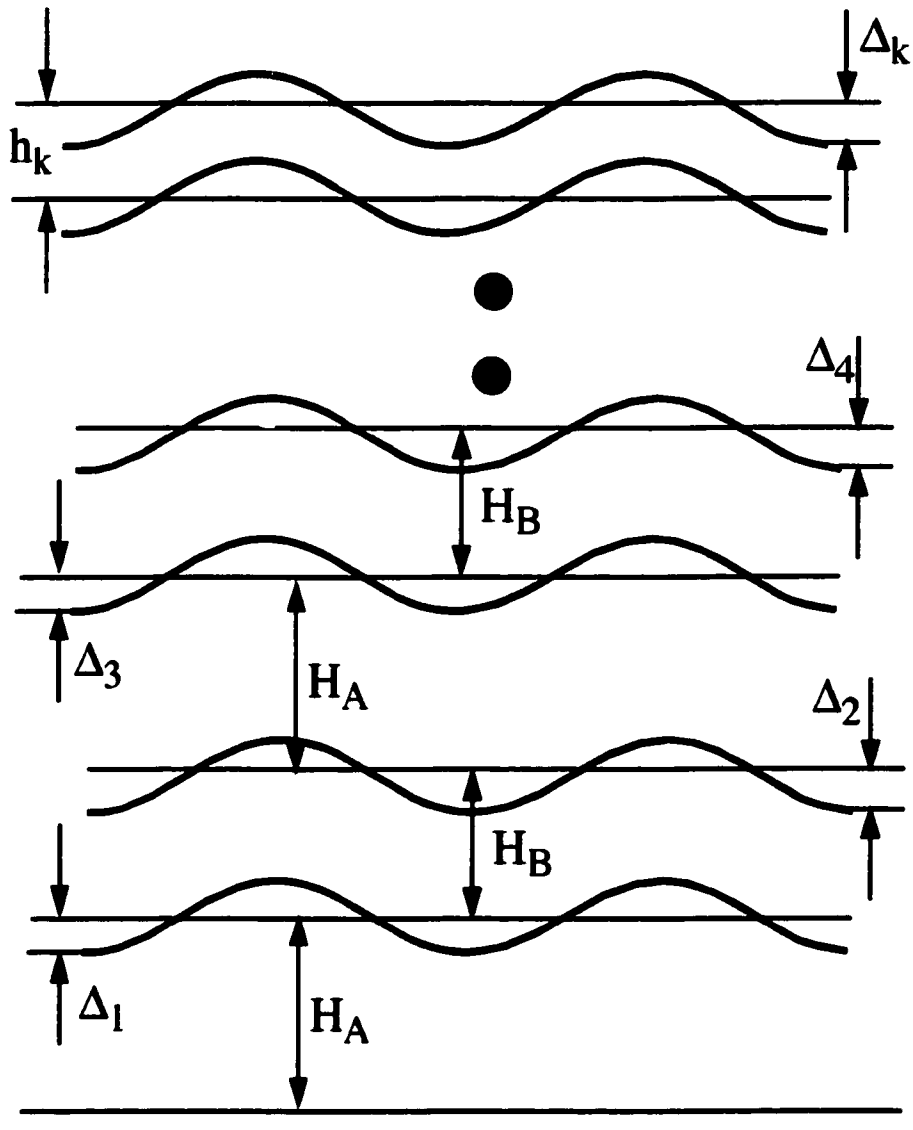
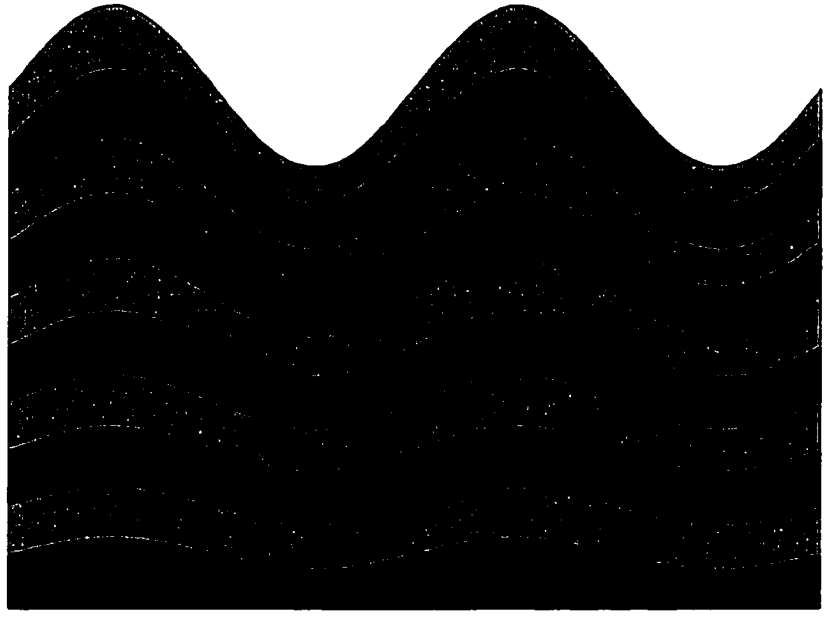


Figure 3.2. A schematic illustration of the multilayer film geometry, indicating the amplitude of the interface undulations Δ and the layer thicknesses H. The odd-numbered layers correspond to material A and the even-numbered ones to material B.

Reproduced with permission of the copyright owner. Further reproduction prohibited without permission.

Fig. 3.3a



Reproduced with permission of the copyright owner. Further reproduction prohibited without permission.

Fig. 3.3b

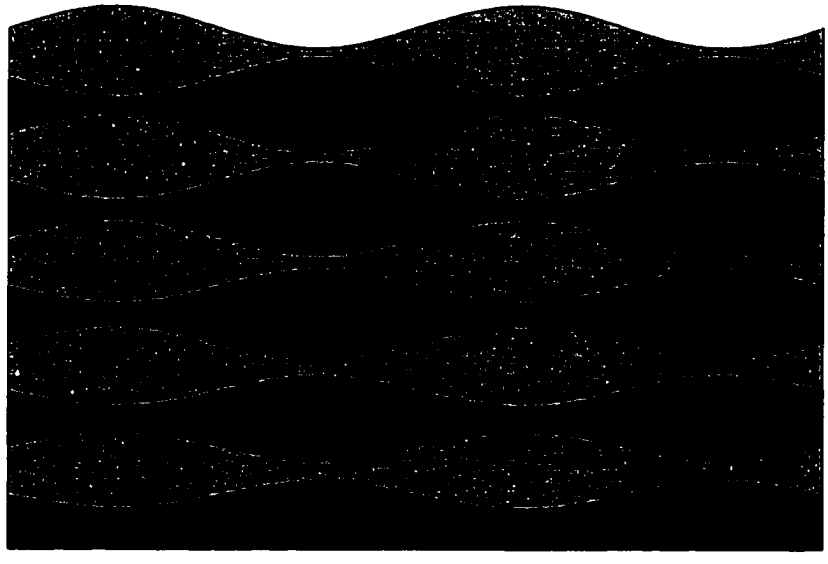


Figure 3.3. Multilayer film morphology produced by an a) in-phase instability and b) an out-of-phase instability. In the latter case, the morphology modulation produces a net composition modulation in the direction parallel to the substrate.

Reproduced with permission of the copyright owner. Further reproduction prohibited without permission.

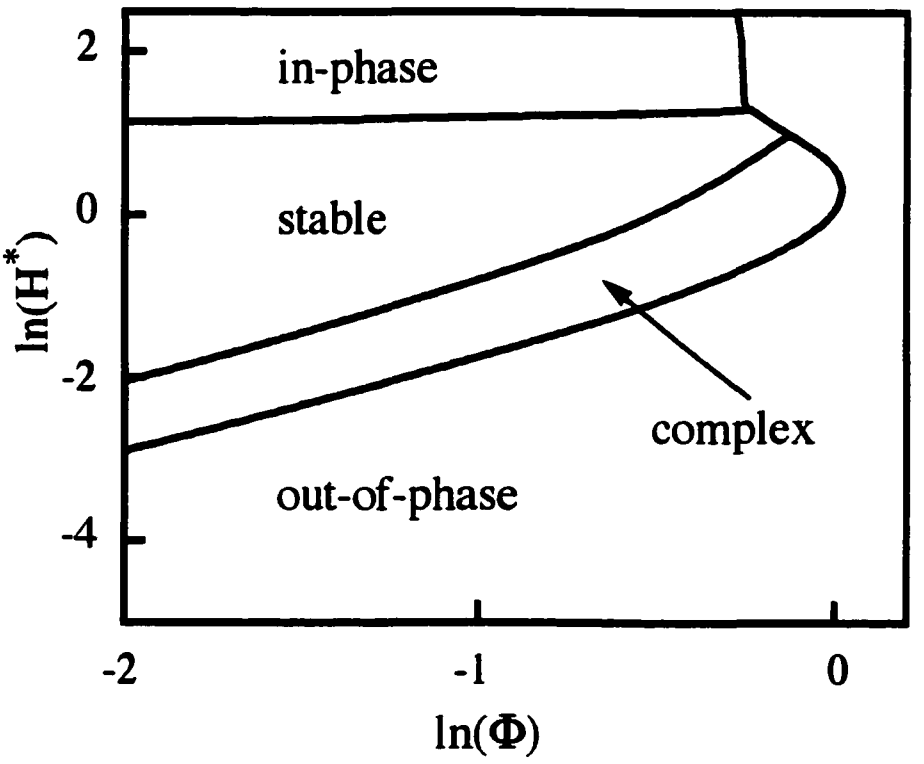


Figure 3.4. Stability diagram for a growing multilayer film, indicating the types of morphologies expected classified according to the eigenvalue λ_{max}. In the region labeled stable, the film will exhibit flat interfaces. In the in-phase and out-of-phase regions, the interface perturbations grow with increasing thickness and are of the form shown in Figs. 3.3a and 3.3b, respectively. The complex region is discussed in the text.

Reproduced with permission of the copyright owner. Further reproduction prohibited without permission.

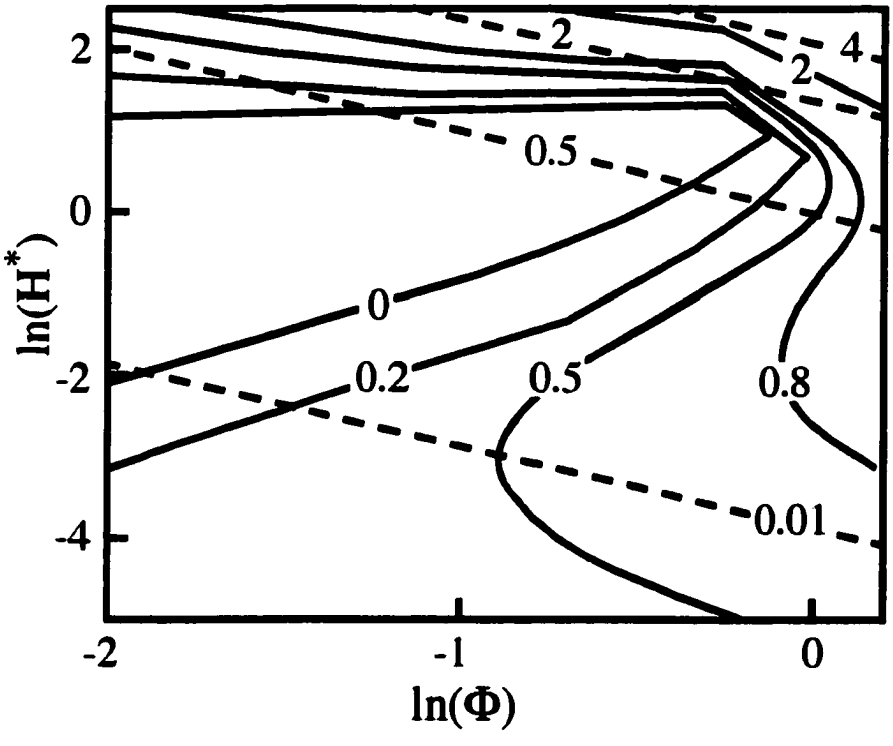


Figure 3.5. Contour plot of the logarithm of the absolute value of λ_{max}. Dashed lines correspond to the case where materials A and B have the same misfit (i.e., contours of the logarithm of λ_s).

Reproduced with permission of the copyright owner. Further reproduction prohibited without permission.

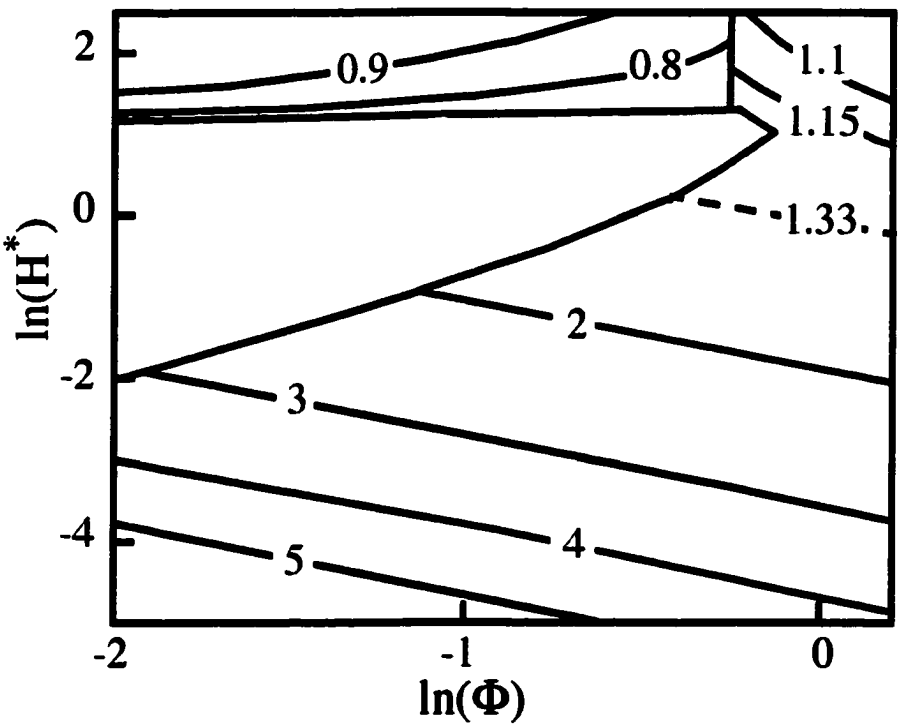


Figure 3.6. Contour plot of ξ^*_{max} for the domains of unstable multilayer growth. The dashed line shows the magnitude of the wave vector (4/3 ξ_0) which discriminates between stable (small wave vectors) and unstable (large wave vectors) perturbations on the surface in the case where materials A and B have the same misfit.

Reproduced with permission of the copyright owner. Further reproduction prohibited without permission.

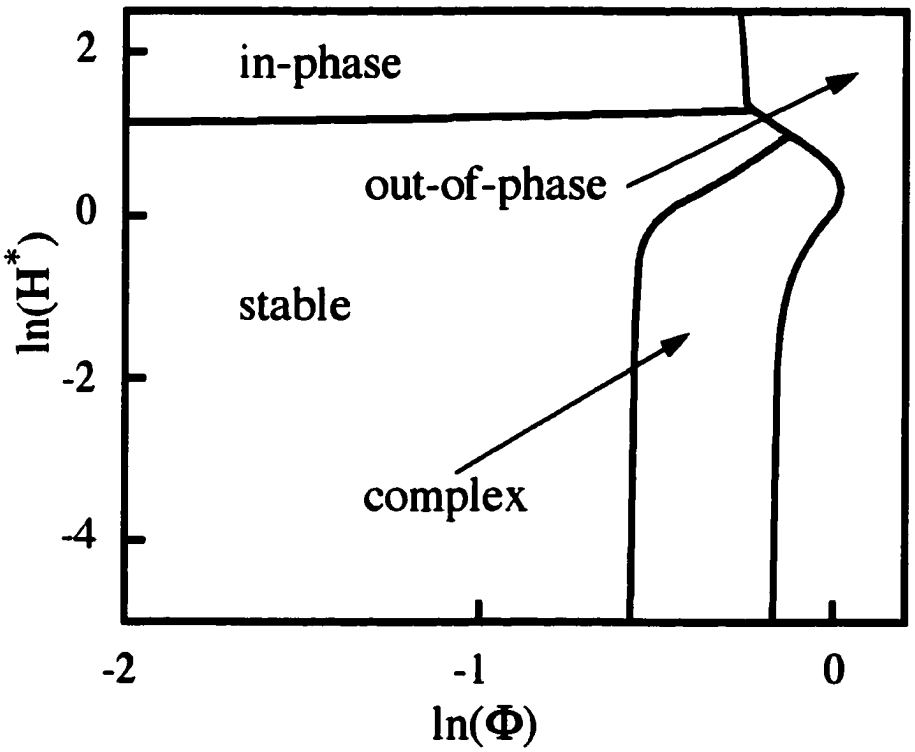
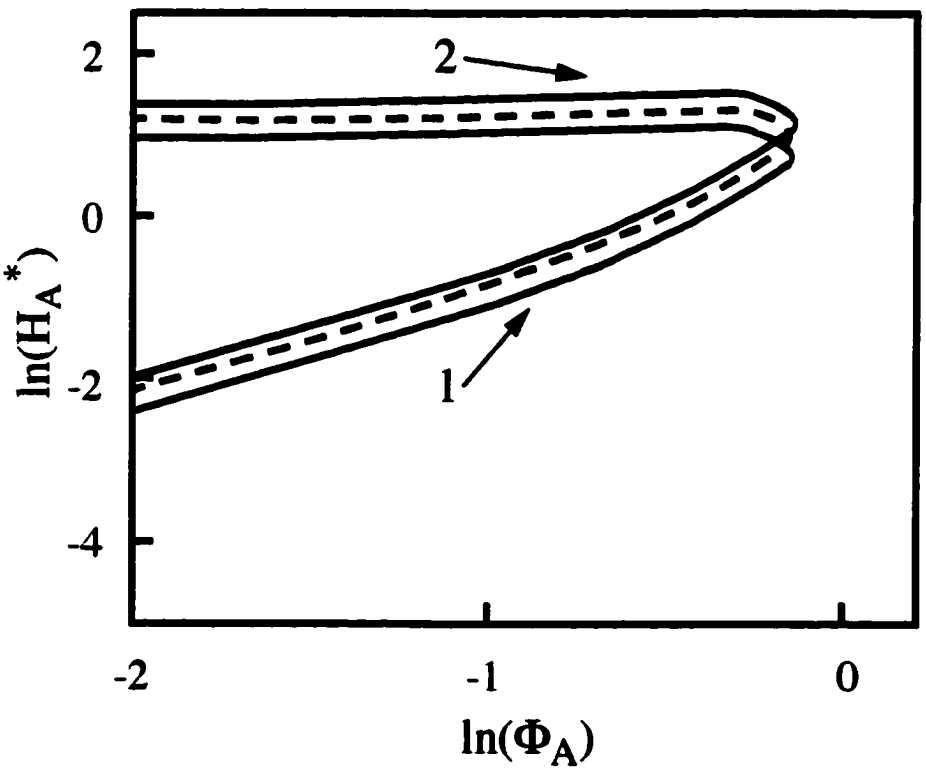


Figure 3.7. Stability diagram for a growing multilayer film with a constraint on the wave vector ξ^*_{max} to values where an initial perturbation on the first layer would grow (i.e., $\xi^*_{max} \leq 4/3$). This constraint greatly enlarges the region of stable growth (cf. Fig. 3.4).

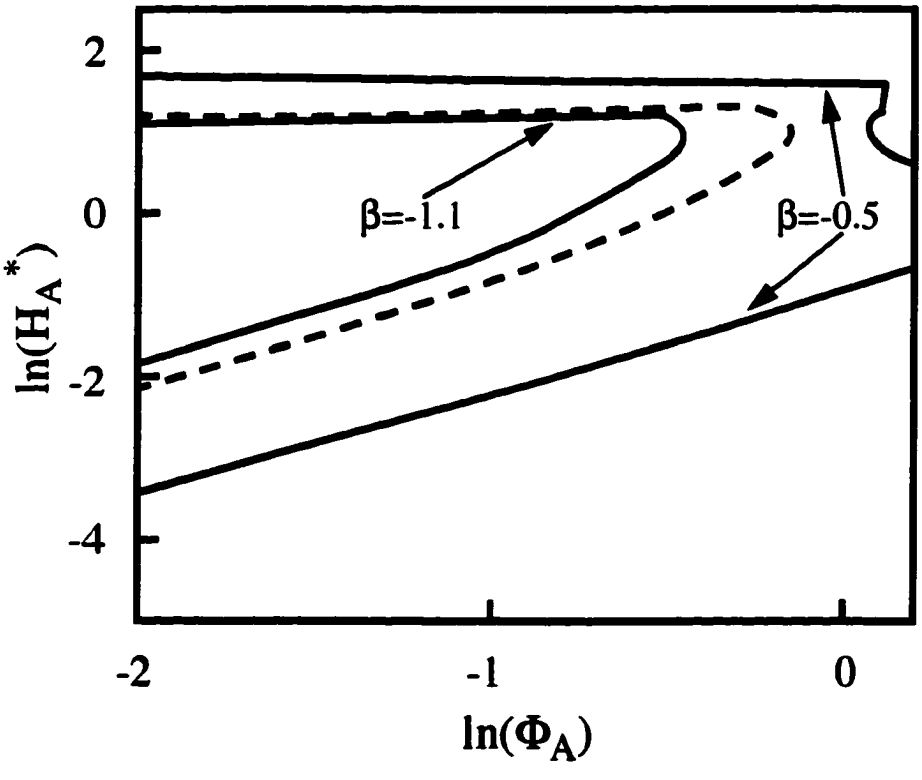
Reproduced with permission of the copyright owner. Further reproduction prohibited without permission.

Fig. 3.8a



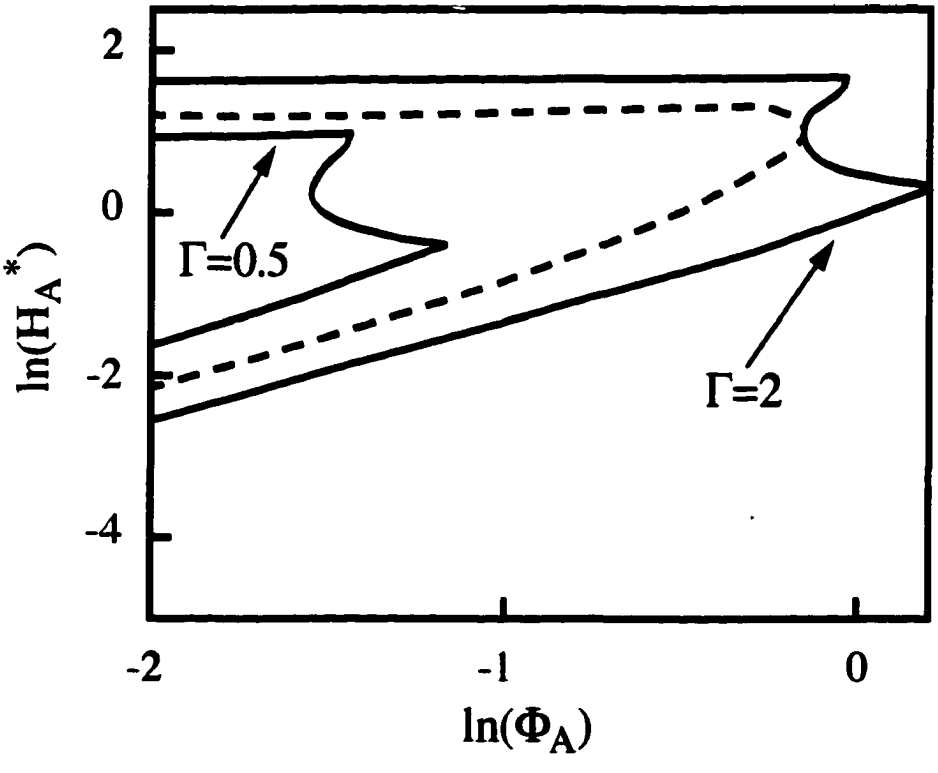
Reproduced with permission of the copyright owner. Further reproduction prohibited without permission.

Fig. 3.8b



Reproduced with permission of the copyright owner. Further reproduction prohibited without permission.

Fig. 3.8c



Reproduced with permission of the copyright owner. Further reproduction prohibited without permission.

Fig. 3.8d

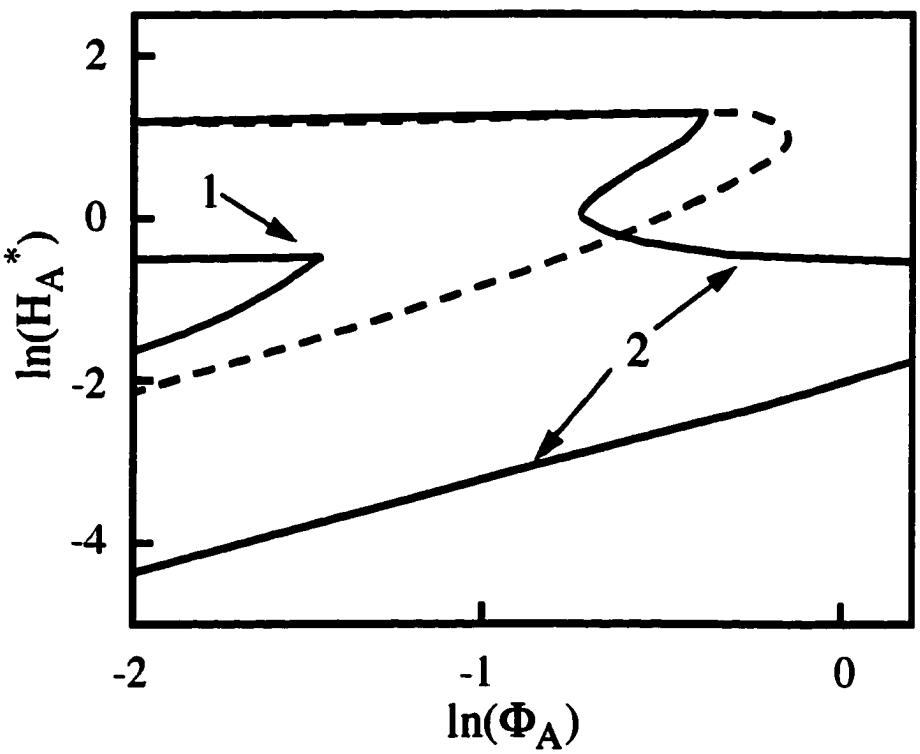


Figure 3.8. Stability diagrams for situations where the materials A and B differ from each other by more than simply the sign of the misfit stress. Figure a) illustrates the influence of relative film thickness. The region of stable growth is bounded by solid curves for $H_A = 2/3\ H_B$ (curve 1) and $H_A = 3/2\ H_B$ (curve 2). Figure b) illustrates the influence of the relative misfit stress ($\beta = \Sigma_B/\Sigma_A$) for $\Sigma_B = -1.1\ \Sigma_A$ and $\Sigma_B = -0.5\ \Sigma_A$ Figure c) illustrates the influence of the relative surface energy ($\Gamma = \gamma_B/\gamma_A$) for $\gamma_B = 0.5\gamma_A$ and $\gamma_B = 2\gamma_A$. Figure d) shows the influence of relative atomic mobility at the growth surface for the case in which $\Phi_A = 0.1\ \Phi_B$. and $\Phi_A = 10\ \Phi_B$. (curve 2). In all figures, the dashed line shows the boundary between stable and unstable growth for the case where materials A and B are identical except for the sign of the misfit stress. Except where noted the material parameters and growth conditions in these figures is exactly the same as for Fig. 3.4.

Reproduced with permission of the copyright owner. Further reproduction prohibited without permission.

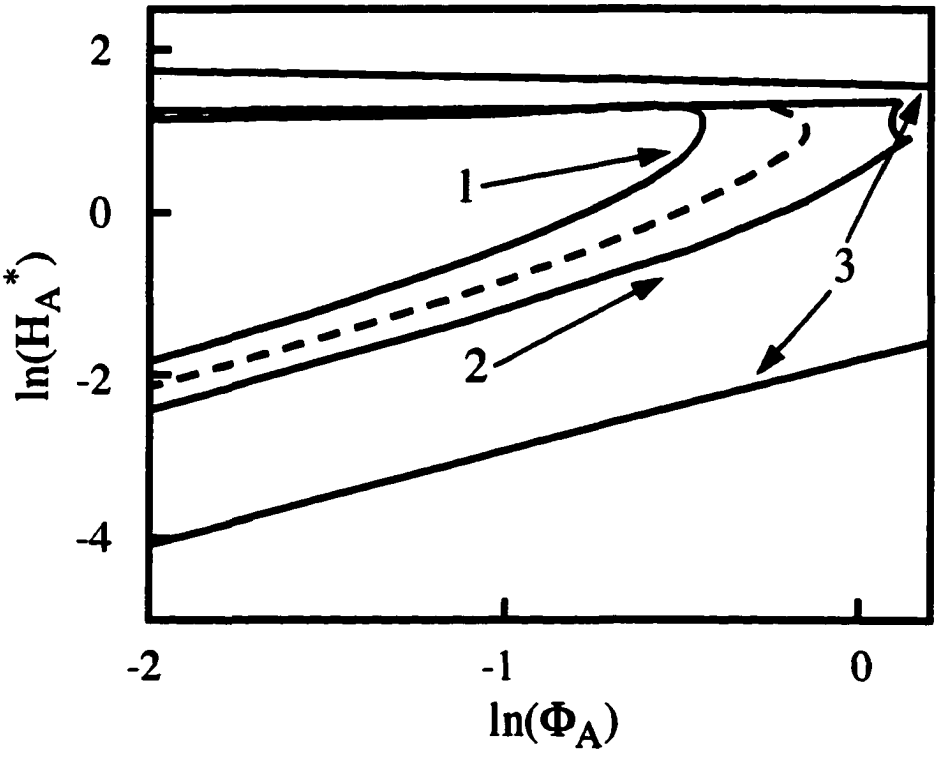


Figure 3.9. Stability diagram for the strain-balance superlattice (i.e., superlattices for which $H_A\Sigma_A + H_B\Sigma_B = 0$). The dashed curve corresponds to the case where materials A and B differ only by the sign of the misfit stress. The curves labeled 1, 2, and 3, correspond to $\beta = \Sigma_B/\Sigma_A$ equals -1.1, -0.9 and -0.5, respectively (with H_A/H_B adjusted to keep the multilayer film strain-balanced).

Reproduced with permission of the copyright owner. Further reproduction prohibited without permission.

CHAPTER IV

ELASTIC MODELS OF SURFACE DEFECTS

4.1 Introduction

Surface defects, such as adsorbed atoms (adatoms) and surface steps play a key role in a number of important surface-related phenomena, including epitaxial growth, surface reconstruction and crystal shapes. One of the central issues in understanding the processes occurring at solid surfaces is an accurate physical description of interactions between defects. The main objective of Chapter IV is to present a study of elastic interactions between surface defects.

Elastic interactions belong to the case of long-range interactions which occur between defects that are far (many atomic diameters) apart from each other. Unlike the case of direct, short-range interactions where two defects are within range of each other's atomic potentials, long-range interactions are mediated by the underlying substrate. There are two distinct origins of long-range interactions [1]. First, perturbations of electronic structure in the vicinity of defects give rise to charge redistribution and, therefore, electrostatic forces between the defects [2]. Second, adatoms and surface steps both distort the underlying substrate, thereby setting-up long-range elastic fields which propagate far into the bulk of the crystal. The interaction between the elastic fields of these defects causes long range defect-defect interactions. Although it is generally not possible to separate these two mechanisms from each other, understanding each of these individually will help to clarify the nature of defect-defect interactions on surfaces. In the present analysis we focus on the elastic interactions.

Reproduced with permission of the copyright owner. Further reproduction prohibited without permission.

Linear elasticity provides a straightforward mathematical explanation of the origin of this interaction. A surface defect, as an imperfection on a solid surface, exerts forces on an otherwise flat defect-free surface. These forces create a field of atomic displacements which extends far into the bulk of the material. Except in the vicinity of the defect core, this displacement field obeys the laws of continuum elasticity. A displacement field produced by two defects can, as a first approximation, be conceived as a sum of two separate displacement fields produced by each defect. The same argument, therefore, applies to the elastic strain field. As a result, the expression for elastic energy of the system of two defects on the surface includes a cross term between the strain fields produced by the defects. This is the case, because elastic energy, in linear elasticity, is quadratic with respect to the components of the strain tensor. It is this cross term that is referred to as the interaction energy between two surface defects. To analyze this energy quantitatively, we present a simple formalism based on the surface Green's function approach.

Unlike topological defects, such as dislocations, where the Burgers vector alone determines the displacement field [3], there is no topological relationship that uniquely specifies the elastic field of a surface defect in terms of its magnitude and orientation. Description of this elastic field, therefore, requires the introduction of a model and its subsequent verification through computer simulations. In this chapter, we analyze elastic interactions between two straight steps using both continuum elasticity and computer simulations. This broad approach enables us to determine the range of applicability of the elastic model of a surface step as well as determine the microscopic parameters which enter the model. Next, we present an elastic model of an adatom on a solid surface and validate this model through atomistic simulations of adatom-adatom interaction. Finally, to present a self-consistent picture of defect interactions, we study the interactions between an adatom and a surface step using the same models as those used to study the interactions between like defects.

Reproduced with permission of the copyright owner. Further reproduction prohibited without permission.

4.2 Elastic field of a surface step

Surface stress

The notion of surface stress is central for the understanding of the model of a surface step. The physical origin of the surface stress can be understood through the following reasoning. The coordination number of atoms at or close to the surface in a solid is different from that in the bulk. As a consequence the equilibrium lattice spacing for the atomic planes at the surface is also different from the lattice parameter of the bulk solid. Since the lattice remains coherent throughout the material, the surface planes are not at their equilibrium lattice parameter resulting in a misfit stress which is referred to as the surface stress.

Mathematically, this stress is defined as the energy required to deform the surface of a solid at constant temperature. A careful thermodynamic analysis of the surface deformation process [4] leads to an expression for the change of total surface energy in terms of elastic strain [5]:

$$d(\gamma S) = S\tau_{ij}d\varepsilon_{ij} \quad (i,j = 1,2) \ , \tag{1}$$

where γ is the surface energy of the solid, S is the surface area and ε_{ij} are the components of the strain tensor at the surface. The quantity τ_{ij} is the surface stress tensor, which can be written as

$$\tau_{ij} = \gamma\delta_{ij} + \frac{\partial\gamma}{\partial\varepsilon_{ij}} \ . \tag{2}$$

Written in this form, the expression for the surface stress distinguishes the processes of creating a free surface (surface energy γ) and deforming it. Unlike liquids, for which the atomic density does not change in the process of surface deformation (due to the freedom

Reproduced with permission of the copyright owner. Further reproduction prohibited without permission.

of the atoms in a liquid to rearrange); in a solid, the lattice must remain coherent resulting in a term in addition to the conventional surface energy.

Cammarata [6] has described some of the consequences of the surface stress, such as its effect on the critical thickness of epitaxially grown thin films, surface reconstructions in metals and strain variation in artificially multilayered films. Macroscopically, the presence of the surface stress can be accounted for imagining that the elastic body is covered by an infinitesimally thin elastic membrane with a misfit stress of magnitude τ which is equal to the surface stress. This assumption alters conventional traction-free boundary conditions at the free surface of an elastic body (see Appendix 2A) which now become [7]:

$$\sigma_{3j} = \frac{\partial \tau_{ij}}{\partial x_j} \text{ and } \sigma_{33} = 0 \quad (i,j = 1,2) . \tag{3}$$

Suo [8] has recently shown that the inhomogeneity in surface stress may reduce the total elastic energy of an elastic body, which may have implications for demixing the components in thin alloy epitaxial films.

Elastic model of a surface step

Within the last fifteen years, several theoretical models for the elastic field of a step have been proposed based upon continuum elasticity and assumptions regarding the step [9],[10]. Surface stress may be used to explain the existence of long range elastic fields associated with surface steps and the related issue of the stability of solid surfaces against faceting. Consider a faceted surface of an elastic solid shown in Fig. 4.1a. Each facet exerts a force upon the bulk of the material caused by the surface stresses at the facet edges. In the limit where the distance between two adjoining facet edges is much larger than the size of each individual facet, a faceted surface can be approximated by an array of alternating point forces on a flat surface (Fig. 4.1b). Using this approximation,

Reproduced with permission of the copyright owner. Further reproduction prohibited without permission.

Marchenko [11] analyzed the stability of a flat solid surface against forming facets by computing the elastic energy created by this arrangement of forces as a function of the facet shape and the magnitude of the surface stresses along each of the two facets.

The picture described above allows us to propose a so-called 'dipole' elastic model of a surface step. Consider a situation when one edge of a facet is much smaller than the other. This is the case of a vicinal surface, which forms when a crystal is miscut by a small angle with respect to a high-symmetry crystallographic plane. Such a surface is composed of flat terraces of the high-symmetry plane edged by identical straight steps. One such step is shown in Fig. 4.1c. Compared with Fig. 4.1a the forces at two adjacent edges are combined into a surface force dipole, which is tilted with respect to the perpendicular to the high-symmetry plane.

Marchenko and Parshin [9] were the first to suggest that the elastic fields of surface steps can be described in terms of tractions on a flat surface related to the surface stress. They argued that the discontinuity of the surface stress sets up a moment M along the surface step of magnitude proportional to the surface stress (see Fig. 4.1c). Marchenko and Parshin argued that this force moment must be compensated by a surface force dipole oriented perpendicular to the surface along the line of the surface step. Using this approach, they estimated the magnitude of this vertical force dipole to be the product of the surface energy $\gamma$and the step height b (more careful consideration given in the same article leads to replacing surface energy γ by surface stress τ). Using this model and working within isotropic elasticity, Marchenko and Parshin predicted that the interaction energy between two identical steps (per unit length of the step) is:

$$E_{\text{int}} = \frac{2(1-\nu^2)}{\pi E}\left[\xi^2 + (\tau b)^2\right]\frac{1}{d_0^2} \qquad (4)$$

where τb is the magnitude of the vertical force dipole and ξ is the magnitude of the force dipole in the lateral direction, d_0 is the separation between two steps, and E and ν are the

Reproduced with permission of the copyright owner. Further reproduction prohibited without permission.

Young's modulus and Poisson ratio of the crystal, respectively. This interaction is repulsive between like steps and decays quadratically with the reciprocal step separation.

Several additional attempts have been made to study step-step interactions theoretically [12-16] in order to understand the energetics of vicinal surfaces in terms of a periodic array of identical steps on flat high-symmetry surfaces. Atomistic simulations of vicinal surface energetics have been performed using different descriptions of atomic interactions [12,13,15]. These simulations show that the interaction energy decays quadratically with the inverse step separation, as predicted by Marchenko and Parshin. While the general arguments presented above clearly lead to the correct functional form for the decay of the elastic field with distance from the step, these simulations did not carefully examine the elastic field of the steps. Nor did these simulations provide the key piece of information needed to fully parameterize the elastic theory for steps; namely, the surface force dipole vector.

Modern electron microscopy techniques have made it possible to indirectly measure the displacement field created by a single step [17]. Recently Stewart, *et al.* [18] analyzed the electron diffraction data from a <211> step on Si {111} in terms of a multipole expansion of the surface tractions. Based upon these results, the authors argue that the leading order term in the expansion is that associated with a surface force dipole; however, some discrepancies between the experimental results and the elastic theory remained.

This section presents atomistic simulation results for <100> steps on a nominally flat {001} surface of nickel and gold. By examining the elastic interactions between steps as a function of the step spacing, we obtain one estimate of the magnitude of the surface force dipole. Next, we perform a detailed analysis of the displacement field associated with a surface step. In order to analyze this data in terms of an elastic model, we derive an anisotropic elastic theory for the elastic field of a step in terms of the surface force dipole vector. We then invert the surface step displacement field obtained from the

Reproduced with permission of the copyright owner. Further reproduction prohibited without permission.

simulation in order to determine the entire surface force dipole vector. The resultant dipole vector yields elastic step interaction energies in reasonable agreement with those obtained directly via atomistic simulation. Finally, an analysis of the elastic theory shows that the relative magnitudes of the components of the surface force dipole vector are determined simply by the anisotropic elastic constants of the crystal

Atomistic simulations of surface steps

We examine [001] steps on the (010) surface of nickel and gold. In order to determine step-step interaction energies, we performed a series of simulations of several ($\bar{1}\bar{m}0$) vicinal surfaces. The geometry of the simulation cell and surface crystallography employed in the present study are shown in Fig. 4.2. In this figure, d_0 denotes the distance between two adjacent steps measured along the terrace in the direction perpendicular to the steps and h is the height of the computational cell. The dimension of the computational cell in the direction in which the step runs is one face centered cubic lattice constant a_0 (which corresponds to two atomic layers), the separation between steps is in the range $8\,a_0 \le d_0 \le 80\,a_0$. Periodic boundary conditions were applied in both the Z-direction (i.e., [001]) and in the [$\bar{m}$10] direction.

The atomic interactions were described using embedded atom method (EAM) potentials [19]. In the this formalism the total energy E_{tot} consists of two distinct parts; a pairwise interaction energy and an on-site energy

$$E_{tot} = \sum_{i=1}^{N}\sum_{j\neq i}\phi(r_{ij}) + \sum_{i=1}^{N} F\left(\sum_{j\neq i}\rho(r_{ij})\right). \qquad (5)$$

where N is the number of atoms in the system, r_{ij} is the separation between atoms i and j and where ϕ, ρ and F are empirical functions fit to the universal binding energy relation and several experimentally determined parameters (elastic constants, lattice parameter,

Reproduced with permission of the copyright owner. Further reproduction prohibited without permission.

vacancy formation energy, etc.). The expressions for the empirical functions employed in the present simulations may be found in [20].

The equilibrium atomic structure and energy of the model were determined by minimizing the total energy with respect to the coordinates of all of the atoms using a conjugate gradient routine [21]. The simulation cell was matched to a perfect crystal lattice of the appropriate lattice parameter at a distance h below the free surface. During the course of the simulation, the height h of the computational cell was gradually increased until the total energy did not change to within an accuracy of 10^{-7} eV. The conjugate gradient method was deemed converged when the maximum force on any atom was less than or equal to 10^{-5} eV/a_0 and when the maximum atomic displacements in any one step were less than or equal to 10^{-6} a_0.

In order to compare the interaction energies obtained in the present simulations with that predicted by Eq. (3), we calculated the surface stress tensor using the expression proposed in [22] :

$$\tau_{\alpha\beta} = -A_c^{-1} \sum_i \sum_k (\mathbf{r}_{k\beta} - \mathbf{r}_{i\beta}) \mathbf{F}_{ki\alpha} \quad . \tag{6}$$

Here $\mathbf{F}_{ki\alpha}$ denotes the α component of the force on the i^{th} atom resulting from its interaction with atom k, $\mathbf{r}_{ki\beta}$ is the β component of the radius-vector from atom i to atom k, and A_c is the area of a unit cell of the surface. For a {010} surface of a cubic material, the surface stress tensor is diagonal, i.e.

$$\tau_{\alpha\beta} = \tau\delta_{\alpha\beta} \quad . \tag{7}$$

Simulation results

The step-step interaction energy E_{int} on $(\bar{1}\bar{m}0)$ vicinal surfaces of gold and nickel as a function of the square of the reciprocal step separation d_0^{-2} is shown in Figs. 4.3(a)

Reproduced with permission of the copyright owner. Further reproduction prohibited without permission.

and (b), respectively. Both sets of data show that over the range of step spacings considered here, the step-step interaction energy is well described by the d_0^{-2} functional form. This is consistent with the prediction of Eq. (4) and with earlier atomistic simulation results [13],[15]. Earlier simulation results [15] suggest that at much smaller step spacings than considered here, higher order terms in the step-step interaction energy dependence of the reciprocal step separation must also be included.

In order to evaluate the agreement of the simulation data with the functional form for E_{int} vs. d_0 predicted by Eq. (4), we fit the data in Fig. 4.3 to the functional form

$$E_{\text{int}} = \frac{A_1}{d_o} + \frac{A_2}{d_o^2} + \frac{A_3}{d_o^3} \quad , \tag{8}$$

The step-step interaction energy is determined from the simulations as indicated in Ref. [15]. If Eq. (7) provided a perfect fit to the entire range of simulation data, A_1 and A_3 would be exactly zero. Table 4.1 shows that A_1 is indeed very small for both Ni and Au. Although A_3 is non-zero, this term makes a negligible contribution to the interaction energy over the range of step spacings examined in the present study. The values for these A_m are similar to those obtained in a previous atomistic study of step-step interactions [15].

The atomic displacement fields associated with individual [001] steps on the (010) surface of gold and nickel are shown in Figs. 4.4 (a) and (b), respectively. These displacement fields were obtained from simulations in which the step separation was $d_0 = 80\, a_0$. In order to demonstrate that the step spacing was sufficiently large to guarantee that step-step interactions do not significantly modify the displacement fields, we also determined the displacement field for the same step in Ni, but with a step spacing $d_0 = 300\, a_0$ (see Fig. 4.4c). The displacement fields for the steps separated by $d_0 = 80\, a_0$ and $300\, a_0$ are indistinguishable.

The maximum atomic displacements associated with the step are $1.9 \times 10^{-2}\, a_0$ in Ni and $5.0 \times 10^{-2}\, a_0$ in Au. Excluding a region of radius $1\, a_0$ around the upper step edge,

Reproduced with permission of the copyright owner. Further reproduction prohibited without permission.

the maximum atomic displacements are 6 x 10^{-3} a_0 in Ni and 1.6 x 10^{-2} a_0 in Au. Since most of the remaining displacements are very small compared with the atomic separation, we expect that linear elasticity should be applicable for describing the elastic field of the step (except, perhaps, within a very small region immediately surrounding the core of the step).

Table 4.1

	A_1 (eV)	A_2 (eV Å)	A_3 (eV Å^2)
Au	0.0003±0.0002	0.17 ± 0.02	-0.62 ± 0.34
Ni	0.00003±0.00002	0.045 ± 0.001	-0.14 ± 0.02

Table 4.1. The coefficients of $(d_0)^{-m}$ in the expansion of the step-step interaction energy E_{int} vs. the inverse interstep spacing d_0, as per Eq. (8).

The displacement fields associated with the steps in Au and Ni (Fig. 4.4 (a) and (b)) are very similar. They are characterized by decreasing magnitude with distance from the step. In both cases, there is a plane, canted with respect to the vertical, across which the out-of-plane displacements change sign. The in-plane displacements also change sign as this same plane is crossed. Therefore, in both the Au and Ni cases, the step displacement fields exhibit a plane of zero (or nearly zero) displacement which is canted toward the upper side of the step. The fact that this plane is canted with respect to the surface normal is unexpected, since the simplest model of a surface step (based upon Marchenko and Parshin's surface stress argument) implies a surface force dipole oriented perpendicular to the nominal surface.

Although it is possible to analyze the displacement field associated with the surface step (determined from the simulations) in terms of an isotropic elastic surface force dipole vector model, such an analysis would be inappropriate because the elastic

Reproduced with permission of the copyright owner. Further reproduction prohibited without permission.

anisotropy in nickel is substantial. One of the effects of this anisotropy can be seen in Fig. 4.4. If both Au and Ni were isotropic, then the step displacement fields in these two materials would be identical with the possible exception of an overall scale factor. Careful examination of Figs. 4.4 (a) and (b) show that the planes about which the displacements change signs occur at different angles in these two materials. Therefore, an anisotropic elastic analysis of the displacement fields of the step is necessary.

Elastic analysis

Consider the case of a step oriented parallel to the OZ direction on a surface with normal OY (see Fig. 4.2). The direction OX lies within the surface, perpendicular to the direction along which the step runs. The step is at the origin of the coordinate system. Further, let the material occupy the half-space $y > 0$. The displacement field associated with any distribution of surface tractions can be written as a convolution of these tractions $\mathbf{T}(x,z)$ with the elastic surface Green tensor $\mathbf{G}(x,y,z)$:

$$\mathbf{u}(x,y,z) = \int dS\, \mathbf{G}(x-x', y, z-z')\, \mathbf{T}(x', z') \tag{9}$$

In the straight surface step case, the problem is strictly two dimensional, since the surface tractions are assumed to be uniform along the step line, i.e. they are independent of the coordinate along a step. These tractions will be denoted as $\mathbf{T}(x)$. The Green tensor $\mathbf{G}(x,y,z)$ can, therefore, be integrated along the step direction to yield $\mathbf{G}(x,y)$.

In Marchenko and Parshin's model, the tractions produced by a step are assumed to be associated with a surface line force dipole which, in the most general case, may be tilted with respect to the surface

$$\mathbf{T}(x) = \mathbf{D}\delta'(x) \ . \tag{10}$$

Reproduced with permission of the copyright owner. Further reproduction prohibited without permission.

where δ' is a derivative of a delta-function and **D** is the surface force dipole vector. The resultant expression for the displacement field associated with a single surface step is simply (inserting Eq. (10) into Eq. (9))

$$\mathbf{u}(x,y) = \mathbf{g}(x,y)\mathbf{D} \tag{11}$$

where $\mathbf{g}(x,y)$ is a three by three matrix:

$$\mathbf{g}(x,y) = -\frac{\partial}{\partial x}\mathbf{G}(x,y) \ . \tag{12}$$

The tensor **g** is easily obtained for the case of an isotropic medium [23] from the well-known isotropic elastic surface Green tensor $\mathbf{G}(x,y,z)$ [24]. For our purposes, the main feature of this tensor is that (in polar coordinates) each of its components can be factored as a product of an angular part $\mathbf{f}_{ij}(\theta)$ and a radial part which is proportional to $1/r$, where r is the distance from the origin. The off-diagonal elements of the matrix **f** vanish at the surface and exhibit the following symmetry:

$$\mathbf{f}_{xy} = -\mathbf{f}_{yx} \ . \tag{13}$$

For an anisotropic medium, an analytical expression for **G** can be obtained only for the case of hexagonal symmetry [25]. However, for two-dimensional problems, the complexity of the problem can be significantly reduced by using the formalism developed by Stroh [26]. The expression for the derivative of the surface Green tensor **g**, derived in this way, is presented in Appendix 4A. For the case of a step oriented along <001> on a {001} surface of a cubic crystal, an expression for **g** can be found analytically in closed form. The elements of the derivatives of the surface Green tensor **g** in polar coordinates are

Reproduced with permission of the copyright owner. Further reproduction prohibited without permission.

$$\mathbf{g}=\begin{pmatrix} \frac{1}{r}\frac{\mathbf{f}_{xx}(\theta)}{\pi L d(\theta)} & \frac{1}{r}\frac{\mathbf{f}_{xy}(\theta)}{\pi L d(\theta)} \\ \frac{1}{r}\frac{\mathbf{f}_{yx}(\theta)}{\pi L d(\theta)} & \frac{1}{r}\frac{\mathbf{f}_{yy}(\theta)}{\pi L d(\theta)} \end{pmatrix} \tag{14}$$

where

$$\begin{aligned} \mathbf{f}_{xx}(\theta) &= C_{44}\cos(\theta)\left(C_{12}\cos^2(\theta)-C_{11}\sin^2(\theta)\right) \\ \mathbf{f}_{xy}(\theta) &= C_{44}\sin(\theta)\left(C_{12}\sin^2(\theta)-C_{11}\cos^2(\theta)\right) \\ \mathbf{f}_{yx}(\theta) &= C_{44}\sin(\theta)\left(C_{11}\sin^2(\theta)-C_{12}\cos^2(\theta)\right) \\ \mathbf{f}_{yy}(\theta) &= \cos(\theta)\left(H\cos^2(\theta)(C_{11}+C_{12})+C_{12}C_{44}+(C_{11}+C_{12})(C_{11}-C_{12}+C_{44}\cos^2(\theta))\right) \end{aligned} \quad , \tag{15a}$$

$$d(\theta)=H\left(C_{11}+C_{12}\right)\cos^2(\theta)\sin^2(\theta)+C_{11}C_{44} \quad , \tag{15b}$$

and

$$L=\frac{C_{44}(C_{11}-C_{12})}{\sqrt{\left(4\frac{C_{11}C_{44}}{C_{11}+C_{12}}+H\right)\left(\frac{C_{11}C_{44}}{C_{11}+C_{12}}\right)}} \quad . \tag{15c}$$

H is the elastic anisotropy of the cubic crystal: $H=C_{11}-C_{12}-2C_{44}$, and C_{11}, C_{12}, and C_{44} are the three unique elastic constants of a cubic crystal. The form of Eqs. (14) and (15) preserve the same structure of the derivative of the Green tensor found in the isotropic case: the radial parts are all proportional to $1/r$. The angle θ is measured from the OX axis to the OY axis in a counterclockwise manner. All elements of the tensor $\mathbf{g}$ in which one of the indices is z are identically zero except for $\mathbf{g}_{zz}$. However, because of the symmetry of the surface step problem, the magnitude of the dipole force in the OZ direction is zero.

Given the green tensor $\mathbf{g}$, the interaction energy between two identical steps E_2 can be readily obtained from the general expression for the elastic interaction energy between two surface loads:

Reproduced with permission of the copyright owner. Further reproduction prohibited without permission.

$$E_{int} = \int dS\, \mathbf{T}_1(x,z)\, \mathbf{u}_2(x,z) \ , \tag{16}$$

where $\mathbf{T}_1(x,z)$ is the traction associated with the first load and $\mathbf{u}_2(x,z)$ is the displacement vector associated with the tractions of the second load and the integral is evaluated over the entire surface. Inserting Eqs. (10) and (11) into Eq. (16) yields

$$E_2 = \frac{\mathbf{DD}}{\pi L d_0^2} = \frac{\mathbf{D}_x^2 + \mathbf{D}_y^2}{\pi L d_0^2} \tag{17}$$

The interaction energy of a periodic array of parallel, identical steps was derived in [15] in terms of the pair interaction energy E_2 and is given by

$$E_{int} = \frac{\pi^2}{6} E_2 = \frac{\pi}{6} \frac{\mathbf{D}_x^2 + \mathbf{D}_y^2}{L d_0^2} \tag{18}$$

This result is the anisotropic generalization of the isotropic result of Marchenko and Parshin [9] presented in Eq. (4), for the case of a [100] step on a {001} surface of a cubic crystal. Like the isotropic theory and the simulation results, this interaction energy decays with step spacing as d_0^{-2}. In terms of the expansion of the step-step interaction energy data for the vicinal surface in terms of the inverse step spacing, the parameter A_2 in Eq. (8) is:

$$A_2 = \frac{\pi}{6} \frac{\mathbf{D}_x^2 + \mathbf{D}_y^2}{L} \ . \tag{19}$$

The only unspecified parameters in this analysis are $\mathbf{D}_x$ and $\mathbf{D}_y$ which, together, specify the orientation of the surface line force dipole. Comparison of Eq. (19) with the simulated elastic step-step interaction energy data from the simulation (presented in Table 4.1), allows direct determination of $\mathbf{D}_x^2 + \mathbf{D}_y^2$. The individual components of the surface line force dipole vector may be extracted directly from the displacement field determined in the atomistic simulations. Both of these analyses are performed below.

Reproduced with permission of the copyright owner. Further reproduction prohibited without permission.

Comparison of simulation and elasticity results

The simulation results presented above suggest that the leading order term in the expansion of the step-step interaction energy in a series of reciprocal powers of distance is quadratic, i.e., d_0^{-2}. This is consistent with the predictions of both the isotropic and our anisotropic elastic theories that model the elastic field of a step in terms of a surface line force dipole. Non-zero higher order terms in this expansion may be associated with surface force distributions which contain quadrapole or higher order terms. The next order term in the expansion of the step-step interaction energy d_n^{-3} is associated with the interaction between a dipole on one step and a quadrapole on another step [27]. The relative contribution of this third order term can be estimated in terms of a dimensionless parameter

$$K = \left| \frac{A_3}{d_0 A_2} \right| . \tag{20}$$

For $K < 0.2$, the third order term makes less than a 20% correction to the step-step interaction energy. Using the simulation data in Table 4.1, this only occurs for step spacings less than approximately 18 Å in Ni and Au (i.e., less than 5 lattice parameters). Although it is not possible to extract the surface line dipole force vector (or its magnitude) from elastic theories, comparison of atomistic simulation and elastic theory results can be employed to uniquely determine this dipole force vector.

The most direct method for extracting the surface line force dipole vector from the atomistic simulations is by direct comparison of the displacements determined via the simulation with the analytical, anisotropic form of Eqs. (11)-(15). The two independent components of the surface line force dipole vector $\mathbf{D}_x$ and $\mathbf{D}_y$ were chosen to provide the best fit to the displacement field obtained from the simulations using a least squares fitting procedure. There is ambiguity on the scale of an interatomic spacing as to the exact location of the surface step. We arbitrarily assumed that the step is located at the

Reproduced with permission of the copyright owner. Further reproduction prohibited without permission.

upper corner of the step (i.e., at the edge of the upper terrace). In order to exclude the effect of surface relaxation, we excluded all atoms within the three (020) planes closest to the surface from the fit. Similarly, to eliminate the effects of non-linear elastic displacements near the "core" of the step, we also excluded all atoms that were within a radius of four atomic spacings of the step from the fit. The best fit, anisotropic elastic displacement field associated with a surface line force dipole is shown in Fig. 4.5 (a) and (b) for the case of an [001] oriented step on a (010) surface in gold and nickel, respectively. Comparison of Figs. 4.4 and 4.5 show that the theoretical predictions of the displacement fields are in excellent agreement with the atomistic data for both nickel and gold everywhere, except for some small differences very near the step itself. It is also possible to invert the Green tensor for the surface line dipole Eq. (11) locally, at each atomic position, and investigate the variation of the surface line force dipole needed to produce that local displacements and the magnitude of the parameter A_2 in the step-step interaction energy obtained from Eq. (19). For all but a small number of points, this procedure produces only small variations in the surface line force dipole values and the step-step interaction energy coefficient A_2. This further demonstrates the accuracy and consistency between the anisotropic elastic analytical predictions of the step elastic field and that found from our atomistic simulations.

The "core" of the step is the region near the step in which the linear elastic theory fails to accurately describe the atomic displacement field. Although, this definition of core size depends on the threshold we use to determine whether the displacement fields are sufficiently accurately reproduced by linear elasticity, we can make a reasonable choice, such that small changes in this threshold do not change significantly change the core size. Using the best fit values of $\mathbf{D}_x$ and $\mathbf{D}_y$ and a threshold error of 10%, we estimate the step core radius to be approximately 3 a_0 for these steps in both Ni and Au.

Table 4.2 shows the values of $\mathbf{D}_x$ and $\mathbf{D}_y$ obtained by fitting Eq. (11) to the displacement field found from the atomistic simulations. In order to establish the

Reproduced with permission of the copyright owner. Further reproduction prohibited without permission.

consistency of these results with respect to the simulations, Table 4.2 compares the magnitude of the step-step interaction energies (A_2) obtained by varying the step spacing in the simulations directly with the predictions of the analytical theory, Eq. (19). The resultant values agree to within 15% for both Au and Ni. We note that an error of order $+\varepsilon$ in $\mathbf{D}_x$ and $\mathbf{D}_y$ leads to an error of up to 4ε in A_2. Therefore, we conclude that the errors in $\mathbf{D}_x$ and $\mathbf{D}_y$ are in the range of 4% to 15%. On this basis, we conclude that the analytical anisotropic elastic theory is in excellent agreement with the simulations.

In Marchenko and Parshin's [9] original paper on step-step interactions, they speculated that the magnitude of the line force dipole oriented normal to the surface is equal to the product of the surface stress and the step height, i.e., τb. In order to examine this assertion, we have calculated the surface stress for the {001} surface of Ni and Au. The data are tabulated in Table 4.3, along with the {001} surface energy determined from the simulation and polycrystalline average surface energies determined experimentally. The surface stress is found to be 1-4 times larger than the surface energy. Hence approximating one with the other would be a poor approximation. Additionally, the computed surface energies are significantly smaller than the experimental values. This is due in large part to the fact that the EAM potentials routinely underestimate the surface energies of fcc metals and that the experimental values are polycrystalline averages. Inserting the surface stress values determined from these simulations into the expression for the step-step interaction energy parameter for the vicinal surface (A_2 in Eq. (19)), we find that Marchenko and Parshin's speculation that the magnitude of the surface line force dipole is equal to the product of the surface stress and the step height yields results that are of the correct order of magnitude. However, only including the τb term in A_2 ignores the possibility of a force dipole in the plane of the surface (see Eq. (4), above). Such a term would only further increase Marchenko and Parshin's predicted value of A_2, which is already too large by approximately 100% compared with the simulation results.

Reproduced with permission of the copyright owner. Further reproduction prohibited without permission.

Table 4.2

(a)

Au	D_x	D_y	A_2
Simulations	-	-	0.15
Theory (fit)	0.17	0.18	0.13
τb	-	0.40	0.34
γb	-	0.12	0.03

(b)

Ni	D_x	D_y	A_2
Simulations	-	-	0.039
Theory (fit)	0.15	0.13	0.033
τb	-	0.29	0.070
γb	-	0.17	0.025

Table 4.2. The two independent components of the surface line force dipole $\mathbf{D}_x$ and $\mathbf{D}_y$ (eV/Å) and the coefficient A_2 (eV Å) of the $(d_0)^{-2}$ in the expansion of the step-step interaction energy E_{int} vs. the inverse interstep spacing d_0, as per Eq. (8) with $A_1 = A_3 = 0$ (as discussed in the text). Table 4.2a presents data for Au and Table 4.2b presents data for Ni. The "Theory (fit)" data was obtained from a least square fit of Eq. (11) to the simulation data. The value of A_2 in the row labeled "Simulations" was determined from Fig. 4.5. The data in the rows labeled "τb" and "γb" were obtained using Eqs. (11) and (19) and the values of the surface stress and surface energy determined in the present simulations. $b = a_0/2$ is the surface step height.

Reproduced with permission of the copyright owner. Further reproduction prohibited without permission.

Table 4.3

	τ (eV/Å^2)	γ(eV/Å^2)	$\bar{\gamma}_{exp}$ (eV/Å^2)
Au	0.196	0.057	0.094
Ni	0.164	0.098	0.149

Table 4.3. The surface stress τ and surface energy γ of the {001} surface of Au and Ni determined from the present atomistic simulations. For comparison, we also enclose the surface energy determined from experiments using polycrystalline samples $\bar{\gamma}_{exp}$. [28].

Both the displacement fields obtained from the atomistic simulations and those determined using Eq. (11) (see Figs. 4.4 and 4.5) show that a plane exists along which the atomic displacements are very nearly zero. This plane passes through the step and hence occurs at some angle, which we label θ_0. Analytically, the occurrence of such a zero displacement plane at θ_0 implies that the following condition must be satisfied

$$\mathbf{g}(\theta_0)\mathbf{D} = 0 \tag{21}$$

This can only occur if the determinant of $\mathbf{g}$ at θ_0 is identically zero. For the step geometry considered here (i.e., <100> steps on a {001} surface), this implies that θ_0 must satisfy the following condition

$$\tan^2\theta_0 = \frac{C_{11}}{C_{12}}. \tag{22}$$

Therefore, the angle of the zero displacement plane is simply a function of the elastic constants. Eq. (21) is a necessary condition in order to satisfy Eq. (21), but not a sufficient one. Using the value of θ_0 determined in Eq. (21), we find that Eq. (20) is satisfied only if the two components of the surface line force dipole vector satisfy the following relation:

Reproduced with permission of the copyright owner. Further reproduction prohibited without permission.

$$\frac{D_y}{D_x} = \frac{C_{44}}{\sqrt{C_{11}C_{12}}} \quad . \tag{23}$$

Equation (23) implies that the ratio of the two components of the surface line force dipole vector is determined solely by the elastic constants of the material.

Ni and Au have much different elastic anisotropies; H(Au) = -0.40 eV/Å^3 and H(Ni) = -1.10 eV/Å^3, using the elastic constants derived from the EAM potentials. However, these anisotropies produce only a relatively small difference in θ_0; θ_0(Au) = 47.0° and θ_0(Ni) = 50.9°. θ_0 can also be extracted from the displacement fields shown in Fig. 4.4, which were determined from the atomistic simulations. These values determined from the simulations are θ_0(Au) = 50° ± 3° and θ_0(Ni) = 51° ± 2°. The values of θ_0 determined from the elastic constants (Eq. 22) are within the error bars of those obtained from the simulations. Although the predicted values for θ_0 for Au and Ni are very similar, the values determined from the simulations are such that θ_0(Au) < θ_0(Ni), in agreement with the theoretical predictions. The predicted angles could be better tested in a material such as diamond where the anisotropy is very large: θ_0(diamond) = 71°.

4.3 Elastic model of adatom interactions on a solid surface

The interaction between adatoms on a solid surface plays a central role in the nucleation stage of islands on a substrate and layer-by-layer (Frank-van der Merwe) film growth [29,30]. There are several distinct methods by which adatoms interact, including via electronic and elastic effects [1,31]. Although the energy associated with the elastic interaction between surface defects is small, these elastic interactions can give rise to growth instabilities in heteroepitaxy [32]. Lau and Kohn [33], Lau [34] and Marchenko and Parshin [9] suggested that these elastic interactions can be described by replacing the surface defect with a distribution of surface forces which interact elastically through the underlying substrate. Marchenko and Parshin [9] represented these forces describing an adatom as a surface force point dipole tensor and solved for the elastic interaction

Reproduced with permission of the copyright owner. Further reproduction prohibited without permission.

between these dipoles on an isotropic elastic substrate. Neglecting the out-of-plane component of the surface force and assuming that the force dipole tensor is diagonal (i.e., the adatom is symmetric), the interaction energy between two identical adatoms E_{int} was found to be : [9,33]

$$E_{int} = \frac{1-\nu^2}{\pi E}\frac{A^2}{R^3}, \tag{24}$$

where E and ν are the Young's modulus and Poisson ratio of the substrate, A is the magnitude of the adatom force dipole and R is the distance between the adatoms. This interaction energy is always positive, such that identical adatoms always repel each other. If the isotropic substrate is replaced with an anisotropic one, the equation describing the adatom interactions change dramatically. Using the surface elastic Green's function obtained by Portz and Maradudin [35] for the case of cubic symmetry, Lau [34] found that the interaction between adatoms may be attractive along certain crystallographic directions. Kappus [36] using a different technique, verified this result. Experimental observations using field ion microscopy [37] suggest that adatoms may either attract or repel each other, depending on their relative positions on the surface.

The magnitude of an adatom force dipole can only be found from microscopic consideration of interatomic interactions in the vicinity of the adatom since, unlike in the case topological defects such as dislocations [3], there are no topological parameters that uniquely describe the full elastic field of the adatom. In an attempt to address this problem, Lau [34] used a van der Waals interatomic potential to describe the interaction between Xe atoms on graphite in order to determine the magnitude of the force dipole A.

We performed a series of atomistic simulations of adatoms on a surface and made direct comparisons between the atomistic simulation results and the predictions of an anisotropic elastic analysis of adatom interactions. More precisely, we used atomistic simulations (containing up to 64,000 atoms) to investigate the interactions between Ni adatoms on a (001) Ni surface. The data, then, served as an input for the elastic analysis

Reproduced with permission of the copyright owner. Further reproduction prohibited without permission.

in order to determine the unknown dipole force tensor of an adatom. The adatom-adatom interaction energy as a function of orientation determined from the simulation was compared with a simple, analytical prediction of adatom-adatom interactions obtained using anisotropic elastic theory. Detailed agreement between the atomistic simulations results and the predictions of the elastic analysis were obtained provided that the adatoms are sufficiently far away from each other that higher order terms in the multipole expansion of the adatom traction are insignificant. The present results, also, show that an isotropic analysis of adatom-adatom interactions is both quantitatively and qualitatively incorrect and that the dipole model in the anisotropic analysis provides an accurate description of adatom-adatom interactions except in crystallographic directions in which the dipole interactions are very small.

Elastic analysis of adatom interactions

Consider an adatom on the surface of an elastic solid occupying the half-space $z > 0$. The adatom exerts tractions $\mathbf{T}$ on the surface, which at distances much larger than the adatom size can be thought of as point forces. Since the total force the adatom exerts must be equal to zero, it is possible to view the tractions $\mathbf{T}$ as an expansion into a series of multipoles [38] without a monopole term. The out-of-plane (z) component of the force is usually much smaller than the in-plane components and is, therefore, neglected [33]. The leading order term in this multipole expansion for the in-plane components of the force is a dipole term and, in the most general case, the traction $\mathbf{T}$ can be expressed in terms of a symmetric force dipole tensor $\mathbf{A}$ [9]:

$$\mathbf{T}_i = A_{ik} \frac{\partial}{\partial \mathbf{R}_k} \delta(\mathbf{R} - \mathbf{R}_0) \ , \tag{25}$$

where $i,k = 1,2$, are the coordinates in the surface (x and y). Here $\mathbf{R}$ is the radius-vector on the surface and $\mathbf{R}_0$ is the position of the adatom $(x_0,y_0,0)$.

Reproduced with permission of the copyright owner. Further reproduction prohibited without permission.

In the case of a (001) surface of a cubic solid, which exhibits a four-fold symmetry, the tensor $\mathbf{A}_{ik}$ is diagonal: $\mathbf{A}_{ik} = A\delta_{ik}$. Here, the traction vector can be written as follows:

$$\mathbf{T}_x = A\frac{\partial}{\partial x}\delta(\mathbf{R}-\mathbf{R}_0) \quad \text{and} \quad \mathbf{T}_y = A\frac{\partial}{\partial y}\delta(\mathbf{R}-\mathbf{R}_0) \ . \tag{26}$$

The energy of interaction between two adatoms E_{int} may be determined by a simple virtual work argument: i.e. this energy is the force (traction) due to one atom times the displacement field of the other:

$$E_{\text{int}} = \frac{1}{2}(\mathbf{T}^1\mathbf{u}^2 + \mathbf{T}^2\mathbf{u}^1) \ , \tag{27}$$

where $\mathbf{u}^i$ is the surface displacement that adatom i produces on the surface at the position of adatom j and $\mathbf{T}^j$ is the traction vector associated with adatom j. In the present case, the tractions are modeled as point sources, however, if the tractions are distributed over the surface, Eq. (27) would be replaced by an integral over the surface. Using the reciprocal theorem, we can rewrite Eq. (27) as:

$$E_{\text{int}} = \mathbf{T}^1\mathbf{u}^2 \ . \tag{28}$$

The displacement field $\mathbf{u}$ associated with an adatom can be determined by using its equivalent tractions and the elastic surface Green's function $\mathbf{G}$.

$$\mathbf{u}(x,y,z) = \int d\mathbf{R}'\, \mathbf{G}(\mathbf{R}-\mathbf{R}',z)\mathbf{T}(\mathbf{R}') \ . \tag{29}$$

Using this relation, the interaction energy between identical adatoms can be determined directly from Eq. (28):

$$\begin{aligned} E_{\text{int}} = A^2\Bigg(&\frac{\partial^2}{\partial x^2}\mathbf{G}_{xx}(\mathbf{R},z=0) + \frac{\partial^2}{\partial y^2}\mathbf{G}_{yy}(\mathbf{R},z=0) \\ &+ \frac{\partial^2}{\partial x\partial y}\mathbf{G}_{xy}(\mathbf{R},z=0) + \frac{\partial^2}{\partial y\partial x}\mathbf{G}_{yx}(\mathbf{R},z=0)\Bigg) \ . \end{aligned} \tag{30}$$

Reproduced with permission of the copyright owner. Further reproduction prohibited without permission.

Lau [34] determined the adatom interaction energy from Eq. (30) using the anisotropic elastic surface Green's functions obtained in [35,39]. These Green's functions provide a complete solution for the elastic field throughout the solid for a point force in the surface. However, in order to determine the interaction energy using Eq. (30), the only piece of information that is required is the displacement field in the surface created by a point force. The price associated with such an excess of information in the approach followed by Lau is the need to use the complicated Green's function expressions derived in [35,39]. More direct methods for finding the matrix **G** at $z = 0$ exist. Barnett and Lothe [40] proposed a direct method for evaluating $\mathbf{G}(\mathbf{R}, z = 0)$ by Fourier transforming the solution in the x-y plane, which reduces the problem to one of 2D elasticity, and solving the resultant equations using a Stroh-like [26] formalism. The resulting expression provides a natural separation of the matrix $\mathbf{G}(\mathbf{R}, z = 0)$ into symmetric and antisymmetric parts. Barber and Sturla [41] used the reciprocal theorem with the elastic field of a linear surface force dipole as an auxiliary solution to find the symmetric part of the matrix $\mathbf{G}(\mathbf{R}, z = 0)$. We follow the same approach and treat the displacement field of a linear surface dipole (i.e., a surface step, as described above) as an auxiliary solution.

We denote the matrix $\mathbf{G}(\mathbf{R}, z = 0)$ as $\mathbf{h}(\mathbf{R})$, following the notation in [41], where **R** is the vector from the adatom to some point on the surface ($z = 0$). In the isotropic case, the surface Green's function is well-known [24]. In the anisotropic case, $\mathbf{h}(\mathbf{R})$ has a complicated dependence on the direction within the $z = 0$ plane. Because of the self-similarity of the underlying elastic equations of equilibrium, $\mathbf{h}(\mathbf{R})$ can be factored as a product of its angular part $\mathbf{h}(\alpha)$ and its radial part, which is inversely proportional to the distance from the origin R:

$$\mathbf{h}(\mathbf{R}) = \frac{\mathbf{h}(\alpha)}{R} \quad , \tag{31}$$

where α is the angle the radius vector **R** makes with respect to the x-axis.

Reproduced with permission of the copyright owner. Further reproduction prohibited without permission.

For a{001} surface of a cubic material, with the x and y axes directed along the four-fold crystallographic directions of the material, the symmetric part of the $\mathbf{h}(\alpha)$ is:

$$\mathbf{h}(\alpha) = \frac{\mathbf{P}(\alpha - \pi/2)\mathbf{L}^{-1}(\alpha)\mathbf{P}^{\mathrm{T}}(\alpha - \pi/2)}{2\pi} \quad , \tag{32}$$

where

$$\mathbf{P} = \begin{pmatrix} \cos\alpha & -\sin\alpha & 0 \\ \sin\alpha & \cos\alpha & 0 \\ 0 & 0 & 1 \end{pmatrix} . \tag{33}$$

$\mathbf{P}$ is a matrix akin to the transformation matrix used in [35] and $\mathbf{L}(\alpha)$ is a 3x3 matrix that is a function of the three elastic constants of the cubic material which is required for the solution of the corresponding 2D elastic problem within the framework of the Stroh formalism. The expression for $\mathbf{L}(\alpha)$ is presented in Appendix 4A.

Equation (34) provides us with all of the ingredients necessary to determine the adatom interaction energy. Combining Eqs. (30)-(32) and performing some algebraic manipulations yields:

$$E_{\mathrm{int}} = \frac{A^2}{2\pi R^3}\left(1 + \frac{\mathrm{d}^2}{\mathrm{d}\alpha^2}\right)\left(\mathbf{L}(\alpha)^{-1}\right)_{11} \quad , \tag{34}$$

where $\mathbf{G}(\mathbf{R}, z = 0) = \mathbf{h}(\alpha)/R$, R is the separation between two adatoms and α is the direction from one adatom to the other with respect to one of the four-fold axes of the material. This result is consistent with that obtained by Lau [34] from the full Green's function of a cubic material. We recall that Eq. (34) is derived under the assumption that the interaction between the adatoms may be described in terms of the adatom dipole fields. In this approximation, the interaction energy between two adatoms decays as $1/R^3$, as required by the self-similarity of the elastic equilibrium equations. While the interaction energy determined from isotropic analysis (Eq. 24) is independent of angle, the angular dependence in the anisotropic solution can be very important; e.g., the sign of the interaction energy may change with the angle.

Reproduced with permission of the copyright owner. Further reproduction prohibited without permission.

The only unknown in Eq. (34) is the magnitude of the surface force dipole associated with the adatom, A. This parameter can not be determined from the elastic theory, since it requires detailed knowledge of the atomic interactions on a length scale of order an atomic size. In the following sections, we employ atomistic computer simulations to determine the magnitude of this parameter. We then compare the angular and spatial dependence of the predicted interaction energies with those obtained directly from the atomistic simulations.

Atomistic simulations

In this atomistic study we investigate the interaction of Ni adatoms on the {001} Ni surface. Because an adatom on a surface creates a long-range displacement field within the bulk of the solid, the simulation cell size must be sufficiently large as to not affect the interaction energy between two adatoms. In order to make this problem more computationally tractable, we impose periodic boundary conditions in two orthogonal directions within the plane of the surface. By so doing, we investigate the interactions between a periodic lattice of adatoms, rather than between a pair of adatoms. Since, within the approximation of linear elasticity, the elastic fields of the individual adatoms may be superimposed, we can analyze the interactions between the adatoms within the lattice as a sum of adatom-adatom interactions. The geometry of the computational cells employed in the present simulation is shown in Fig. 4.6. The simulation cell is a rectangular parallelepiped with axes parallel to the <001> directions of the underlying cubic crystal. A single adatom was placed upon the (001) surface. Periodic boundary conditions are applied in the x and y directions (parallel to two axes of the parallelepiped). In Fig 4.6, S_1 and S_2 represent the period of the lattice of adatoms that coincides with the size of the computational cell. We varied both the ratio S_1 to S_2 and the smallest period S_1.

Reproduced with permission of the copyright owner. Further reproduction prohibited without permission.

For the sake of consistency, the interactions between Ni atoms were modeled by the same set of EAM potentials as that used to model the interaction between [100] steps on (001) Ni surface [20]. The equilibrium configuration of the system was determined by minimizing the total energy (Eq. 34) with respect to the positions of all of the atoms. This minimization was performed using the conjugate gradient method as described above. In order to insure that the perfect crystal, to which the finite size simulation cell was matched at $z = h$, had no influence on the adatom-adatom interaction energies, h was increased until the interaction energies did not change to the desired precision.

Results and discussion

The angular dependence of the Green's function $\mathbf{h}_{zz}(\alpha)$ (Eq. 32) for EAM Ni is completely determined from its anisotropic elastic constants: C_{11} = 233 GPa (1.45 eV/Å^3), C_{11} = 154 GPa (0.96 eV/Å^3), C_{44} = 128 GPa (0.80 eV/Å^3) [20]. Figure 4.7 shows $\mathbf{h}_{zz}(\alpha)$ as a function of angle using the anisotropic elastic constants, as well as the effective (Voigt average) isotropic elastic constants of Ni. Comparison of the isotropic and anisotropic Green's functions shows that inclusion of anisotropy introduces an angular dependence to $\mathbf{h}_{zz}(\alpha)$ and increases the absolute magnitude of $\mathbf{h}_{zz}$ by 21%, on average. The four-fold symmetry of the underlying crystal lattice is obvious in $\mathbf{h}_{zz}(\alpha)$.

Although the anisotropic elastic Green's function $\mathbf{h}_{zz}(\alpha)$ shows a relatively small variation with angle, the adatom-adatom interaction energy (Eq. 34) shows a very strong variation with angle (see Fig. 4.8). In fact, the adatom-adatom interaction energy changes sign with α. These results were first obtained in [34]. The adatom-adatom interaction energy, determined from isotropic elasticity, shows no variation with α and is positive (repulsive) for like adatoms. The interaction energy determined from the anisotropic solution is attractive along the <100> directions and is of the same order of magnitude as (but opposite in sign to) that predicted using the isotropic elastic solution. In the < 110>

Reproduced with permission of the copyright owner. Further reproduction prohibited without permission.

directions, the adatom interactions are repulsive and exceed the isotropic elastic predictions by more than a factor of 3.5.

To analyze the simulation results, we need to generalize the adatom pair interaction energy of Eq. (34) for the case of a rectangular lattice of adatoms. The interaction energy per atom in the adatom lattice is

$$E_{\text{int}} = \frac{1}{2}\sum_i E_{\text{int}}(\mathbf{R}_i) = \frac{A^2}{2\pi}\sum_i \frac{\Xi(\alpha_i)}{\mathrm{R}_i^3} = \frac{A^2}{2\pi S_1^3}\sum_{m,n} \frac{\Xi(\alpha_i)}{(m^2 + n^2(S_2/S_1)^2)^{3/2}} = \frac{A^2\Sigma}{2\pi S_1^3}, \qquad (35)$$

where the sum extends over the entire lattice of adatoms excluding the origin and $\mathbf{R}_i$ and α_i are the radius vector from the origin to the i^{th} adatom and the angle that vector makes from the x-axis, respectively. m and n are the x and y indices of the i^{th} atom in the lattice and S_1 and S_2 are the lattice periods, were S_1 is arbitrarily chosen as the shorter of the two (x and y) periods. The symbol Σ is defined within Eq. (35) and is a function of the ratio of the two periods S_1/S_2 and the elastic constants of the material. $\Xi(\alpha_i)$ is the angular part of the adatom interaction energy in Eq. (34):

$$\Xi(\alpha) = \frac{1}{2}\left(1 + \frac{\mathrm{d}^2}{\mathrm{d}\alpha^2}\right)\left(\mathbf{L}(\alpha)^{-1}\right)_{11}. \qquad (36)$$

The summation Σ was evaluated numerically with the elastic constants of EAM Ni and the orientation of the adatom lattice and crystal surface examined in the simulations; the results are shown in the Table 4.4. When $S_2{:}S_1 = 2{:}1$ and 3:1, the summation Σ is negative, while for $S_2{:}S_1 = 1{:}1$ Σ is positive. This implies that the overall interaction between adatoms in these lattices is attractive. We also calculated Σ for a $S_2{:}S_1 = 1{:}1$ lattice of adatoms on an *isotropic* substrate. This was done by generalizing Eq. (24) for the case of the adatom lattice in the same manner as we generalized Eq. (34). For the elastic constants which enter Eq. (24), we employed the Voigt average elastic constants of EAM Ni. While the values of Σ determined using the isotropic expression has the same sign as does that obtained using the anisotropic expression for $S_2{:}S_1 = 1{:}1$, the isotropic

Reproduced with permission of the copyright owner. Further reproduction prohibited without permission.

value is more than twice as large as the anisotropic one. We note that for S_2:S_1 = 2:1 and 3:1, the anisotropic value of Σ is negative, while the isotropic theory erroneously predicts that Σ is positive for all S_2:S_1.

Table 4.4

S_2:S_1	Σ
1:1	2.57
2:1	-0.37
3:1	-1.08
1:1 (isotropic)	5.63

Table 4.4. The magnitude of the lattice summation Σ (Eq. 35) for different adatom lattice period ratios S_2:S_1. Σ corresponds to t he overall interactions between all of the adatoms in the adatom lattice.

In the atomistic simulations of adatom-adatom interactions, we determine the total energy for one unit cell of the adatom lattice as a function of the adatom spacings S_1 and S_2. The total energy per cell consists of four terms:

$$E_{tot} = E_{bulk} + E_{surf} + E_{ad} + E_{int}^{ad} \quad . \tag{37}$$

The first term E_{bulk} corresponds to the bulk energy, which is the product of the energy of an atom in a perfect crystal and the number of atoms in the computational cell. The surface energy E_{surf} is the energy per unit area of the surface times the product of S_1 and S_2. The third term E_{ad} is the difference in energy between an infinite surface with and without a single adatom. Finally, the adatom interaction energy E_{int}^{ad} corresponds to the interaction between one adatom and all other adatoms in the adatom lattice, as per Eq. (35). E_{bulk} is simply the sublimation energy of Ni, which is an input parameter used to determine the EAM potential used in these studies. The surface energy was determined

Reproduced with permission of the copyright owner. Further reproduction prohibited without permission.

using the same interatomic potential, as described in Ref. [20]. E_{ad} was determined by extrapolating a plot of $E_{tot} - E_{bulk} - E_{surf}$ to large values of inter-adatom spacings, since the interaction energy between adatoms rapidly decays at large adatom separations.

The variation of the adatom interaction energy for a lattice of adatoms vs. the inverse lattice period S_1 is presented in Fig. 4.9 for S_2:S_1 = 1:1, 2:1 and 3:1. As expected, based upon the data in Table 4.4, the interaction energy is positive for S_2:S_1 = 1:1 and negative for S_2:S_1 = 3:1. For S_2:S_1 = 2:1, the magnitude of the interaction energy is very small (see Table 4.4). More interestingly, however, we find that for large S_1 the interaction energy is negative, while at small S_1 the interaction energy is positive. This is somewhat surprising, since Eq. (35) suggests that the interaction energy is a monotonic function of the adatom lattice spacing S_1. We note that the predicted variation of the interaction energy with adatom spacing is based upon a dipole model of the interaction energy which must be valid for large adatom-adatom spacing. This is verified by the data in Fig. 4.9, which shows that for S_2:S_1 = 2:1, the interaction energy is negative, in agreement with the predictions of the dipole theory in Table 4.4. When the adatoms are close together, higher order (than dipole) terms in the expansion of the surface force distribution clearly become important.

The next higher order (beyond dipole) term in the expansion of the surface force distribution associated with an adatom corresponds to quadropoles. Therefore, the next order term in the adatom interaction energy should correspond to dipole-quadropole interactions, which decay with adatom separation as S^{-4} [27]. In order to test this assertion, we fit the data in Fig. 4.9 to the following functional form:

$$E_{int} = \frac{B_3}{S_1^3} + \frac{B_4}{S_1^4} \quad , \tag{38}$$

where B_3 and B_4 are adjustable parameters. The results of the fit are presented in Table 4.5. The fourth-order term B_4 makes more than a 20% correction to the dipole model interaction energy for $S_1 < 14\,a_0$, $29\,a_0$ and $12\,a_0$ for S_2:S_1 = 1:1, 2:1 and 3:1,

Reproduced with permission of the copyright owner. Further reproduction prohibited without permission.

respectively. Therefore, for the range of data shown in Fig. 4.9, the dipole-quadropole (B_4) term is significant for all S_2:S_1 and is particularly significant for the 2:1 over most of the range of Fig. 4.9. The fact that the interaction energy changes sign with adatom spacing in the S_2:S_1 = 2:1 case, may be explained by noting that the dipole-quadropole term B_4 makes a significant contribution to the interaction energy and B_3 and B_4 have opposite sign. This implies that dipole-quadropole terms will be very important for determining the sign and magnitude of the elastic interaction between adatoms when the dipole-dipole terms in the interaction energy are small.

Table 4.5

	B_3 (eV Å^3)	B_4 (eV Å^4)
1:1	0.34	3.34
2:1	-0.077	1.56
3:1	-0.15	1.27

Table 4.5. The parameters describing adatom-adatom interactions on a (100) surface of EAM Ni, obtained by fitting the data in Fig. 4.9 to the functional form in Eq. (38).

Using Eq. (35) and the fitting parameter B_3 determined from the simulations and Eq. (38), we can extract the magnitude of the force dipole A

$$A = \sqrt{\frac{2\pi B_3}{\Sigma}} \,. \tag{39}$$

The values of A determined for each S_2:S_1 are reported in Table 4.6. Although B_3 varies by over 400% with S_2:S_1, the resulting force dipoles magnitudes A are within 20% of each other. The maximum deviation in A occurs for S_2:S_1 = 2:1, where the overall magnitude of the adatom interactions are very small (see Fig. 4.9). For the sake of comparison with the isotropic theory, we determined A for the isotropic elastic case

Reproduced with permission of the copyright owner. Further reproduction prohibited without permission.

(Table 4.6). The isotropic theory produces a force dipoles magnitude A, which is approximately 50% smaller than that predicted from the anisotropic elastic theory.

Table 4.6

S_2:S_1	A (eV)
1:1	0.91
2:1	1.15
3:1	0.93
1:1 (isotropic)	0.62

Table 4.6. The magnitude of the point force dipole strength A as per Eq. (39).

The present results demonstrate that elastic anisotropy is very significant in determining the magnitude, as well as the sign, of the elastic interaction between adatoms. Therefore, while the functional dependence of the interaction energy on adatom spacing may be determined using the isotropic elastic theory, the isotropic theory is unreliable for quantitative predictions.

Equation (39) gives only the absolute value of the force dipole A. Its sign (i.e., whether the dipole exerts a compressive or a tensile stress on the surface) was determined by analyzing surface atomic displacements in the vicinity of the adatom. Displacements of atoms closest to the center of the defect are directed outwards (corresponding to compression at the surface), leading us to assign a negative value to the force dipole strength.

4.4 Adatom-step interactions

Interactions between adsorbed atoms as well as interactions with other types of defects on metallic surfaces have been studied widely, because of the importance of this

Reproduced with permission of the copyright owner. Further reproduction prohibited without permission.

problem for the understanding of epitaxial crystal growth and surface morphology evolution processes (see the previous section of this chapter and [32]). Recently developed microscopy techniques have made it possible to make direct observations of interacting adatoms and surface steps [42]. It has long been known that the presence of a step creates a diffusion barrier (so-called Shwoebel barrier) which prevents adatoms from migrating from an upper terrace to a lower terrace, across a step [43]. This phenomenon, as well as adatom diffusion along the step, has been studied using atomistic static relaxation [44] and molecular dynamics [45] simulation methods, as well as by analyzing experimentally observed distribution of adatoms near the edge of an individual step [46]. However, despite a prolonged interest, the fundamental nature of these interactions is still not fully understood.

In the present section, we examine the long range elastic interactions between adatoms and steps on a surface using both atomistic computer simulation and elastic theory. Sections 4.2 and 4.3 which discuss elasticity of both adatoms and surface steps provide the necessary machinery to describe adatom-step interactions within the framework of the dipole model. Our main objective is to determine the appropriateness of the dipole elastic model for describing the adatom-step interaction at large separation and to parameterize the elastic model using results from the atomistic simulation.

In particular, we examine the elastic interaction of a Ni adatom with an [001] step on a (100) Ni surface. We perform a series of atomistic simulations in which we vary the adatom-step separation in order to determine the adatom-step interaction energy. Next, we conduct an elastic analysis to derive the expression of step-adatom interaction energy within the framework of the dipole model. The magnitude of the linear force dipole **D** associated with a step as well as the magnitude of an adatom force dipole A obtained in Sec. 4.2 and 4.3 serves an input for the model to obtain the numerical value of the step adatom interaction energy within the dipole approximation. Combining the results of

Reproduced with permission of the copyright owner. Further reproduction prohibited without permission.

these studies, we make a critical comparison of the atomistic and continuum elastic results.

Simulation method

We performed a series of atomistic simulations of a periodic array of adatoms on a vicinal surface consisting of [001] monoatomic height steps and (001) terraces. Several simulations were performed as a function of step - nearest adatom spacings, d_0, for the geometry shown in Fig. 4.10. In particular, we examined $4\,a_0 \leq d_0 \leq 9.5\,a_0$ for adatom separations of $15\,a_0$ in the direction parallel to the steps and b in the direction perpendicular to the steps. The step separation was also fixed at $b = 50\,a_0$. In all cases, the separation between adatoms and between adatoms and non-nearest steps are assumed to be sufficiently large such that their mutual interactions are predominantly elastic in nature. In practice, all of the periodicities are imposed by the application of periodic boundary conditions in the 0X and 0Y directions.

The interatomic interactions were modeled by the potentials [19] used to describe the interactions between Ni adatoms and [100] monoatomic steps on the (001) Ni surface. This descriptions of atomic interactions is consistent with those used in Sec. 4.2, 4.3.

The equilibrium configuration of the system was determined by minimizing the total energy of the system with respect to the positions of all of the atoms using the conjugate gradient method [21] as described above. In order to insure that the perfect crystal to which the finite size simulation cell was matched at $z = h$ had no influence on the adatom-adatom interaction energies, h was fixed at the depth of $12.5\,a_0$ which is greater than the largest step-adatom spacing examined.

Due to the extremely large number of atoms in the computational cell, the accuracy in the energy minimization procedure was decreased to the relative error in the total energy of 10^{-5} compared to 10^{-7} in the simulations of interacting steps and adatoms.

Reproduced with permission of the copyright owner. Further reproduction prohibited without permission.

This reduction in the severity of the convergence criterion allowed us to reduce the computational time required for the energy minimization procedure without which the present problem would be intractable.

Elastic analysis and results

The energy associated with the interaction between a surface step and an adatom can be readily determined using the simple virtual work argument (Eq. (27)). The expression for the interaction energy is:

$$E_{int}^{ad-st} = \frac{1}{2}\left(\mathbf{T}_{adat}\mathbf{u}_{step} + \mathbf{T}_{step}\mathbf{u}_{adat}\right) , \tag{40}$$

where $\mathbf{T}_{step}$ and $\mathbf{T}_{adat}$ are the vectors of tractions that a step and an adatom exert on the material surface and $\mathbf{u}_{step}$ and $\mathbf{u}_{adat}$ are corresponding displacement vectors evaluated at the surface at the position of the other defect. The product must be replaced by a convolution integral in case of distributed surface tractions, as explained above. It is convenient to rewrite Eq. (40) using the reciprocal theorem as:

$$E_{int}^{ad-st} = \mathbf{T}_{adat}\mathbf{u}_{step} . \tag{41}$$

The elastic field of a step on the surface of an isotropic medium is well known and is described in detail in [18]. The in-plane and out-of-plane components of the displacement vector are decoupled at the surface, i.e. the out-of-plane component of the force dipole **D** creates no in-plane component of the vector $\mathbf{u}_{step}$ and vice versa. Since the out-of-plane component of the surface tractions associated with the adatom are higher order than dipole, we neglect them. Therefore, we need only consider the in-plane component of the displacement field of the step in Eq. (41). The dependence of E_{int} on the distance between a step and an adatom d_0 is obtained by replacing the dipole tractions associated with the adatom with its representation as a derivative of a delta function (see Eq. (26)):

Reproduced with permission of the copyright owner. Further reproduction prohibited without permission.

$$E_{int}^{ad\text{-}st} = \frac{2(1-\nu^2)}{\pi E}\frac{D_x A}{d_0^2} \quad . \tag{42}$$

where E and ν and the Young's modulus and Poisson's ratio of the material.

Whether this interaction is repulsive or attractive is determined by the signs of both A and D_x. Both these quantities are determined microscopically; i.e., in terms of the local atomic interactions in the core of each defect. The interaction energy within the linear elastic and dipole approximations is symmetric with respect to whether the adatom is on the upper or lower terrace (to the left or right of the step) in Fig. 4.10. This is because the in and out-of-plane components of the step force dipole and its displacement field are decoupled in this approximation.

The interaction energy between surface defects, which are each described in terms of a multipole (derivatives of a delta function), is inversely proportional to some power of their separation d_0 [27]. Increasing the number of terms one uses in the multipole expansion of the defect surface traction adds additional terms in the defect interaction energy which are of higher order (i.e., higher powers of the inverse defect separation $1/d_0$). In the cases of step-adatom interactions considered here, the leading order term in the expansion of the surface tractions is of second order (i.e., dipole). Therefore, the leading order term (i.e., smallest power of $1/d_0$) in the surface defect-defect interactions will always be a associated with dipole - dipole interactions. This effectively prohibits the appearance of a term linear in $1/d_0$ in the expression for the interaction energy (Eq. (42)). This same conclusion holds in the anisotropic elasticity case as well, since the self-similarity of the displacement field created by a surface multipole is a consequence of the homogeneity of the underlying elastic equation of equilibrium [39].

Anisotropic elastic analysis of the displacement field of a [100] step on the (001) surface performed in Sec. 4.2 (Eqs. (10)-(14)) allows us to consistently replace the isotropic result for the interaction energy (Eq. (42)) with the anisotropic one. Similarly to

Reproduced with permission of the copyright owner. Further reproduction prohibited without permission.

the isotropic material case, for this step geometry, the in-plane the in and out-of plane components of the step surface force dipole **D** and the displacement vector **u** are decoupled at the free surface. The expression for the in-plane component of the displacement vector at the surface is:

$$\mathbf{u}_x^{step} = -\mathbf{D}_x / (\pi L d_0) \tag{43}$$

where $\mathbf{D}_x$ is the magnitude of the in-plane component of the step force dipole, d_0 is the distance from the step, and L is given by Eq. (15c). Its numerical value for the [100] step on the (001) surface of EAM nickel is 0.627 eV/Å^3. For a step of this orientation, the anisotropic elastic correction to the adatom/step interaction, Eq. (42) becomes:

$$E_{int}^{ad\text{-}st} = \frac{1}{\pi L}\frac{\mathbf{D}_x A}{d_0^2} \quad . \tag{44}$$

The magnitude of the in-plane component of the step force dipole $\mathbf{D}_x$ is equal to -0.15 eV/Å. (The sign of $\mathbf{D}_x$ is changed compared to Table 4.2 to account for the handedness of the coordinate system). Combining this result with the magnitude of the surface dipole strength associated with the adatom and Eq. (44), yields the adatom-step interaction energy with no adjustable parameters. Therefore, we can use this result to directly analyze the adatom/step interactions found in the atomistic computer simulations. Using the independently determined defect strengths ($A < 0$ and $\mathbf{D}_x < 0$), the step/adatom interactions (Eq. 44) are repulsive and are symmetric with respect to the position of an adatom about the step. Corrections to Eq. (44) may result from terms higher than dipole in the expansion of the surface tractions simulating either and/or both of the defects. These corrections will be terms including cubic and higher powers of the reciprocal distance d_0 between a step and an adatom.

The presence of the periodic boundary conditions in the atomistic simulations prevents us from directly applying Eq. (44) to the simulation data. Fortunately, we can

Reproduced with permission of the copyright owner. Further reproduction prohibited without permission.

rederive Eq. (44) for the case of an adatom interacting with a periodic array of steps results

$$E_{int}^{ad\text{-}st} = \frac{\pi^2}{b^2 \sin^2(\pi d_0 / b)} \frac{\mathbf{D}_x A}{\pi L} , \tag{45}$$

where b is the step spacing in the computational cell. The next higher-order term in the expansion of the step/adatom interaction will transform into a term proportional to:

$$\frac{\pi^3 \cos(\pi d_0 / b)}{b^3 \sin^3(\pi d_0 / b)} .$$

The results of the simulations for both the upper and the lower terraces of the step were fitted to the functional form:

$$E_{int}^{ad\text{-}st} = B_1 \frac{\pi^2}{b^2 \sin^2(\pi d_0 / b)} + B_2 \frac{\pi^3 \cos(\pi d_0 / b)}{b^3 \sin^3(\pi d_0 / b)} \tag{46}$$

where B_1 and B_2 are fitting constants. There is an uncertainty of order of the size of the core of the step, as to which point corresponds to the appropriate origin of the coordinate system. For the sake of simplicity, we measured d_0 from the adatom position to the step along the terrace. In other words, for adatoms on the upper terrace, d_0 is measured to the top of the step and on the lower terrace, d_0 is measured to the bottom of the step.

The dependence of the step-adatom interaction energy on step-adatom separation d_0 for adatoms on both the upper and lower terraces, obtained from the atomistic simulations, is shown in Fig. 4.11. Over the range of step-adatom separations considered here ($4\ a_0 \le d_0 \le 9.5\ a_0$) with a step separation fixed at $b = 50\ a_0$, the step-adatom interaction energy decays monotonically. This figure also shows that there is a difference between the step-adatom interaction energies for adatoms on the upper and lower terraces. This difference is largest at small separations and becomes negligible (within the numerical error) at large separations. At small separations, the adatom-step repulsion is larger on the upper terrace.

Reproduced with permission of the copyright owner. Further reproduction prohibited without permission.

Table 4.7 shows the results of the determination of the parameters B_1 and B_2 in Eq. (46) by fitting to the simulation data in Fig. 4.11. The values of the dipole-dipole coefficient B_1, determined from the simulation data for the upper and lower terraces, are in good agreement (i.e., $B_1 = 112 \pm 13\%$). On the other hand, the values corresponding to the dipole-quadropole coefficient B_2 differ by approximately 300% and are both attractive (negative). This deviation can also be seen in Fig. 4.11, where the two curves representing the upper and lower terraces deviate from each other in regions of small step-adatom separation. The large differences in the third order term in the expansion of the step-adatom interaction (Eq. 45) are due, in part, to the antisymmetry of the out-of-plane (vertical) component of the displacement field of the step. This antisymmetry only enters the dipole-quadropole and higher order terms since the leading order term in the out-of-plane surface force of the adatom is quadropolar while that of the step is dipolar. Normally, we would expect that these terms would lead to opposite signs of B_2 on the upper and lower terraces. However, there are also other dipole-quadropole terms present associated with higher moments of the in-plane force distribution and the non-point-like spatial distribution of those force distributions. In the range of separations presented in Fig. 4.11, the contribution to the interaction energy of these third-order terms is approximately 5% for the upper terrace and 20% for the lower terrace.

Figure 4.11 also shows a comparison of the step-adatom interaction energies determined from the simulations with those predicted by the elastic theory (where we have independently determined all of the parameters). The predicted step-adatom interaction energy and those from the simulations show very nearly the same separation (d_0) dependence. This suggests that the dipole surface force model for step-adatom interactions is valid. However, the simulation results are shifted to higher step-adatom interaction energies as compared with the theoretical predictions by approximately 40%. We believe that the error here is primarily caused by three factors. Due to the very large number of atoms in the computational cell, the accuracy of the total energy minimization

Reproduced with permission of the copyright owner. Further reproduction prohibited without permission.

procedure in the computations of energy associated with the interactions between a step and an adatom is lower than that achieved in the computation of the step-step and adatom-adatom interaction energies. Because the convergence criterion employed in the

Table 4.7

	B_1(meV Å^2)	B_2(meV Å^3)	χ^2
elastic theory	76.2		
Upper	99.3	-109.9	3.65×10^{-5}
Lower	124.5	-837.4	5.89×10^{-5}

Table 4.7. The parameters describing the interactions between a [100] step on a (100) surface and an adatom. These parameters were obtained by fitting the data in Fig. 4.11 to the functional form in Eq. (46). The data point labeled elastic theory was obtained from Eq. (45) using the dipole strengths determined from simulations based on isolated defects.

present calculation was relaxed, the atomic displacement fields are not fully equilibrated. As a result, the actual interaction energy may be lower than that found here; resulting in a somewhat smaller coefficient B_2 in Eq. (46).

Another possible source of error is related to the choice of the origin from which the adatom - step distance is measured. In the present study we arbitrarily chose two separate origins, one used for an adatom on the upper terrace and one for an adatom on the lower terrace. The uncertainty in the choice of origin is of the order of a_0. Over the range of the adatom-step separations d_0 examined in the present atomistic simulations, this uncertainty may result in an error in the fitting coefficient B_2 of order of $(a_0/d_0)^2$, i.e., about 10 - 20%. This value is in the same range as the discrepancy between the values of the coefficient B_2 for the upper and lower terrace as well as the value computed in accordance with the predictions of the dipole model and linear elasticity (Eq. (45)).

Reproduced with permission of the copyright owner. Further reproduction prohibited without permission.

Finally, the discrepancy between the simulations and the theoretical predictions may be caused by the contribution of the short – range forces into the interaction energy. In Sec. 4.2 we estimated the size of the core of the step as approximately 5 lattice parameters. A similar estimation was not conducted for adatoms due to difficulties associated with distinguishing between short range forces and higher-order multipole terms due to the anisotropy of adatom - adatom interactions. Nevertheless, it is reasonable to assume that the range over which the elastic dipole model is inappropriate for describing adatom-adatom interactions does not extend beyond a few atomic spacings. Both these two estimates are comparable with the smallest adatom - step separations for which atomistic simulations were conducted. Hence, we expect the dipole model to provide a relatively inaccurate prediction of the interaction energy in the present range of adatom-step separations.

4.5 Conclusions

In this Chapter, we employed anisotropic elastic analysis and computer simulations to study the nature of interactions between surface defects (surface steps and adatoms). The displacement field of and interaction energies between [100] steps on a (001) surface of Ni and Au were determined using zero temperature atomistic simulations and Embedded Atom Method (EAM) interatomic potentials. A fit of the step-step interaction energy determined from simulations shows that the leading order term in the step-step interaction energy is proportional to the inverse square of the step spacing. This is consistent with a surface line force dipole elastic model of a step. In order to fit the simulation data to the elastic model, we derived an anisotropic form for the elastic field associated with a surface line force dipole. One input into the analytical description of the elastic fields of the step is the surface force dipole vector associated with the step. We determined this dipole vector by fitting the displacement field determined from the

Reproduced with permission of the copyright owner. Further reproduction prohibited without permission.

simulation with the results of the anisotropic elastic theory. We demonstrated that this fit is excellent for both Ni and Au. This dipole vector was combined with the anisotropic elastic theory to predict the step-step interaction energy. This too was shown to be in excellent agreement with the simulations.

Next, we studied the interactions between homoepitaxial adatoms on a substrate. Point dipole forces were used to model the elastic fields generated by adatoms on a surface. The anisotropic elastic theory showed that the adatom-adatom interaction energy has a strong angular dependence and can change sign with angle. Atomistic simulations were used to test the validity of the anisotropic elastic theory and to determine the overall magnitude of the dipole force, which was needed to fully parameterize the elastic theory. These simulations were performed for Ni adatoms on a {001} Ni substrate using the same set of the EAM interatomic potentials. The simulations were shown to be in very good agreement with the anisotropic elastic theory prediction. However, when the spacing between adatoms was small, dipole-quadropole interaction terms became important, especially in directions in which the dipole-dipole interactions are very small. The magnitudes of the force dipole, determined from simulations that emphasize different crystallographic directions, were all nearly identical. This further supports the anisotropic dipole-dipole interaction model for adatom interactions on solid surfaces.

Finally, we derived an analytical expression for the energy associated with the step-adatom interactions in the framework of linear elasticity. This theory requires two parameters: the strength of the elastic fields associated with the adatoms and those associated with the steps, which are readily available from the atomistic simulations of step-step and adatom-adatom interactions on Ni {001} surface. These defect strengths were used to predict the elastic interaction energy between a Ni adatom and a <001> step on the same surface. Atomistic simulations of a surface with a periodic array of steps interacting with an adatom were performed and compared with the predictions of the elastic theory with no adjustable parameters. A detailed comparison of the simulation and

Reproduced with permission of the copyright owner. Further reproduction prohibited without permission.

theoretical result showed that the step-adatom interactions were dominated by dipole-dipole interactions, but that higher order terms can also be significant in the range of adatom-step separation studied here. We also discussed a possible source of discrepancies between the numerical values of the interaction energies which were obtained from theoretical predictions and atomistic simulations.

Reproduced with permission of the copyright owner. Further reproduction prohibited without permission.

References to Chapter IV

[1] T. L. Einstein, in *Handbook of Surface Science*, ed. by W. N. Unertl, (Elsevier Science B. V.: Amsterdam, 1996) Vol. 1 (Physical Structure).

[2] W. Kohn and K. H. Lau, *Solid State Comm.*, **18**, 553 (1976).

[3] J. P. Hirth and J. Lothe, *Theory of Dislocations*, (Wiley: New York, 1982).

[4] C. Herring, in *The Physics of Powder Metallurgy*, ed. by W. E. Kingston, (McGraw-Hill: New York, 1951).

[5] R. Shuttleworth, *Proc. Royal Soc.*, **A63**, 445 (1950).

[6] R. C. Cammarata, *Prog. Surf. Sci.*, **46**, 1 (1994).

[7] V. I. Marchenko, *JETP Lett.*, **33**, 381 (1981).

[8] Z. Suo and W. Lu, *J. Mech. Phys. Solids*, (To be published).

[9] V. I. Marchenko and A. Ya. Parshin, *Sov. Phys. JETP*, **52**, 129 (1980).

[10] D. J. Srolovitz and J. P. Hirth, Surf. Sci. **255**, 111 (1991).

[11] V. I. Marchenko, *Sov. Phys. JETP* **54**, 605 (1981).

[12] P. Wynblatt, in *Interatomic potentials and simulation of lattice defects*, ed. by P. Gehlen, J. R. Beeler, and R. I. Jaffee, (Plenum Press: New York, 1972).

[13] D. Wolf and J. A. Jaszczak, *Surf. Sci.*, **277**, 301 (1992).

[14] A. C. Redfield and A. Zangwill, *Phys. Rev.*, **B46**, 4289 (1992).

[15] R. Najafabadi and D. J. Srolovitz, *Surf. Sci.*, **317**, 221 (1994).

[16] B. Houchmandzadeh and C. Misbah, *J. Phys. I (Paris)*, **5**, 685 (1995).

[17] O. Pohland, X. Tong, and J. M. Gibson, *J. Vac. Sci. Tech.*, **A11**, 1837 (1993).

[18] J. Stewart, O. Pohland, and J. M. Gibson, *Phys. Rev.*, **B49**, 13848 (1994).

[19] M. S. Daw and M. I. Baskes, *Phys. Rev.*, **B29**, 6443 (1984).

[20] S. M. Foiles, M. L. Baskes, and M. S. Daw, *Phys. Rev.* **B33**, 7983 (1986).

[21] W. H. Press and *et al*, *Numerical Recipes in C: The Art Of Scientific Computing*, 2nd ed., (Cambridge University Press: New York, 1992).

Reproduced with permission of the copyright owner. Further reproduction prohibited without permission.

[22] G. J. Ackland and M. W. Finnis, *Phil. Mag.*, **A54**, 301 (1986).

[23] For example, see Ref. [18].

[24] L. D. Landau and E. M. Lifshitz, *Theory of Elasticity*, 3rd ed., (Pergamon Press: Oxford, 1986).

[25] I. M. Lifshitz and L. N. Rozentsveig, *Zh. Eksp. Teor. Fiz.*, **17**, 783 (1947).

[26] A. N. Stroh, *Phil. Mag.*, **3**, 625 (1958).

[27] J. M. Rickman and D. J. Srolovitz, *Surf. Sci.*, **284**, 21 (1993).

[28] W. R. Tyson and W. A. Miller, *Surf. Sci.*, **62**, 267 (1977).

[29] J. Tersoff, A. W. D. v. d. Fon, and R. M. Tromp, *Phys. Rev. Lett.*, **72**, 266 (1994).

[30] J. A. Venables, G. D. T. Spiller, and M. Hanbucken, *Rep. Prog. Phys.*, **47**, 399 (1984).

[31] A. M. Stoneham, *Solid State Comm.*, **24**, 425 (1977).

[32] C. Duport, P. Ploliti, and J. Villiain, *J. Phys. I (Paris)*, **5**, 1317 (1995).

[33] K. H. Lau and W. Kohn, *Surf. Sci.*, **65**, 607 (1977).

[34] K. H. Lau, *Solid State Commun.*, **28**, 757 (1978).

[35] K. Portz and A. A. Maradudin, *Phys. Rev.*, **B16**, 3535 (1977).

[36] W. Kappus, *Z. Phys.*, **B45**, 113 (1981) and references therein.

[37] F. Watanabe and G. Ehrlich, *J. Chem. Phys.*, **96**, 3191 (1992).

[38] C. Teodosiu, *Elastic models of crystal defects*, (Springer-Verlag: Berlin, 1982).

[39] L. Dobrzynski and A. A. Maradudin, *Phys. Rev.*, **B14**, 2200 (1976).

[40] D. M. Barnett and J. Lothe, *Phys. Norv.*, **8**, 13 (1975).

[41] J. R. Barber and F. A. Sturla, *J. Mech. Phys. Solids*, **40**, 17 (1992).

[42] G. Ehrlich, *Surf. Sci.*, **241**, 1 (1991).

[43] R. L. Schwoebel and E. J. Shipsey, *J. Appl. Phys.*, **37**, 3682 (1966).

[44] C. L. Liu, *Intl. J. Mod. Phys.*, **B9**, 1 (1995).

[45] C. Uebing, *Phys. Rev.*, **B49**, 13913 (1994).

Reproduced with permission of the copyright owner. Further reproduction prohibited without permission.

[46] S. C. Wang and G. Ehrlich, *Phys. Rev. Lett.*, **71**, 4174 (1993).

[47] T. C. T. Ting, *Q. J. Mech. Appl. Math.*, **45**, 119 (1992).

Reproduced with permission of the copyright owner. Further reproduction prohibited without permission.

Fig. 4.1a

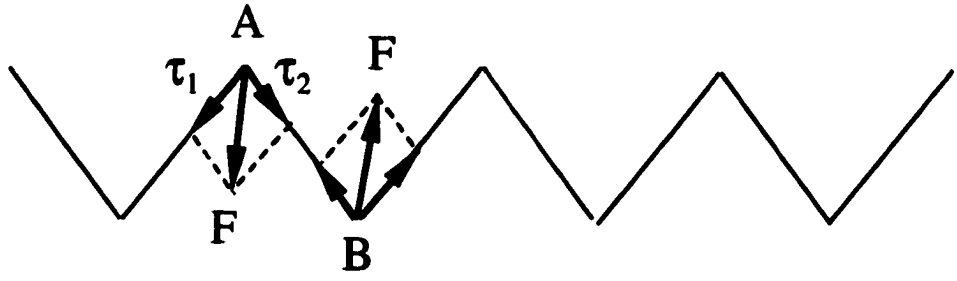


Fig. 4.1b

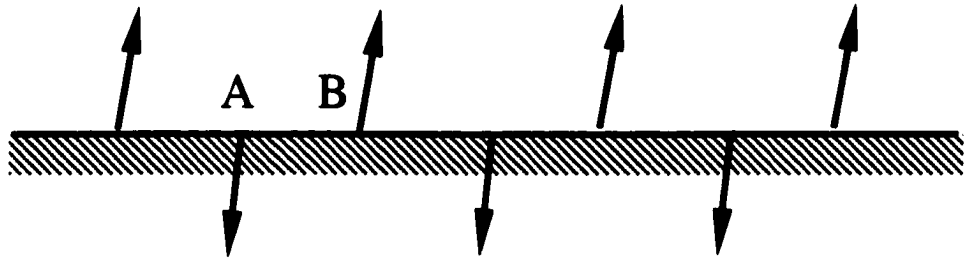


Fig. 4.1c

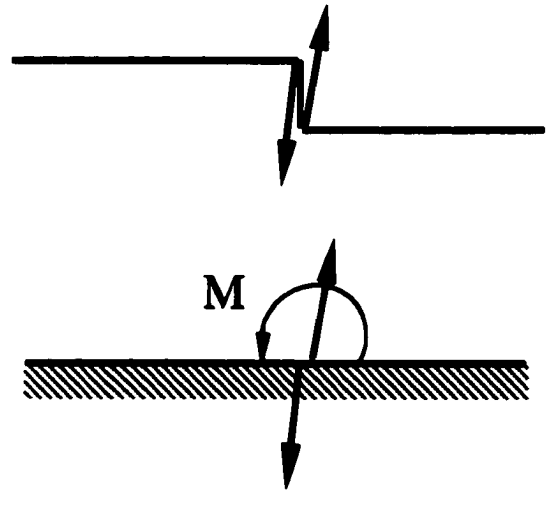


Figure 4.1. Surface tractions produced by discontinuities in the surface stress on a faceted surface. a) A force created by a facet. The surface stresses on the two inequivalent facets are τ_1 and τ_2. b) Approximation of a faceted surface by an array of alternating forces on a flat solid surface c) A step with the tractions which form a force couple is replaced by a tilted surface force dipole. The out-of-plane (vertical) component of this dipole compensates the moment M created by the force couple.

Reproduced with permission of the copyright owner. Further reproduction prohibited without permission.

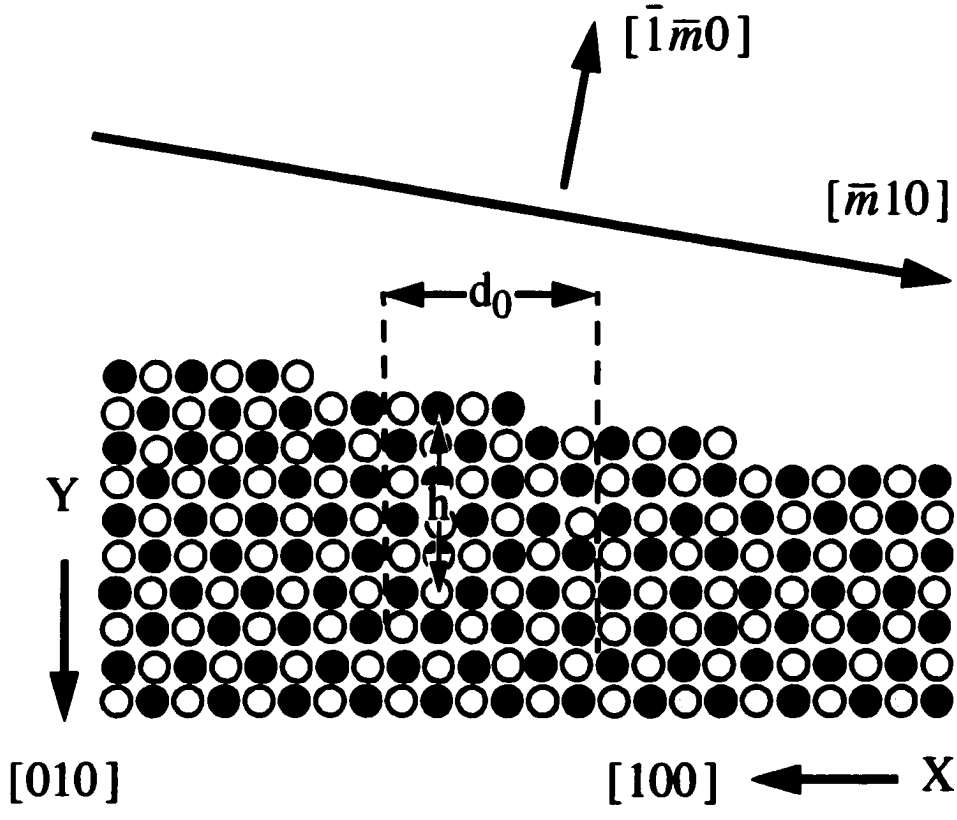
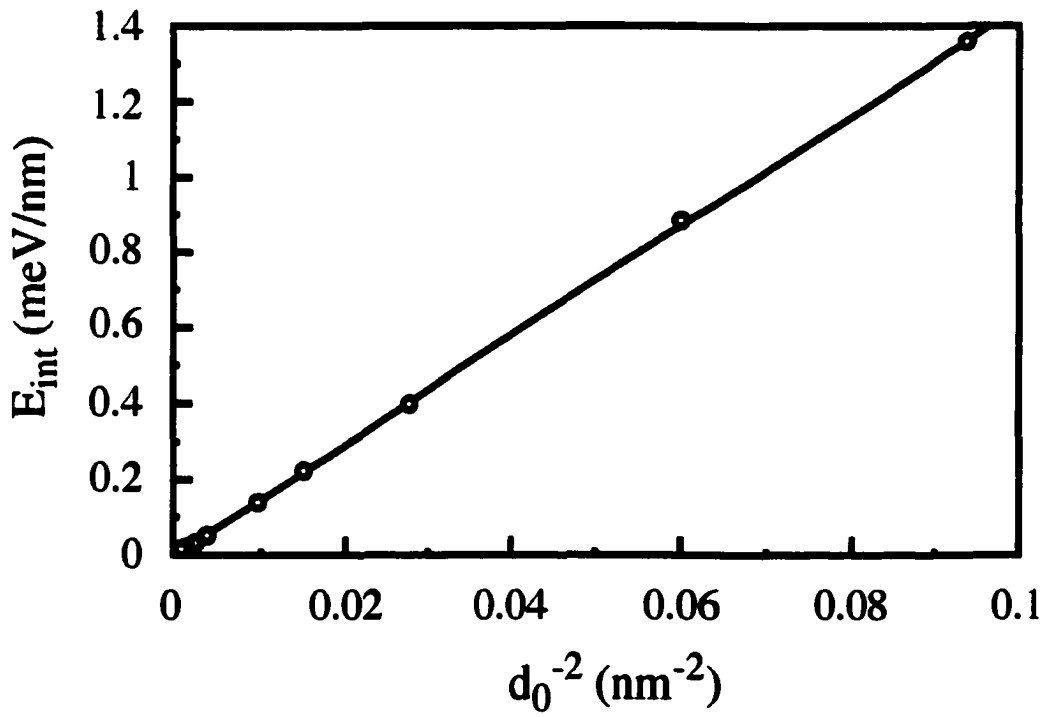


Figure 4.2. The geometry of the simulation cell. Black and white circles denote atoms displaced in the Z-direction by $a_0/2$, where a_0 is the perfect crystal lattice constant. This figure corresponds to a $(\bar{1}\bar{6}0)$ surface. d_0 is the step separation and $b = a_0/2$ is the step height. The unit cell width is equal to the step separation, its height is h and its thickness is a_0. Periodic boundary conditions are applied in the [$\bar{m}$10] direction and the atoms at $Y > h$ are frozen in their perfect crystal positions.

Reproduced with permission of the copyright owner. Further reproduction prohibited without permission.

Fig. 4.3a



Reproduced with permission of the copyright owner. Further reproduction prohibited without permission.

Fig. 4.3b

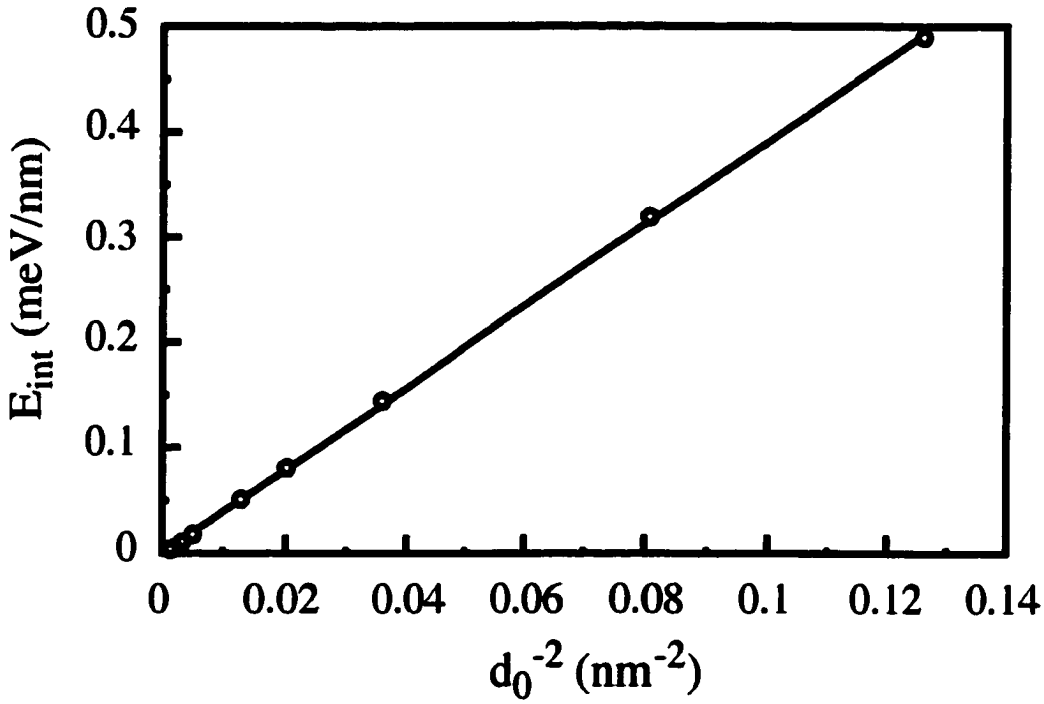
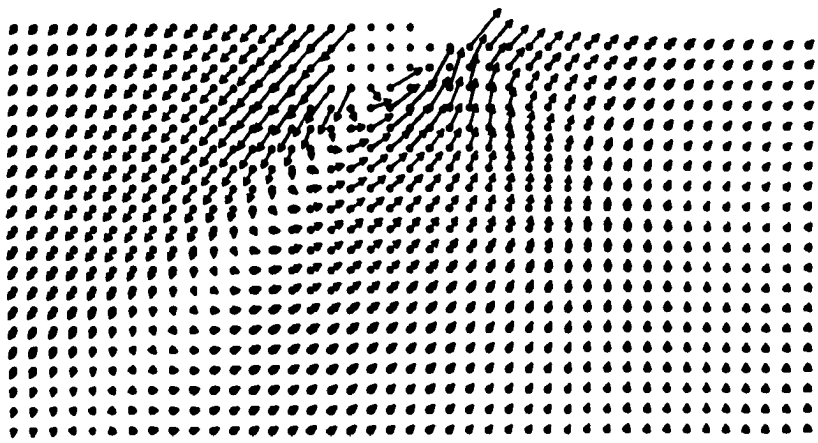


Figure 4.3. Interaction energy of the steps on vicinal ($\bar{1}\bar{m}0$) surfaces versus the square of the inverse step separation for (a) gold and (b) nickel.

Reproduced with permission of the copyright owner. Further reproduction prohibited without permission.

Fig. 4.4a



Reproduced with permission of the copyright owner. Further reproduction prohibited without permission.

Fig. 4.4b

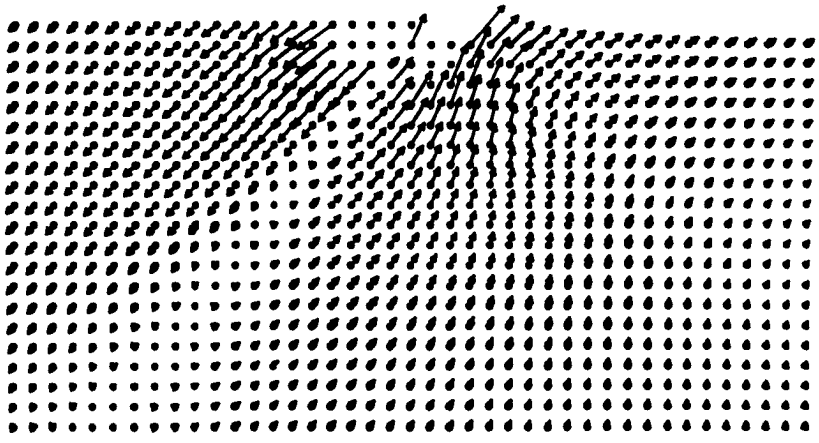


Fig. 4.4c

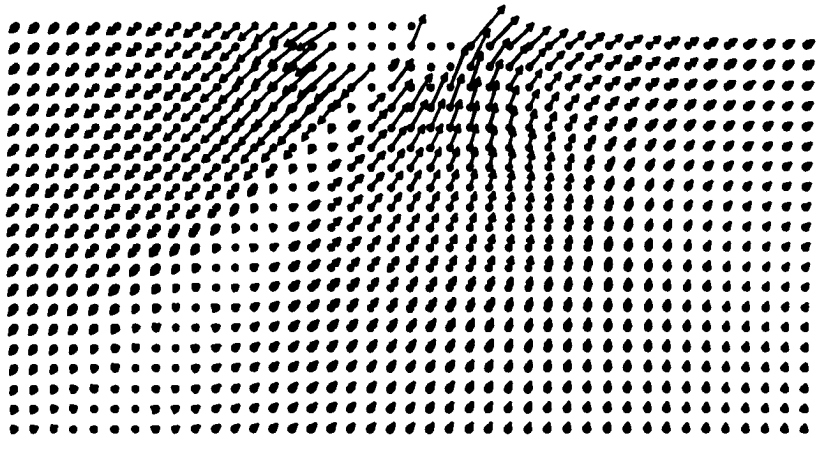


Figure 4.4. Displacement field for a periodic array of <100> steps on a {001} surface obtained from the atomistic simulations. Figure (a) and (b) corresponds to gold and nickel surfaces, respectively, with a step separation $d_0 = 80\ a_0$ (only a segment of the surface is shown). Figure (c) is the same as (b) except that $d_0 = 300\ a_0$. In order to improve the clarity, the atomic displacement vectors are magnified by a factor of 100 for gold and 200 for nickel. Displacements larger than $5\ 10^{-3}\ a_0$, in the core region, are not shown.

Reproduced with permission of the copyright owner. Further reproduction prohibited without permission.

Fig. 4.5a

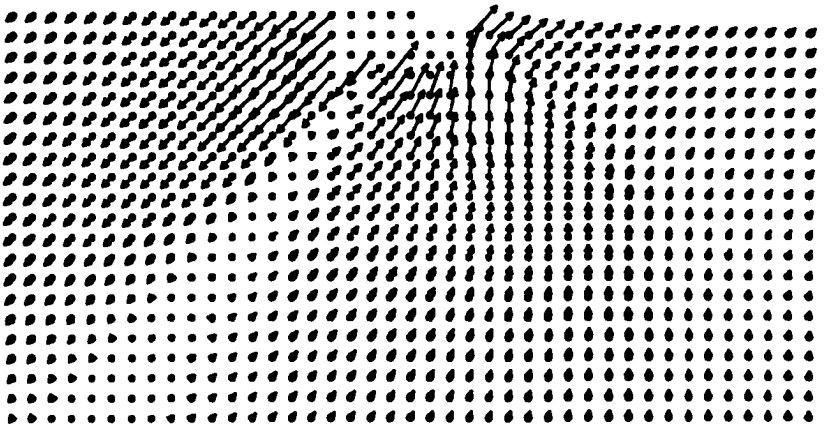


Fig. 4.5b

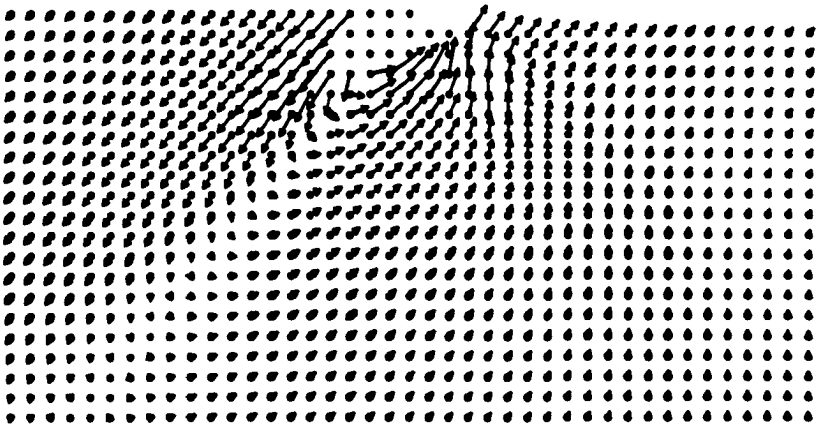


Figure 4.5. Displacement field for a periodic array of <100> steps on a {001} surface obtained from the anisotropic elastic theory (Eq. 11) using the best fit surface line force dipole vector **D**, Figure (a) and (b) corresponds to gold and nickel surfaces, respectively, with a step separation $d_0 = 80\, a_0$ (only a segment of the surface is shown). The magnification factor used for the displacements are exactly as shown in Fig. 4.4.

Reproduced with permission of the copyright owner. Further reproduction prohibited without permission.

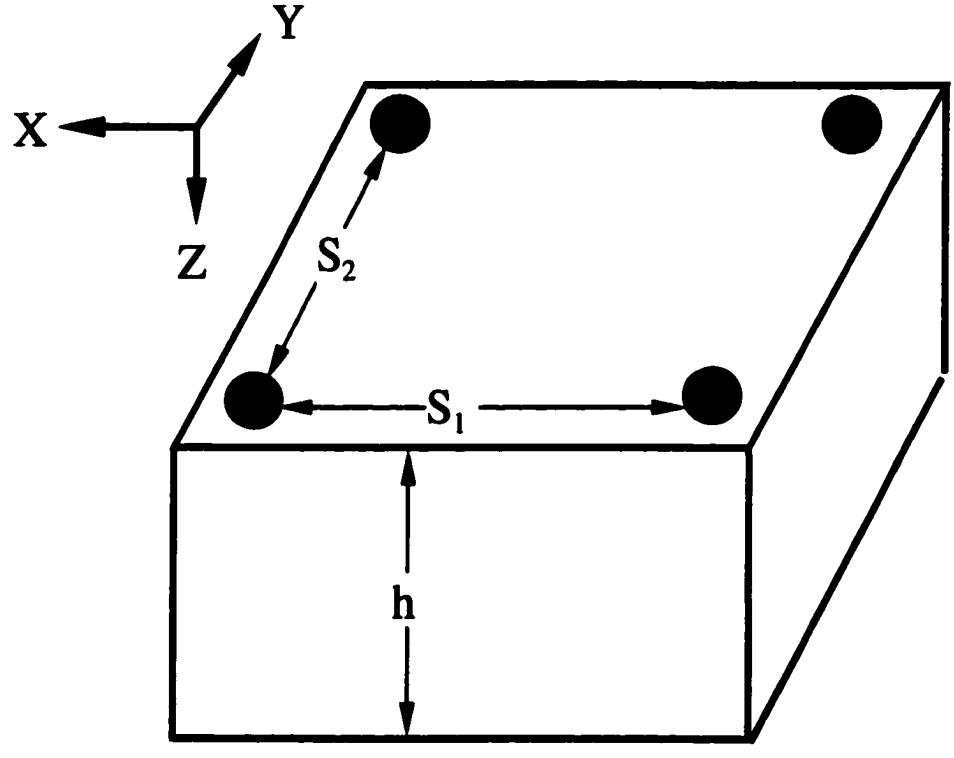


Figure 4.6. Geometry of the simulation cell used to determine the adatom - adatom interaction strength. Periodic boundary conditions are imposed in the x and y directions.

Reproduced with permission of the copyright owner. Further reproduction prohibited without permission.

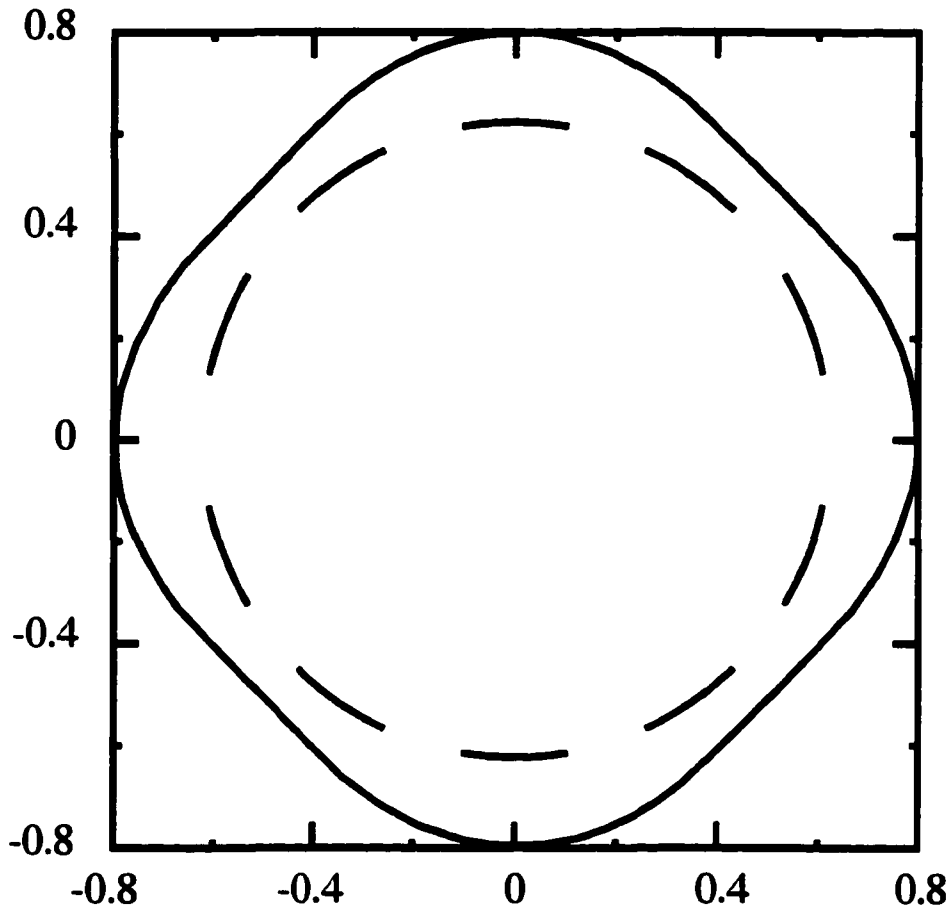


Figure 4.7. Polar plot of $h_{zz}(\alpha)$ for the {001} plane of EAM Ni (solid curve). The scale on both axes is $Å^3/eV$. The dashed curve denotes the same quantity obtained using isotropic elasticity with the Voigt average elastic constants of EAM Ni.

Reproduced with permission of the copyright owner. Further reproduction prohibited without permission.

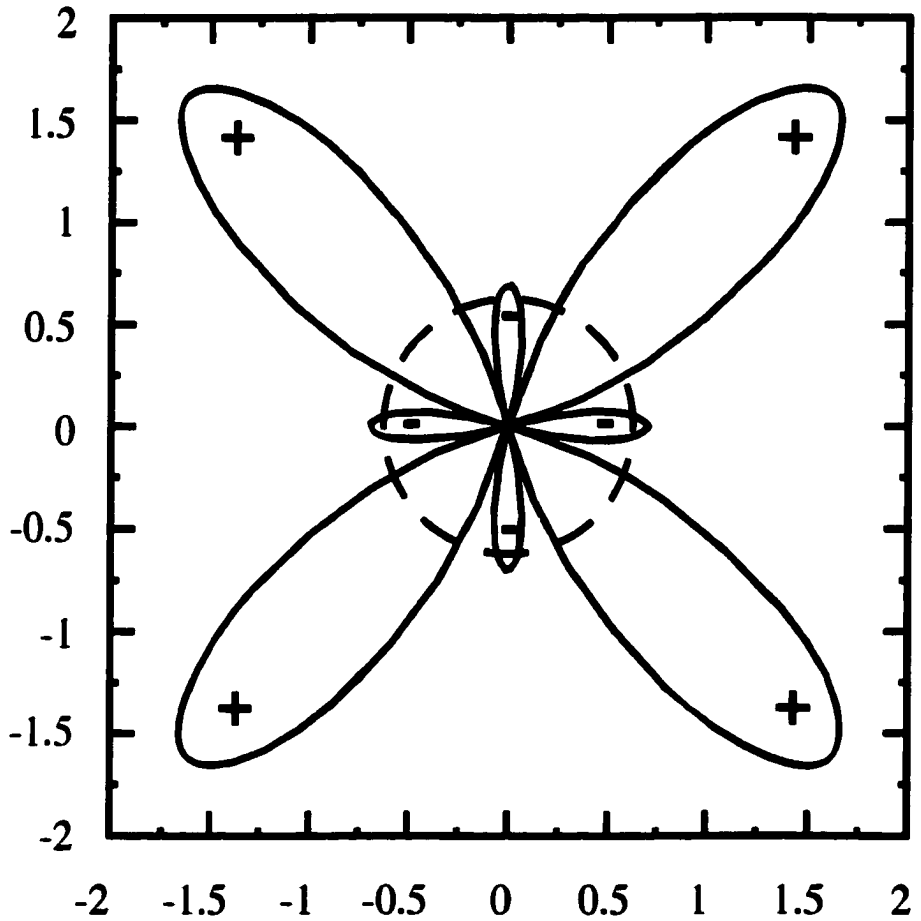


Figure 4.8. Polar plot of the adatom interaction energy, as per Eq. (36) (solid curve). The scale on both axes is $Å^3/eV$. The '+' and '-' denotes repulsive and attractive regions, respectively. The dashed curve denotes the same quantity obtained using isotropic elasticity with the Voigt average elastic constants of EAM Ni. The isotropic solution is repulsive everywhere.

Reproduced with permission of the copyright owner. Further reproduction prohibited without permission.

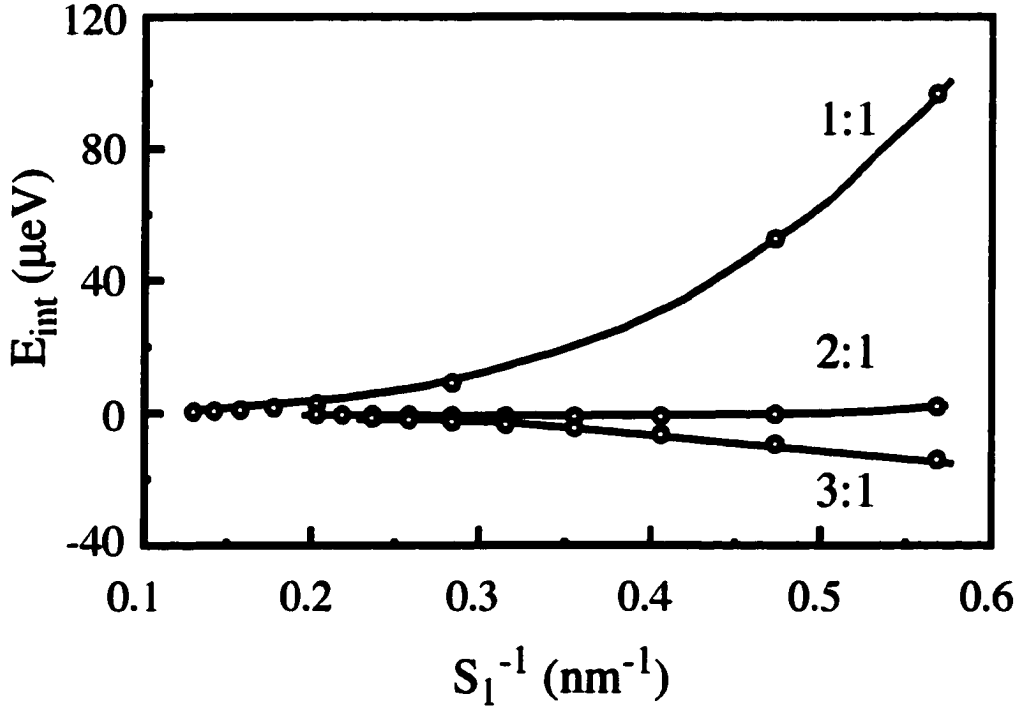


Figure 4.9. The adatom-adatom interaction energy for adatoms on the (001) surface of EAM Ni vs. the inverse nearest neighbor adatom separation S_1^{-1} for different adatom lattice period ratios: S_2:S_1. The lines drawn through the data points are best fits to Eq. (38).

Reproduced with permission of the copyright owner. Further reproduction prohibited without permission.

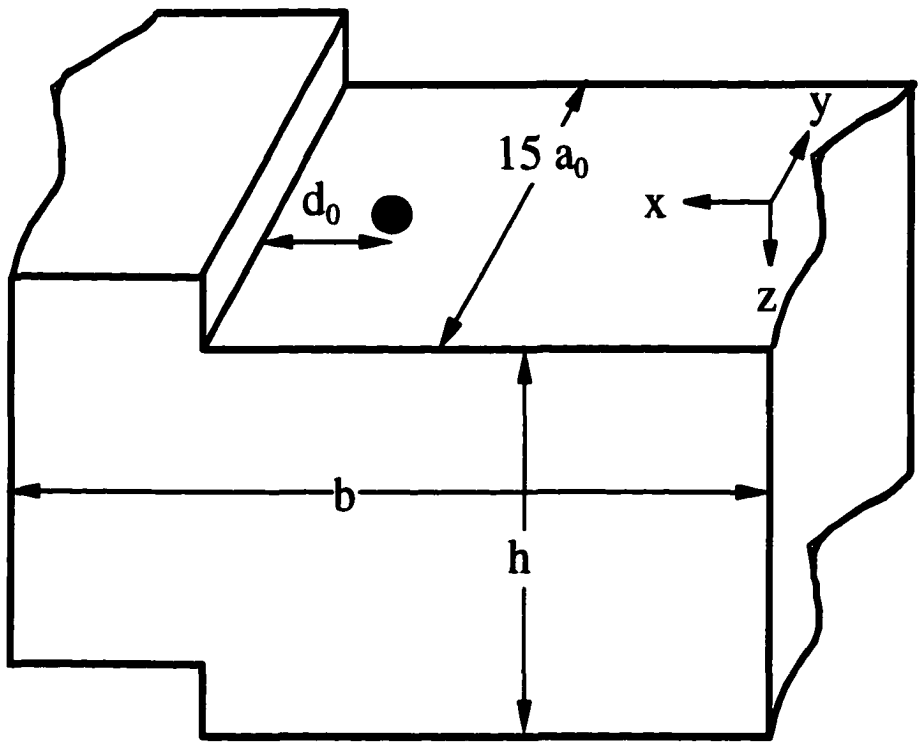


Figure 4.10. Geometry of the simulation cells used to determine step - adatom interaction strength. In both cases, periodic boundary conditions are imposed in the x and y directions.

Reproduced with permission of the copyright owner. Further reproduction prohibited without permission.

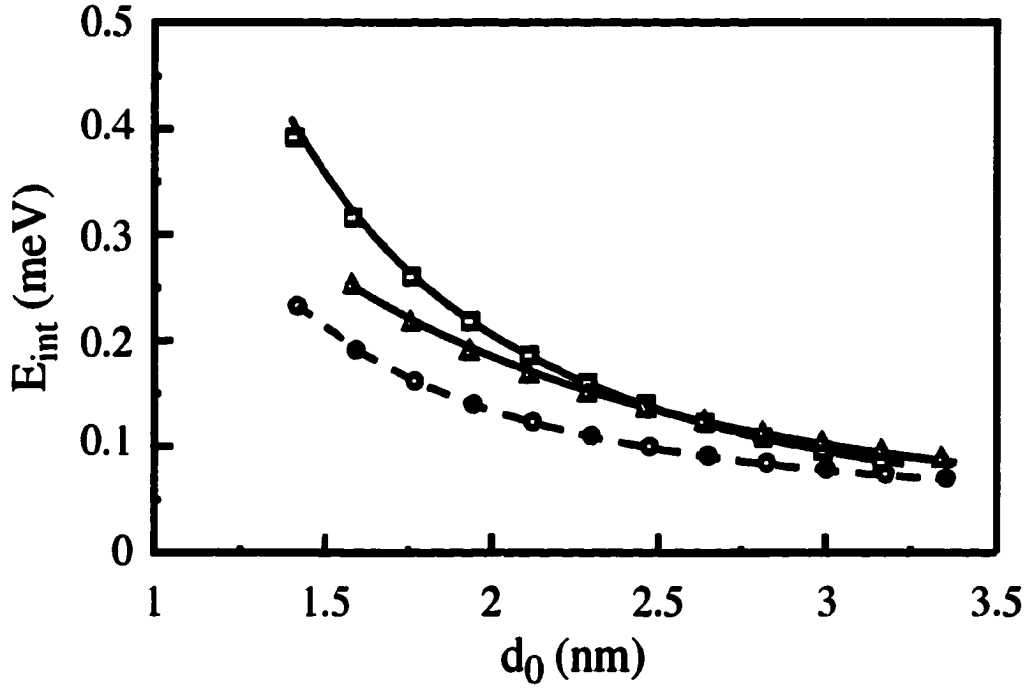


Figure 4.11. The step-adatom interaction energy for the case of a (001) surface with [100] steps in EAM Ni. The data indicated by the squares and triangles correspond to adatoms on the terraces immediately above and below the step, respectively. The dashed line is calculated according to Eq. (45) with no adjustable parameters. The solid lines correspond to the best fit of the data to Eq. (46).

Reproduced with permission of the copyright owner. Further reproduction prohibited without permission.

CHAPTER V

CONCLUSIONS AND SUGGESTIONS FOR FUTURE RESEARCH

In this dissertation, several consequences of the elastic nature of interfaces were discussed. Three specific problems were examined in which we attempted to elucidate some macroscopic and microscopic aspects of interfaces. These problems are: 1) Elastic analysis of dislocations at interfaces; 2) Morphology evolution during multilayer film growth; 3) Elastic models of surface defects. Below we summarize the results and suggest the directions for future research in order to put things in perspective.

Elastic analysis of dislocations at interfaces

In treating this problem, we employed a linear model of interfacial bonding and continuum elastic analysis to study dislocations near a heterophase interface. We presented a simple method for determining elastic fields in such bimaterials originating from internal sources of stress (such as dislocations). Using this method, we determined the forces acting on dislocations as a function of the dislocation-interface separation, the strength of the bonding at the interface and elastic constants of and misfit between the bounding materials.

The method used to solve this problem employs the assumption of the linearity of the traction – displacement dependence of bonding at the interface. While this may be a good approximation for the limiting cases of a "welded" and "slipping" interface, a more realistic traction – displacement curve must include nonlinearity. The nonlinearity naturally occurs in this problem, because for a large jump in displacement, the traction at the interface must go to zero, as a real interface has a tendency for sliding and crack

Reproduced with permission of the copyright owner. Further reproduction prohibited without permission.

opening. A realistic description of this nonlinearity must be based on the nature of the atomic bonding at the interface. Hence, our analysis may give erroneous results when a dislocation is close to the bimaterial interface and the stresses in the material close to the interface are large. Introducing the nonlinearity into the problem, however gloomy the prospect for doing this analytically might look, will make it possible to address two issues. First, it will be possible to analyze the problem, where a dislocation or an assembly of dislocations, such as a pile-up, exerts large stresses on the interface. One example of the importance of such a process is dislocation pile-up leading to interfacial microcracking. The second issue which should be addressed is the incorporation of data on bond strength, obtained from electronic calculations to the problem. An interim suggestion is to use an empirical form of the nonlinear force-displacement arrangement, such as the Universal Binding Energy Relation [1], as used by Needleman in finite element modeling [2]. This will provide a smooth transition from the microscopic, atomic level description of the interface, to the mesoscopic level, at which the dislocations come into play.

Morphology evolution during multilayer film growth

We analyzed the stability of multilayer thin films during growth. We examined the case in which the evolution of the growing film is controlled by diffusion along the growth surface. The nature and extent of the surface diffusion is controlled by the interplay between surface tension, the elastic strain energy arising from misfit, and the morphology of both the growing surface and buried interfaces. The problem was analyzed to the first order in perturbation theory where the small parameter is the product of perturbation wave vector and amplitude. We found that multilayer film growth can be stabilized by appropriate choice of material parameters and growth conditions. This is a novel result, because , a monolitic film growing under the same stress is unstable against

Reproduced with permission of the copyright owner. Further reproduction prohibited without permission.

forming surface undulations. We also predicted the conditions for unstable growth and the nature of the resultant morphological instability.

The linear stability analysis employed in the problem correctly predicts the region of stable film growth, but is incapable of describe the true asymptotic multilayer film morphology. This is because the analysis is valid for only small perturbations and even a slowly growing instability will eventually lead to morphologies with too large of an amplitude to be described in this linear theory. Near the boundary of the stable region of the predicted stability diagram, the analysis will be valid for several layers of film growth, but far from it, the analysis could break down even before the first layer is completely grown. Unfortunately, the latter is quite common for the technically important multilayer compound semiconductor case. To remedy this situation, it is necessary to include the nonlinear terms in the analysis. This involves both determining the nonlinearities in the chemical potential as a function of surface morphology and solving the resultant evolution equations without resorting to perturbation theory. Such an approach will undoubtedly force us to solve this problem numerically – possibly by finite elements.

Another effect of the stress driven morphology evolution in multilayer films which needs to be re-examined involves the effect of mass transport below the growing surface. In the present approach, we explicitly assumed that everything below the growing surface was frozen. This is reasonable if surface diffusion is much faster than bulk diffusion and bulk diffusion is negligible over the time required to grow the entire film. There are observations that bulk diffusion may indeed be significant during the growth of III-V mulilayer films [3]. This will also be key in understanding the results of growth interrupt experiments or post-growth annealing. We can now write down the equations that account for both the nonlinearity effects described above and sub-surface diffusion, but little thought has been given to the method of solution.

Reproduced with permission of the copyright owner. Further reproduction prohibited without permission.

Elastic models of surface defects

We employed elastic analyses and atomistic computer simulations to study the interactions between defects (surface steps, adsorbed atoms) on solid surfaces. The simulations data were analyzed in terms of a 'dipole' model in which the defect is replaced by a surface force couple. We found that the dipole model provides a good description of interactions between two surface steps and between two adsorbed atoms and a satisfactory description of interactions between a step and an adatom. For the interaction between two adsorbed atoms we emphasized the importance of anisotropy in the treatment of surface defects. The computer simulations employed in the study that we have completed did not consider a wide range of surface and step orientations or crystallography. It is important to determine the range of applicability of the isotropic results and determine the adequacy of the anisotropic solutions based on simply dipole models for describing surface defects in more cases. A second area where more research should be done is in determining the importance/relative magnitude of higher order terms in the multipole expansion. Most simulations performed to date have focussed on close packed metals. While these represent a good test bed, they do not represent all materials – especially those with more open crystal structures.

The idea that a surface step may be represented as a surface force dipole may also be applicable to materials interfaces, because interfaces have interfacial stress which are similar to the surface stress for the free surface. It would be interesting to study the energetics of vicinal interfaces (near low Σ orientations) to elucidate the nature of interfacial steps and secondary dislocation structure. This would provide additional insight into the problem of phase transformations, since interfacial defects, especially steps often play a key role in determining how a new phase will grow and act as heterogenous nucleation centers in phase transformations.

Reproduced with permission of the copyright owner. Further reproduction prohibited without permission.

References to Chapter V

[1] G. Bozzolo, J. Ferrante and J. R. Smith, *Scripta Met.* **25**, 1927 (1991).

[2] A. Needleman, *J. Appl. Mech.* **54**, 525 (1987).

[3] B. Lita, R. S. Goldman, J. D. Phillips, P. K. Bhattacharya, *Appl. Phys. Lett.*, **74**, 2824 (1999).

Reproduced with permission of the copyright owner. Further reproduction prohibited without permission.

APPENDICES

Reproduced with permission of the copyright owner. Further reproduction prohibited without permission.

APPENDIX 2A

SURFACE GREEN'S FUNCTION

To describe the stress field in a half space we begin with the Airy stress function $\chi(x,y)$, which satisfies the biharmonic equation:

$$\nabla^4 \chi = 0 \ . \tag{2A.1}$$

Fourier transforming Eq. (2A.1) along the x direction yields [12]

$$\left(\frac{\partial^2}{\partial y^2} - \xi^2\right)^2 \chi(\xi, y) = 0 \ldots \tag{2A.2}$$

The solution to this equation is:

$$\begin{aligned} \chi(\xi, y) &= (My + N)\exp(-|\xi| y) \qquad y > 0 \\ \chi(\xi, y) &= (My + N)\exp(|\xi| y) \qquad y < 0 \ . \end{aligned} \tag{2A.3}$$

The stresses and displacements may be found directly from the stress function χ and Hooke's law [12]

$$\sigma_{xx} = \frac{\partial^2 \chi}{\partial y^2} \mathrm{a} \ , \quad \sigma_{yy} = -\xi^2 \chi \ , \quad \sigma_{xy} = -i\xi \frac{\partial \chi}{\partial y} \tag{2A.4}$$

$$2\mu \mathbf{u}_x = \left[(1-\nu)\frac{\partial^2 \chi}{\partial y^2} + \xi^2 \nu \chi\right] / i\xi \ , \quad 2\mu \mathbf{u}_y = \left[(1-\nu)\frac{\partial^3 \chi}{\partial y^3} + \xi^2 (\nu - 2)\frac{\partial \chi}{\partial y}\right] / \xi^2 \tag{2A.5}$$

Here μ and ν are the elastic constants of the appropriate materials μ_1, ν_1 and μ_2 and ν_2 for materials **1** and **2**, respectively).

The constants M and N in Eq. (2A.3) can be determined directly from the traction boundary conditions

Reproduced with permission of the copyright owner. Further reproduction prohibited without permission.

$$\begin{aligned} &\sigma_{yy} = -\mathbf{T}_y \quad \text{and} \quad \sigma_{xy} = -\mathbf{T}_x && y = 0^+ \\ &\sigma_{yy} = \mathbf{T}_y \quad \text{and} \quad \sigma_{yy} = \mathbf{T}_y && y = 0^-, \end{aligned} \tag{2A.6}$$

where $\mathbf{T}_x$ and $\mathbf{T}_y$ are the Fourier transform of the tangential and normal components of the tractions on the surface of a half-space and $y = 0^+$ and 0^- indicate the surfaces of the $y > 0$ and $y < 0$ half spaces, respectively. The resultant constants are

$$\begin{aligned} &M = \frac{\mathbf{T}_y}{|\xi|} + \frac{\mathbf{T}_x}{i\xi} \quad \text{and} \quad N = \frac{T_y}{\xi^2} && y > 0 \\ &M = \frac{\mathbf{T}_y}{|\xi|} - \frac{\mathbf{T}_x}{i\xi} \quad \text{and} \quad N = -\frac{T_y}{\xi^2} && y < 0 \ . \end{aligned} \tag{2A.7}$$

Combining Eqs. (2A.5)-(2A.7) we obtain the relationships between the surface tractions and the displacements in each half space; these are the surface Green functions $\mathbf{G}_1$ and $\mathbf{G}_2$ presented in Eqs. (4) and (6). Inserting the stress function Eq. (2A.3) into Eq. (2A.4) yields the stress field throughout the half-space. In particular, $\sigma_{xx}(\xi,y)$ for material **1** is:

$$\sigma_{xx}(\xi, y) = \frac{\partial^2 \chi}{\partial y^2} = \left[\xi^2 (My + N) - 2M|\xi|\right] \exp(-y|\xi|) \ . \tag{2A.8}$$

Substituting the values of A and B in terms of the surface tractions (Eq. 2A.7a) into Eq. (2A.8) and separating the two components of the traction vector $\mathbf{T}_x$ and $\mathbf{T}_y$, we obtain the relationship between the Fourier transform of the surface tractions and the stress throughout the half space; this is the vector **W** presented in Eq. (14).

Reproduced with permission of the copyright owner. Further reproduction prohibited without permission.

APPENDIX 2B

EXPONENTIAL INTEGRAL IDENTITIES

The following relations were used to obtain Eq. (18): $\alpha\int_0^\infty dt\frac{e^{-t}}{t+\alpha}=1-e^{\alpha}\mathrm{Ei}(2,\alpha)$, $\alpha\int_0^\infty dt\frac{te^{-t}}{t+\alpha}=1-2e^{\alpha}\mathrm{Ei}(3,\alpha)$ and $\alpha\int_0^\infty dt\frac{te^{-t}}{t+\alpha}=2-6e^{\alpha}\mathrm{Ei}(4,\alpha)$, where the exponential integral $\mathrm{Ei}(n,\alpha)$ is defined as $\mathrm{Ei}(n,\alpha)\equiv\int_1^\infty dt\frac{e^{-\alpha t}}{t^n}$. In the limit $\alpha = 0$ limit, the exponential integral is simply $\mathrm{Ei}(n,0)=\frac{1}{n-1}$. The exponential integral is bounded as follows: $\frac{1}{x+n}\le e^{x}\,\mathrm{Ei}(n,x)\le\frac{1}{x+n-1}$.

Reproduced with permission of the copyright owner. Further reproduction prohibited without permission.

APPENDIX 2C

EVALUATION OF THE FOURIER SERIES

In deriving the expressions for the climb force acting on the array of dislocations in Eqs. (24) and (28), we must evaluate summations of the form:

$$\sum_{n=1}^{\infty}\frac{e^{-nx}}{1+ny}\ ,\quad \sum_{n=1}^{\infty}\frac{ne^{-nx}}{1+ny}\quad\text{and}\quad \sum_{n=1}^{\infty}\frac{n^2e^{-nx}}{1+ny}\ . \tag{2C.1}$$

In the $\kappa_t = \infty$ limit, $y = 0$ in Eqs. (1C.1) and these equations reduce to:

$$\sum_{n=1}^{\infty}e^{-nx}=\frac{e^{-x/2}}{2\sinh(x/2)}\ ,\quad \sum_{n=1}^{\infty}ne^{-nx}=-\frac{d}{dx}\sum_{n=1}^{\infty}e^{-nx}=\frac{1}{4\sinh^2(x/2)}$$

$$\sum_{n=1}^{\infty}n^2e^{-nx}=-\frac{d}{dx}\sum_{n=1}^{\infty}ne^{-nx}=\frac{\cosh(x/2)}{4\sinh^3(x/2)} \tag{2C.2}$$

The following analysis of these equations is as suggested by Eykholt [22]. The first series in Eq. (2C.1) can be evaluated as follows. First, we define a function

$$F(x,y)=\sum_{n=1}^{\infty}\frac{e^{-nx}}{1+ny}\ . \tag{2C.3}$$

Then

$$F-y\frac{\partial F(x,y)}{\partial x}=\sum_{n=1}^{\infty}e^{-nx}=\frac{e^{-x/2}}{2\sinh(x/2)} \tag{2C.4}$$

and, therefore,

$$\frac{\partial}{\partial x}\left(e^{-x/y}F(x,y)\right)=-\frac{e^{-x/2}}{2y\sinh(x/2)}e^{-x/y} \tag{2C.5}$$

Reproduced with permission of the copyright owner. Further reproduction prohibited without permission.

Since F(x,y) goes to zero as x tends to infinity, both sides of Eq. (2C.5) can be integrated over x in the range from x to ∞:

$$F(x,y)=\frac{e^{x/y}}{y}\int_{x}^{\infty}d\zeta\frac{e^{-\zeta/2}}{2\sinh(\zeta/2)}e^{-\zeta/y} \tag{2C.6}$$

Using a change of variables $e^{-\zeta}=t$ and integrating Eq. (2C.6) by parts one obtains:

$$F(x,y)=\frac{e^{-x/2}}{2\sinh(x/2)}-e^{x/y}\int_{0}^{e^{-x}}dt\frac{t^{1/y}}{(1-t)^2} \tag{2C.7a}$$

The summation of the other two series in Eq. (2C.1) can be computed by differentiation of Eq. (2C.7a) with respect to x and, then, integrating the result by parts

$$\sum_{n=1}^{\infty}\frac{ne^{-nx}}{1+ny}=-\frac{\partial F(x,y)}{\partial x}=\frac{1}{4\sinh^2(x/2)}-e^{x/y}\int_{0}^{e^{-x}}dt\frac{t+1}{(1-t)^3}t^{1/y}\ , \tag{2C.7b}$$

$$\sum_{n=1}^{\infty}\frac{n^2e^{-nx}}{1+ny}=\frac{\partial^2 F(x,y)}{\partial x^2}=\frac{\cosh(x/2)}{4\sinh^3(x/2)}-e^{x/y}\int_{0}^{e^{-x}}dt\frac{t^2+4t+1}{(1-t)^4}t^{1/y}\ . \tag{2C.7c}$$

The integrals in (Eq. 2C.7) can be rewritten in terms of incomplete beta-functions:

$$\int_{0}^{\exp(-x)}dt\frac{t^{1/y}}{(1-t)^2}=B_{e^{-x}}(1+\frac{1}{y},-1) \tag{2C.8a}$$

$$\int_{0}^{\exp(-x)}dt\frac{t+1}{(1-t)^3}t^{1/y}=2B_{e^{-x}}(1+\frac{1}{y},-2)-B_{e^{-x}}(1+\frac{1}{y},-1)\ , \tag{2C.8b}$$

$$\int_{0}^{\exp(-x)}dt\frac{t^2+4t+1}{(1-t)^4}t^{1/y}=B_{e^{-x}}(1+\frac{1}{y},-1)-6B_{e^{-x}}(1+\frac{1}{y},-2)+6B_{e^{-x}}(1+\frac{1}{y},-3)\ , \tag{2C.8c}$$

Reproduced with permission of the copyright owner. Further reproduction prohibited without permission.

where $B_x(\alpha,\beta) = \int_0^x t^{\alpha-1}(1-t)^{\beta-1}dt$.

Substituting the values 2Λ and $2/\beta$ for x and y into Eqs. (2C.1) and (2C.7), we obtain (Eqs. 24 and 28).

Reproduced with permission of the copyright owner. Further reproduction prohibited without permission.

APPENDIX 3A

SURFACE STRESS FROM A BURIED LINE LOAD

In this Appendix, we determine the stress at the growing surface associated with the presence of an interface between misfitting layers n and n+1. This result is used in Section 3.3 above. To first order in perturbation theory, this is equivalent to finding the stress produced by a line force of magnitude equal to the corrective tractions applied at the interface. Although the corrective tractions in the present problem only have components tangential to the interface, we present the formulae for a more general problem where both normal and tangential tractions are present.

Consider an isotropic elastic half-space occupying the domain $y < 0$ as shown in Fig. 3A.1 in which a line load $\mathbf{F}(x)$ is buried at depth h. To find the stress field in the half-plane, we derive the stress field created by this load in the whole plane and then apply a corrective solution to satisfy the boundary conditions at the free surface. The Green's function for the whole plane [28] is:

$$\tilde{\mathbf{G}} = \frac{1}{2\mu\left(\xi^2+\eta^2\right)^2}\begin{pmatrix} 2\eta^2+\frac{1-2\nu}{1-\nu}\xi^2 & -\frac{\xi\eta}{1-\nu} \\ -\frac{\xi\eta}{1-\nu} & 2\xi^2+\frac{1-2\nu}{1-\nu}\eta^2 \end{pmatrix} . \tag{3A.1}$$

A tilde indicates that a quantity is in reciprocal space, μ is the shear modulus, and ξ and η are the x and y component of the wave vector, respectively. Equation (3A.1) provides the relationship between the general body force $\mathbf{F}$ and the displacement field. The stress tensor σ_{ij} is obtained from the definition of the strain and Hooke's law:

$$\tilde{\sigma}_{xx} = 2\mu\left[\tilde{\varepsilon}_{xx}+\frac{\nu}{1-2\nu}\left(\tilde{\varepsilon}_{xx}+\tilde{\varepsilon}_{yy}\right)\right] = \frac{i}{\left(\xi^2+\eta^2\right)}\left[\left(\xi\tilde{F}_x-\eta\tilde{F}_y\right)+\frac{\eta^2}{(1-\nu)}\frac{\left(\xi\tilde{F}_x+\eta\tilde{F}_y\right)}{\left(\xi^2+\eta^2\right)}\right]$$

Reproduced with permission of the copyright owner. Further reproduction prohibited without permission.

$$\tilde{\sigma}_{yy} = 2\mu\left[\tilde{\varepsilon}_{yy} + \frac{\nu}{1-2\nu}\left(\tilde{\varepsilon}_{xx} + \tilde{\varepsilon}_{yy}\right)\right] = \frac{i}{\left(\xi^2+\eta^2\right)}\left[\left(\eta\tilde{F}_y - \xi\tilde{F}_x\right) + \frac{\xi^2}{(1-\nu)}\frac{\left(\xi\tilde{F}_x + \eta\tilde{F}_y\right)}{\left(\xi^2+\eta^2\right)}\right] \quad (3A.2)$$

$$\tilde{\sigma}_{xy} = 2\mu\tilde{\varepsilon}_{xy} = \frac{i}{\left(\xi^2+\eta^2\right)}\left[\left(\eta\tilde{F}_x + \xi\tilde{F}_y\right) - \frac{\xi\eta}{(1-\nu)}\frac{\left(\xi\tilde{F}_x + \eta\tilde{F}_y\right)}{\left(\xi^2+\eta^2\right)}\right]$$

To find the stress field created by a sinusoidal line load **f** at depth h ($h > 0$)

$$\mathbf{f} = \mathbf{f}(x)\delta(y+h)\,, \quad (3A.3)$$

we inverse Fourier transform Eq. (3A2) with respect to the variable η:

$$\sigma_{xx}(\xi,y) = \frac{e^{-|\xi|y+h|}}{4(1-\nu)}\left[i\left(3-2\nu-|\xi\|y+h|\right)sign(\xi)\tilde{f}_x + \left(|\xi\|y+h|-2\nu\right)sign(y+h)\tilde{f}_y\right]$$

$$\sigma_{yy}(\xi,y) = \frac{e^{-|\xi|y+h|}}{4(1-\nu)}\left[i\left(2\nu+|\xi\|y+h|-1\right)sign(\xi)\tilde{f}_x - \left(2(1-\nu)+|\xi\|y+h|\right)sign(y+h)\tilde{f}_y\right] \quad (3A.4)$$

$$\sigma_{xy}(\xi,y) = \frac{e^{-|\xi|y+h|}}{4(1-\nu)}\left[\left(|\xi\|y+h|-2(1-\nu)\right)sign(y+h)\tilde{f}_x + i\left(1-2\nu+|\xi\|y+h|\right)sign(\xi)\tilde{f}_y\right]$$

At the surface ($y = 0$) the xx-component of the stress tensor is:

$$\sigma_{xx}(\xi,0) = \frac{e^{-|\xi|h}}{4(1-\nu)}\left[i\left(3-2\nu-|\xi|h\right)sign(\xi)\tilde{f}_x + \left(|\xi|h-2\nu\right)\tilde{f}_y\right] \quad (3A.5)$$

and the tractions at the free surface are:

$$T_x = \sigma_{xy}(\xi,0) = \frac{e^{-|\xi|h}}{4(1-\nu)}\left[\left(|\xi|h-2(1-\nu)\right)\tilde{f}_x + i\left(1-2\nu+|\xi|h\right)sign(\xi)\tilde{f}_y\right] \quad (3A.6)$$

$$T_y = \sigma_{yy}(\xi,0) = \frac{e^{-|\xi|h}}{4(1-\nu)}\left[i\left(2\nu+|\xi|h-1\right)sign(\xi)\tilde{f}_x - \left(2(1-\nu)+|\xi|h\right)\tilde{f}_y\right]$$

To satisfy the traction free boundary conditions at the surface, we apply corrective tractions $\mathbf{T}_c = -\mathbf{T}$. The xx-component of the stress field at the surface ($y = 0$) is the sum of

Reproduced with permission of the copyright owner. Further reproduction prohibited without permission.

the stress produced by the line load (Eq. 3A.6) and that produced by the corrective solution:

$$\sigma_{xx}(\xi, h) = e^{-|\xi|h}\left(i\left[2 - \frac{|\xi|h}{1-\nu}\right] sign(\xi)\tilde{f}_x + \frac{(1-2\nu+|\xi|h)}{1-\nu}\tilde{f}_y \right) \qquad (3A.7)$$

Setting the value of the normal component $\mathbf{f}_y$ to zero and the tangential component as per Eq. (7), yields the correction to the surface traction produced by the *n*/*n*+1 interface (Eq. 13).

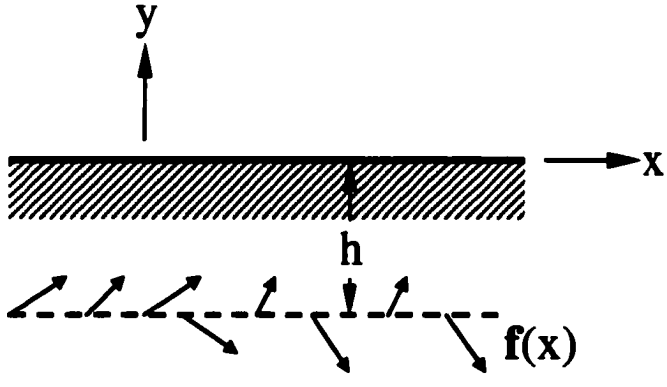


Figure 3A.1. The geometry used to compute the stress on the surface caused by an interface buried at depth *h*. The interface is modeled by a line load which can vary along x, f(*x*).

Reproduced with permission of the copyright owner. Further reproduction prohibited without permission.

APPENDIX 3B

SOLUTION OF THE RECURRENCE RELATIONS

In this Appendix, we obtain closed form solutions to the evolution equations for the surface of the growing multilayer film. As in the text, we first consider the special case where materials A and B are identical in every respect, except that the magnitude of the misfit stress Σ with respect to the substrate is equal and opposite in the two materials (i.e., $\beta = -1$). In this case, the integration of the evolution equation resulted in two expressions (Eqs. 24' and 22'):

$$X_k = X_{k-1}F - 2\sum_{j=1}^{k-1}(-1)^{k-j-1}X_j\left[\Psi H^*(k-j-1)+\Xi\right] \tag{3B.1}$$

and

$$X_j = \Delta_j e^{\xi^* H^*(j-1)} \tag{3B.2}$$

from which the amplitude of the perturbation Δ_k of layer k can be found using successive iterations. This recurrence relation can be greatly simplified by rewriting Eq. (3B.1) as

$$X_{k+3} = X_{k+2}(F-2-2\Xi)+X_{k+1}\left(2F-1+2\Psi H^*-2\Xi\right)+X_kF \ , \tag{3B.3}$$

which only involves four consecutive terms. Applying Eq. (3B.2) to the previous relation produces a recurrence relation for Δ_k:

$$\Delta_{k+3} = \Delta_{k+2}e^{-\xi^* H^*}(F-2-2\Xi)+\Delta_{k+1}e^{-2\xi^* H^*}\left(2F-1+2\Psi H^*-2\Xi\right)+\Delta_k e^{-3\xi^* H^*}F \tag{3B.4}$$

As in the text, we normalize the amplitudes of the perturbation Δ_k by Δ_1: $\Delta_k^+ = \Delta_k / \Delta_1$. Δ_k^+ can be rewritten in closed form in terms of a power of the 3x3 matrix **L**:

Reproduced with permission of the copyright owner. Further reproduction prohibited without permission.

$$\mathbf{L}=\begin{pmatrix} e^{-\xi^* H^*}(F-2-2\Xi) & 1 & 0 \\ e^{-2\xi^* H^*}\left(2F-1+2\Psi H^*-2\Xi\right) & 0 & 1 \\ e^{-3\xi^* H^*}F & 0 & 0 \end{pmatrix}. \tag{3B.5}$$

The perturbation amplitudes for three consecutive layers can be expressed as vectors $\mathbf{Y}_k$: $\mathbf{Y}_k=\left\langle \Delta^+_{k+2},\ \Delta^+_{k+1},\ \Delta^+_k \right\rangle$. The vector $\mathbf{Y}_k$ is related to the vector $\mathbf{Y}_1$ by the (k-1)th power of matrix $\mathbf{L}$: $\mathbf{Y}_k=\left\langle \Delta^+_{k+2},\ \Delta^+_{k+1},\ \Delta^+_k \right\rangle=\mathbf{Y}_1\mathbf{L}^{k-1}=\left\langle \Delta^+_3,\ \Delta^+_2,\ \Delta^+_1 \right\rangle\mathbf{L}^{k-1}$. Finding the values of Δ_2 and Δ_3 using Eqs. (22'), (24') and arbitrary Δ_1 determines the vector $\mathbf{Y}_1$. Applying the matrix $\mathbf{L}$ to this vector k-1 times determines the amplitude Δ^+_k.

The power of the matrix grows as fast as the power if its eigenvalues. We denote the three eigenvalues of the matrix $\mathbf{L}$ as λ_1, λ_2 and λ_3. Assuming that $\mathbf{L}$ is not degenerate, we express the matrix of eigenvectors $\mathbf{\Lambda}$ of matrix $\mathbf{L}$ as:

$$\mathbf{\Lambda}=\begin{pmatrix} \lambda_1^2 & \lambda_1 & 1 \\ \lambda_2^2 & \lambda_2 & 1 \\ \lambda_3^2 & \lambda_3 & 1 \end{pmatrix}. \tag{3B.6}$$

The expression for Δ^+_k ($k \geq 4$) can now be written as:

$$\Delta^+_k=\alpha_1\lambda_1^{k-1}+\alpha_2\lambda_2^{k-1}+\alpha_3\lambda_3^{k-1}\ , \tag{3B.7}$$

where the α's are the coefficients of the expansion of vector $\mathbf{Y}_1$ in the basis of the eigenvectors of matrix $\mathbf{L}$: $\langle \alpha_1,\ \alpha_2,\ \alpha_3 \rangle=\mathbf{Y}_1\mathbf{\Lambda}^{-1}=\langle \Delta_3^+,\ \Delta_2^+,\ 1 \rangle\mathbf{\Lambda}^{-1}$. Δ^+_k grows asymptotically as the power of the maximal eigenvalue of matrix $\mathbf{L}$. Because of this power law, the asymptotic regime is reached quickly, provided that the coefficient α_i corresponding to that maximal eigenvalue of $\mathbf{L}$ (denoted λ_1), is not much smaller than the other two α's.

We now turn to the general case (Eqs. 24, 25), where materials A and B may be different. It is possible to derive a recurrence relation similar to Eq. (3B.4), in terms of two 4x4 matrices; one each for the odd and even numbered layers. In particular, we find

Reproduced with permission of the copyright owner. Further reproduction prohibited without permission.

$$X_{k+4} = X_{k+3}\left[F_B + \beta(1-\beta)\Xi_B + \frac{\Psi_B}{\Psi_A}\beta\right]$$
$$+X_{k+2}\left[1-\beta(1-\beta)\left(\Xi_B + \Psi_B H_A^* - \frac{\Psi_B}{\Psi_A}\Xi_A\right) - \frac{\Psi_B}{\Psi_A}\beta F_A\right] \qquad (3B.8a)$$
$$-X_{k+1}\left[F_B + \frac{\Psi_B}{\Psi_A}\beta + \beta(1-\beta)\left(\frac{\Psi_B}{\Psi_A}\Xi_A - \Psi_B H_A^*\right)\right] + X_k\left[\frac{\Psi_B}{\Psi_A}\beta F_A\right]$$

for even k and

$$X_{k+4} = X_{k+3}\left[F_A - (1-\beta)\Xi_A + \frac{\Psi_A}{\Psi_B\beta}\right]$$
$$+X_{k+2}\left[(1-\beta)\left(\Xi_A + \Psi_A H_B^* - \frac{\Psi_A}{\Psi_B}\Xi_B\right) + 1 - F_B\frac{\Psi_A}{\Psi_B\beta}\right] \qquad (3B.8b)$$
$$-X_{k+1}\left[(1-\beta)\left(\Psi_A H_B^* - \frac{\Psi_A}{\Psi_B}\Xi_B\right) + F_A + \frac{\Psi_A}{\Psi_B\beta}\right] + X_k\left[F_B\frac{\Psi_A}{\Psi_B\beta}\right]$$

for odd k. We use Eq. (22) to obtain similar relations for Δ_k or Δ_k^*.We define the two 4 by 4 matrices $\mathbf{L}_A$ and $\mathbf{L}_B$:

$$\mathbf{L}_A = \begin{pmatrix} L_A^{11} & 1 & 0 & 0 \\ L_A^{21} & 0 & 1 & 0 \\ L_A^{31} & 0 & 0 & 1 \\ L_A^{41} & 0 & 0 & 0 \end{pmatrix} \quad \mathbf{L}_B = \begin{pmatrix} L_B^{11} & 1 & 0 & 0 \\ L_B^{21} & 0 & 1 & 0 \\ L_B^{31} & 0 & 0 & 1 \\ L_B^{41} & 0 & 0 & 0 \end{pmatrix} \qquad (3B.9)$$

The matrix coefficients $\mathbf{L}_A^{i1}$ and are simply the product of the ith bracketed term in Eq. (3B.8a) and $e^{-\xi^*\eta_i}$, where η_i is H_A^*, $H_A^* + H_B^*$, $2H_A^* + H_B^*$ and $2\left(H_A^* + H_B^*\right)$ for $i = 1$, 2, 3, and 4, respectively. Similarly, the matrix coefficients $\mathbf{L}_B^{i1}$ and are simply the product of the ith bracketed term in Eq. (3B.8b) and $e^{-\xi^*\eta_i}$, where η_i is H_B^*, $H_A^* + H_B^*$, $H_A^* + 2H_B^*$ and $2\left(H_A^* + H_B^*\right)$ for $i = 1$, 2, 3, and 4, respectively.

In the general case, the vector $\mathbf{Y}_k$ has four components $\mathbf{Y}_k = \left\langle \Delta_{k+3}^+,\ \Delta_{k+2}^+,\ \Delta_{k+1}^+,\ \Delta_k^+ \right\rangle$. The amplitude of the vector $\mathbf{Y}_k$ is simply

Reproduced with permission of the copyright owner. Further reproduction prohibited without permission.

$$\mathbf{Y}_k = \mathbf{Y}_1(\mathbf{L}_B\mathbf{L}_A)^{(k-1)/2} = \langle \Delta_4^+, \quad \Delta_3^+, \quad \Delta_2^+, \quad 1\rangle(\mathbf{L}_B\mathbf{L}_A)^{(k-1)/2} \tag{3B.10}$$

for odd values of k and $\mathbf{L}_A$ times this for even values of k. Defining the matrix $\mathbf{L}$ as a product of matrices $\mathbf{L}_B$ and $\mathbf{L}_A$ and the matrix $\mathbf{\Lambda}$ as the matrix of the eigenvectors of matrix $\mathbf{L}$ corresponding to the eigenvalues λ_1, λ_2, λ_3 and λ_4 we obtain a closed form expression for Δ_k^+. Assuming that k is even and is greater than four, we have:

$$\Delta_k^+ = \sum_{i=1}^{4} \alpha_i \Lambda_{i1} \lambda_i^{(k-4)/2} \quad \text{and} \quad \Delta_{k-1}^+ = \sum_{i=1}^{4} \alpha_i \Lambda_{i2} \lambda_i^{(k-4)/2} \quad , \tag{3B.11}$$

where $\mathbf{\Lambda}_1$ and $\mathbf{\Lambda}_2$ are the components of the first and second column of the matrix of the eigenvectors of $\mathbf{\Lambda}$, respectively, and α is the expansion coefficient of the vector in the basis of eigenvectors: $\langle \alpha_1, \quad \alpha_2, \quad \alpha_3, \quad \alpha_4 \rangle = \mathbf{Y}_1 \mathbf{\Lambda}^{-1}$.

As in the case of nearly equivalent materials A and B, when the materials in these layers are different we only need to consider the asymptotic part of Eqs. (3B.11), i.e.

$$\Delta_k^+ = \alpha_1 \Lambda_{11} \lambda_1^{(k-4)/2} \quad \text{and} \quad \Delta_{k-1}^+ = \alpha_1 \Lambda_{12} \lambda_1^{(k-4)/2} \tag{3B.12}$$

where λ_1 is the maximal eigenvalue. All of the stability arguments used in the nearly equivalent layers case can be applied to the general case. To be more specific, the eigenvalue λ in the general case corresponds to the square of the same eigenvalue in the nearly equivalent layers case and the instability condition $\lambda_1 > 1$ applies in the general case as well. The phase of the perturbation cannot be easily analyzed because the phase between two successive layers is now determined by two numbers: $\Lambda_{11}/\Lambda_{12}$ if we proceed from an odd-numbered layer to an even-numbered one and $\lambda_1\Lambda_{12}/\Lambda_{11}$ if we proceed from an evennumbered layer to an oddnumbered one. In the nearly equivalent layers case, these two values are equal to each other.

Although the dependence of the mode of the perturbation of the growth conditions and material parameters cannot be easily presented for the general case, the question of

Reproduced with permission of the copyright owner. Further reproduction prohibited without permission.

whether the perturbation is stable or unstable can be easily answered from the analysis of the maximal eigenvalue λ_1.

Reproduced with permission of the copyright owner. Further reproduction prohibited without permission.

APPENDIX 4A

ANISOTROPIC SURFACE ELASTIC GREEN TENSOR

The elastic Green tensors associated with an isotropic elastic half space are easily derived and are well known [23]. While the Green tensors for an anisotropic half space may also be determined, they cannot be evaluated analytically except in special cases, e.g., a hexagonal crystal [25]. Fortunately, this complexity may be significantly reduced in two-dimensional problems by application of the Stroh formalism [26].

Let us consider an anisotropic, elastic half-space occupying the region $y = 0$, with the x-axis parallel to the surface. This problem is two-dimensional, and all solutions are independent of the coordinate z. Following the approach proposed by Ting [47], we introduce the following three by three matrices:

$$\mathbf{Q}_{ik}(\theta) = C_{ijks} n_j n_s \,, \quad \mathbf{R}_{ik}(\theta) = C_{ijks} n_j m_s \,, \quad \mathbf{T}_{ik}(\theta) = C_{ijks} m_j m_s \,. \tag{4A.1}$$

where $n_i = [\cos\theta, \sin\theta, 0]$, $m_i = [-\sin\theta, \cos\theta, 0]$, and C_{ijks} is the anisotropic elastic constant tensor. The angle θ is measured with respect to the OX axis in a counterclockwise direction (i.e., towards the OY axis). It is useful to identify the following three matrices:

$$\begin{aligned} &\mathbf{N}_1(\theta) = -\mathbf{T}^{-1}(\theta)\mathbf{R}^{T}(\theta) \,, \quad \mathbf{N}_2(\theta) = \mathbf{T}^{-1}(\theta) \\ &\mathbf{N}_3(\theta) = \mathbf{R}(\theta)\mathbf{T}^{-1}(\theta)\mathbf{R}^{T}(\theta) - \mathbf{Q}(\theta) \,. \end{aligned} \tag{4A.2}$$

and three incomplete integrals:

$$\mathbf{S}(\theta) = \frac{1}{\pi}\int_0^{\theta} \mathbf{N}_1(\omega)\,d\omega \,, \quad \mathbf{H}(\theta) = \frac{1}{\pi}\int_0^{\theta} \mathbf{N}_2(\omega)\,d\omega \,, \quad \mathbf{L}(\theta) = -\frac{1}{\pi}\int_0^{\theta} \mathbf{N}_3(\omega)\,d\omega \,. \tag{4A.3}$$

Reproduced with permission of the copyright owner. Further reproduction prohibited without permission.

The surface Green tensor $\mathbf{G}_{ij}(r,\theta)$ for an anisotropic, elastic half-space may now be written in terms of these quantities as (see expression (5.2) in the same article [47]):

$$\mathbf{G} = -\left[\frac{1}{\pi}(\ln r)\mathbf{I} + \mathbf{S}(\theta) - \frac{1}{2}\mathbf{S}\right]\mathbf{L}^{-1} \tag{4A.4}$$

where $\mathbf{I}$ is an identity matrix, and

$$\mathbf{S} = \mathbf{S}(\pi)\,, \quad \mathbf{H} = \mathbf{H}(\pi)\,, \quad \mathbf{L} = \mathbf{L}(\pi)\,. \tag{4A.5}$$

Integrals (4A.3) and (4A.5) can be computed analytically only in a few special cases. However, in order to describe the displacement field associated with a surface force line dipole, we need only evaluate the derivative of the surface Green's function with respect to x, rather than the entire surface Green tensor itself. This simplification allows us to avoid evaluating the indefinite integrals Eq. (4A.3) altogether, and only the elements of the matrix $\mathbf{L}$, which are the definite integrals Eq. (4A.5), need to be computed. At most, the matrix $\mathbf{L}$ contains six unique elements because it is symmetric. The resultant expression for the surface dipole Green tensor $\mathbf{g}$ is:

$$\mathbf{g} = -\frac{\partial}{\partial x}\mathbf{G} = \frac{1}{r}[\mathbf{I}\cos\theta - \mathbf{N}_1\sin\theta]\mathbf{L}^{-1}\,. \tag{4A.6}$$

In the case of cubic symmetry, when the half-space is bounded by a {001}-type plane and the <100> step lies along the OZ (as in the present case), this problem can be solved analytically. The matrix $\mathbf{L}$ becomes diagonal:

$$\mathbf{L}_{33} = C_{44}; \qquad \mathbf{L}_{11} = \mathbf{L}_{22} = L = \frac{C_{44}(C_{11} - C_{12})}{\sqrt{\left(4\dfrac{C_{11}C_{44}}{C_{11} + C_{12}} + H\right)\left(\dfrac{C_{11}C_{44}}{C_{11} + C_{12}}\right)}} \tag{4A.7}$$

Reproduced with permission of the copyright owner. Further reproduction prohibited without permission.

where H is the crystal anisotropy, $H = C_{11} - C_{12} - 2C_{44}$. In the isotropic limit ($H \rightarrow 0$), Eq. (4A.6) reduces to the well known isotropic elastic surface dipole Green tensor [23].

If we examine {111} surfaces rather than the {001} surfaces, as in recent experiments [18], computation of the elements of **L** requires either solving a cubic equation or numerical evaluation. Except for this one step, the procedure for deriving the surface Green tensor for a {111} surface is essentially the same as that outlined above for the (010)-<001> surface step geometry.

Reproduced with permission of the copyright owner. Further reproduction prohibited without permission.